PHILOSOPHICAL TRANSACTIONS OF THE ROYAL SOCIETY A MATHEMATICAL, PHYSICAL & ENGINEERING SCIENCES

On the Clouds of Bubbles Formed by Breaking Wind-Waves in Deep Water, and their Role in Air -- Sea Gas Transfer

S. A. Thorpe

Phil. Trans. R. Soc. Lond. A 1982 **304**, 155-210
doi: 10.1098/rsta.1982.0011

Phil. Trans. R. Soc. Lond. A **304**, 155–210 (1982) [155]
Printed in Great Britain

ON THE CLOUDS OF BUBBLES FORMED BY BREAKING WIND-WAVES IN DEEP WATER, AND THEIR ROLE IN AIR–SEA GAS TRANSFER

By S. A. THORPE

Institute of Oceanographic Sciences, Wormley, Godalming, Surrey GU8 5UB, U.K.

(*Communicated by Sir George Deacon, F.R.S. – Received 29 May* 1981)

CONTENTS

Clouds of small bubbles generated by wind waves breaking and producing whitecaps in deep water have been observed below the surface by using an inverted echo sounder. The bubbles are diffused down to several metres below the surface by turbulence against their natural tendency to rise. Measurements have been made at two sites, one in

 [Published 18 February 1982

fresh water at Loch Ness and the other in the sea near Oban, northwest Scotland. Sonagraph records show bubble clouds of two distinct types, 'columnar clouds' which appear in unstable or convective conditions when the air temperature is less than the surface water temperature, and 'billow clouds' which appear in stable conditions when the air temperature exceeds that of the water. Clouds penetrate deeper as the wind speed increases, and deeper in convective conditions than in stable conditions at the same wind speed. The response to a change in wind speed occurs in a period of only a few minutes.

Measurements of the acoustic scattering cross section per unit volume, M_v, of the bubbles have been made at several depths. The distributions of M_v at constant depth are close to logarithmic normal. The time-averaged value of M_v, $\bar{M}_v$, decreases exponentially with depth over scales of 40–85 cm (winds up to 12 m s^{-1}), the scale increasing as the wind increases. Values of $\bar{M}_v$ at the same depth and at the same wind speed are greater in the sea than in the fresh-water loch, even at smaller fetches.

Estimates have been made of the least mean vertical speed at which bubbles must be advected for them to reach the observed depths. Several centimetres per second are needed, the speeds increasing with wind. Results depend on the conditions at the surfaces of the bubbles, that is whether they are covered by a surface active-film. The presence of oxygen (or gases other than nitrogen) in the gas composing the bubbles appears not to be important in determining their general behaviour. The presence of turbulence in the water also appears unlikely to affect the gas diffusion rates from individual bubbles at wind speeds up to 16 m s^{-1}, except perhaps very close to the surface. The vertical variation of $\bar{M}_v$ and the trend with increasing wind speed is moderately well predicted by a 'cell model' taken to represent turbulent motions in the water. Analytical and numerical models in which the tendency of bubbles to rise is balanced by turbulent diffusion, and the effects of solubility of the gas within the bubbles are accounted for, are in reasonable agreement with the observations. An eddy diffusion coefficient is taken (in neutral conditions) to be equal to that in the atmospheric boundary layer over a rigid surface, linearly proportional to depth and friction velocity. The effects of stable or unstable conditions, and those of varying the saturation level in the water, are briefly examined.

Estimates are also made, by using the observed values of $\bar{M}_v$ supported by the analytical results, of the gas flux from the bubbles. Most of the flux occurs in the upper 2 m of the water column. This flux is compared with existing measurement of the net gas flux across the air–water interface. It is concluded that in Loch Ness the component of the flux via the bubbles is small at wind speeds up to 12 m s^{-1}, but that at sea the contribution is significant at wind speeds of 12 m s^{-1} (at least when the water is close to being saturated) and that at higher wind speeds the bubble contribution may dominate in the processes of air–water gas transfer.

1. Introduction

When, in windy conditions, surface gravity waves in deep water break as 'whitehorses' or 'whitecaps', many small bubbles are produced and carried below the water surface. These bubbles have been observed by using a fixed, upward-pointing, sonar located some 30 m below the water surface, both in fresh water in Loch Ness and in the sea near Oban in Scotland. Bubbles are not distinguished individually by the sonar but *en masse*, as clouds are seen in the atmosphere. The shape of the bubble clouds and the depth to which they extend are results of the turbulent motions in the water. Being *below* the surface these bubbles may be distinguished from the floating bubbles or *foam*, and their dynamics and persistence are influenced by different processes.

Knowledge of wave-generated bubbles in the sea is meagre and measurements few (Wu 1981). In 1963 Kanwisher reported that under the violent conditions of a winter storm in the North Atlantic 'an echo sounder head floating at a depth of 30 m and looking up showed foam being

swept down to 20m' below the sea surface. This was a remarkable observation, not only because it suggested the use of acoustics to study the dynamics of the motion just below the surface of the sea, but because Blanchard & Woodcock (1957) had shown that the lifetime of bubbles thought to be typical of those produced by breaking waves in the sea was only a few minutes, and thus the downward speed of the bubbles must have been many centimetres per second. Kanwisher also remarked that we 'may surmise that the total volume of bubbles produced' at the sea surface 'increases as some power of the wind velocity greater than two', and that we 'can only conclude that bubbles from breaking waves may be significant gas exchanging devices at the higher wind velocities'. The contribution of bubbles to gas transfer across the sea surface is still unknown, or ignored (see for example the reviews by Brtko & Kabel (1978) and Jones (1980)), and the literature contains many caveats regarding their importance. We shall produce evidence that the contribution is significant and show that bubbles provide a physical asymmetry in the transfer processes to and from the sea surface and may require appropriate parametrization in the global budget of gases.

Some direct optical observations of bubbles in the sea have been made. Blanchard & Woodcock (1957) made estimates in the near-shore zone and correctly, as later observations have shown, concluded that most bubbles are less than 200 μm in diameter. Medwin (1970) also made optical observations, but only in the near-shore zone in low wind speeds and in conditions in which biological contributions to the apparent bubble population appear to have been significant.

Kolovayev (1976) appears to have been the first to catch, photograph, and count bubbles below breaking waves in the open sea at appreciable wind speeds, up to 13 $m s^{-1}$. The most numerous bubbles in the depth range 1.5–8 m are those with radii of about 70 μm and very few bubbles exceeded 300 μm in radius. The number of bubbles decreased with depth and increased with wind speed.

Johnson & Cooke (1979) succeeded in photographing bubbles *in situ* in the sea, using a camera suspended from a surface float and thus overcoming the need in Kolovayev's technique to allow the bubbles to rise on to a transparent plate, perhaps dissolving on their way. Bubbles were sampled at depths between 0.5 and 4.0 m in winds of 8–13 $m s^{-1}$, and the smallest bubbles that could be detected had radii of 17 μm. The bubble distributions had a peak at radii of about 40–50 μm, smaller than found by Kolovayev. The numbers fell rapidly for radii less than this peak. They also decreased rapidly as depth increased, and the distributions became narrower, with the absence of the larger bubbles. The numbers increased with wind speed, with larger bubbles appearing at depths where they were previously absent. At 1.8 m depth in winds of 11–13 $m s^{-1}$, some 1.56×10^5 bubbles m^{-3} were observed. Their total volume would, however, have contributed a density change in the water equivalent to that produced by a temperature change of only 1.5×10^{-3} K and thus probably made an insignificant contribution to the dynamics.

Acoustic means of detecting bubbles were developed in World War II in connection with submarine detection of the bubble-containing wakes of surface craft, but there are few instances of the deliberate use of acoustics to observe naturally occurring bubbles. Medwin (1970, 1977) used an attenuation method at various frequencies to deduce the size distribution of bubbles at depths of 3–36 m, but only at low wind speeds (less than 6.2 $m s^{-1}$). The number of bubbles found at 4 m increased by a factor of about 2 for an increase in wind speed from 3.3 to 5.5–6.1 $m s^{-1}$. The measurements were made from an oceanographic tower, a moored vessel or a floating buoy, and the presence of these structures may have contributed to the observed bubble populations.

PHILOSOPHICAL TRANSACTIONS OF THE ROYAL SOCIETY A MATHEMATICAL, PHYSICAL & ENGINEERING SCIENCES

Aleksandrov & Vaindruk (1974) appear to have been the first to describe short-term variations of the near-surface 'aerated' layer. They used a bottom-mounted upward-pointing sonar 1 km offshore in a water depth of 20 m, and recognized that because the orbital motion of surface waves cannot carry bubbles down to the depths at which they are observed, or sustain them at depth, the observed distributions must be a reflexion of the presence of turbulence. Aleksandrov & Vaindruk suggested that because the smallest bubbles rise very slowly through the water, acoustic observations of bubbles might be used to study near-surface turbulence. They measured both the height of the water surface above the sonar and the depth of the base of the bubble clouds. The latter responded naturally to the orbital motion of the surface waves and also to longer-period variations due, it was suggested, to the turbulent motions of the mixing layer. The variation in the depth of the bubble clouds increased with wind speed.

The present work is a continuation of the observations reported by Thorpe & Stubbs (1979), Thorpe & Humphries (1980) and Thorpe & Hall (1980, 1982) in which a 248 kHz upward-pointing sonar was used to detect bubbles in Loch Ness. We have largely substantiated the suggestion by Aleksandrov & Vaindruk that a relation exists between the bubble clouds and the turbulence. Thorpe & Stubbs showed that the observed average penetration depth of the bubble clouds, d (m), estimated from sonagraph records, increases with wind speed measured at 10 m, W_{10} (m s^{-1}), approximately as

$$d = 0.4(W_{10} - 2.5) \tag{1}$$

and suggested that the shape of the clouds depends on the direction of the heat flux through the water surface, columnar clouds appearing when the air was colder than the water, billow-like clouds when the water was colder than the air. Thorpe & Humphries produced circumstantial evidence that some of the variation in cloud intensity could be associated with waves breaking in, or near, the area of the surface covered by the sonar beam. Thorpe & Hall described the thermal structure of the mixing layer and showed that descending bubble clouds can sometimes be associated with downward-moving water on surfaces tilted to the horizontal, but parallel to thermal fronts resulting from the straining of the mean temperature field by turbulent eddies with axes across the wind direction. The region of downward-moving water extended beyond the depth to which bubbles were seen to descend. Wind rows also produce a significant increase in the local concentration of the bubbles near the surface. There is hence a relation between the bubble clouds and certain identifiable turbulent structures within the near-surface mixing layer.

New observations are described in § 2. These provide estimates of the scattering cross section per unit volume of the bubble clouds. The acoustic scattering cross section of an air bubble in water is given by

$$\sigma(a, \omega) = \frac{4\pi a^2}{(1 - \omega_0^2/\omega^2)^2 + \delta^2}. \tag{2}$$

Devin (1959) gives values of the damping coefficient, δ; ω is the sonar frequency, and ω_0 is the bubble's resonant frequency,

$$\omega_0 = \frac{1}{2\pi a}\left(\frac{3\gamma' p}{\rho}\right)^{\frac{1}{2}} \tag{3}$$

(in cycles per unit time), where γ' is the ratio of specific heats, c_p/c_v, and p is the hydrostatic pressure. For bubbles of radius much less than the resonant radius, a_r, where

$$a_r = \frac{1}{2\pi\omega}\left(\frac{3\gamma' p}{\rho}\right)^{\frac{1}{2}}, \tag{4}$$

the scattering cross section $\sigma \approx 4\pi a^6/a_0^4$, which rapidly diminishes as a decreases. For bubbles with radius much larger than the resonant radius, $\sigma \approx 4\pi a^2$, the surface area of the bubbles.

Figure 1 shows the variation of σ with a for the 248 kHz sonar used in our experiments with p corresponding to 1 m depth. The resonant radius is 14 μm and the width of the resonant peak is about 7 μm.

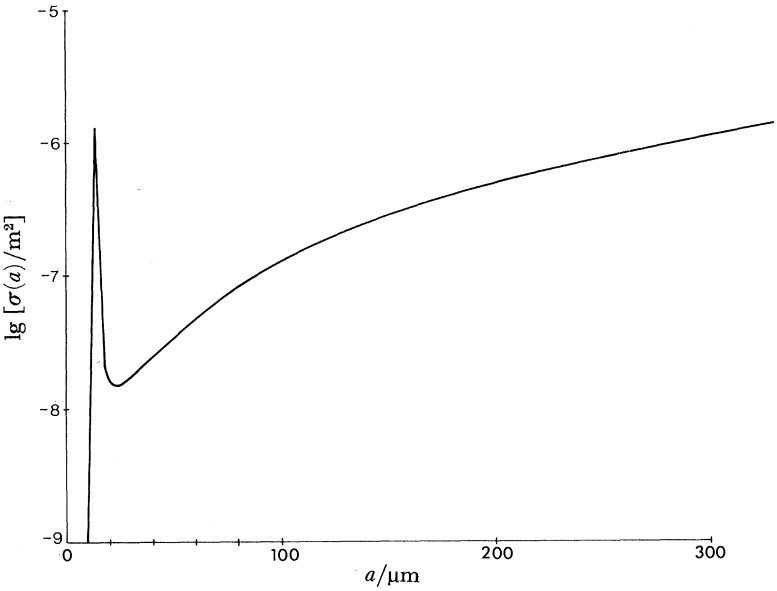

FIGURE 1. The variation of the scattering cross section of an air bubble, σ, at a depth of 1 m with bubble radius, a, for a sound source of 248 kHz.

TABLE 1. THE SCATTERING CROSS SECTION PER UNIT VOLUME, M_v, OF BUBBLES AT VARIOUS DEPTHS AND WIND SPEEDS BASED ON OBSERVATIONS BY JOHNSON & COOKE (1979)

wind speed / (m s^{-1})	depth/m	M_v/m^{-1}
8–10	1.5	9.09×10^{-4}
11–13	0.7	2.74×10^{-2}
11–13	1.8	7.14×10^{-3}
11–13	4.0	7.14×10^{-4}

The acoustic scattering cross section per unit volume of a cloud of bubbles with a density $N(a)$ bubbles per unit volume per unit radius, is given by

$$M_v = \int_0^\infty N\sigma \, da. \tag{5}$$

For a 248 kHz signal, M_v has been estimated from the four bubble size distributions reported by Johnson & Cooke (1979). For these distributions the greatest contribution to M_v comes from bubbles of size 50–60 μm. and the narrow resonant peak does not contribute a large part. The values of M_v are given in table 1. The data are scanty, but it may be noted that in winds of 11–13 m s^{-1}, M_v decays approximately exponentially with depth with an exponentiation scale of about 0.8 m, and there is a tenfold increase in M_v at 1.5 m interpolated for 11–13 m s^{-1} winds from the lower to the higher wind range.

In the observations described in §2 it was possible to measure M_v and to record its variation with depth and with time. The dynamics of small bubbles, and gas diffusion from bubbles, are reviewed in §3. The results are used to devise theoretical models for the behaviour and distribution of bubbles below the surface of the water (§4). The observations are compared with calculations of M_v derived from the models and are found to be reasonably consistent with one based on eddy diffusion coefficients for flows in a turbulent boundary layer near a rigid surface. An important aspect of the study of bubbles is the information that they may give about diffusion from, or near, the water surface, and in §5 we discuss how the observations may be used to estimate the net gas flux from the bubbles into the water.

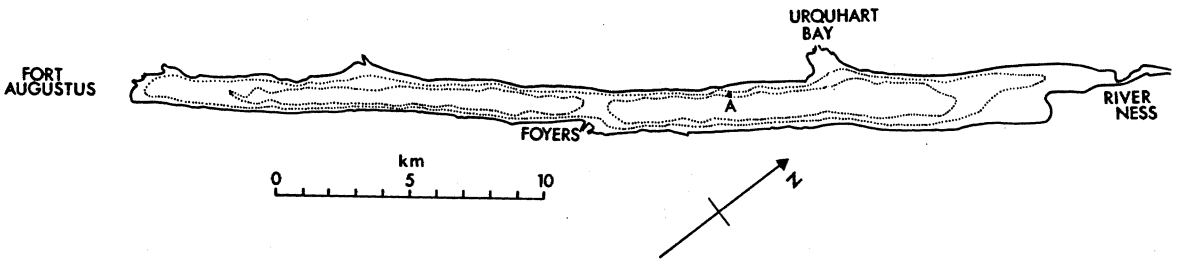

FIGURE 2. Loch Ness. Measurements were made at position A.
The dotted contours are at 90 and 180 m.

2. OBSERVATIONS

2.1. *The acoustic system*

Observations have been made by using the same acoustic system, although mounted differently, both in Loch Ness and in the sea near Oban. The sonar operates at 248 kHz with a pulse length of 0.08 ms and repetition rate of about 2.5 Hz. The beam is directed upwards towards the water surface.

The site at Loch Ness (57° 17.2′ N, 4° 27.7′ W; see figure 2) was some 250 m offshore where the water depth is 166 m. The loch is fresh water. The sonar transducer was supported by floats and connected to shore by a cable running through a sheave on the bottom of the loch. The transducer could be lowered or raised in the water column by hauling in, or paying out, the cable on shore. The operating depth for the measurements reported here was 30–35 m, sufficiently deep that the mooring was not disturbed by surface waves, and the bubble 'targets' were beyond the Fresnel zone, extending to about 21 m from the transducer. The width of the sonar beam was about 5° (determined by towing a target, a weighted trawl float, across the beam). The surface directly receiving and reflecting sound from the beam, the surface 'footprint' of the sonar, is about 2.6–3.1 m in diameter. The estimated beam angle was consistent with the distortion of surface waves as they appeared on the sonagraph. The sonar correctly senses the position of a wave trough but, because of the finite beam width, receives reflected sound from the flanks of the wave rather than the crest itself, when the crest is over the sonar. The wave profile is thus flattened to a degree dependent on the beam angle and the wavelength.

Data were collected on days on which the wind was predominantly southwesterly or northeasterly, blowing along the axis of the loch, when the maximum fetches were approximately 20 and 14 km respectively. Because of the narrowness of the loch and the resulting limitation in the angular spread of the spectrum, especially of long waves, the effective fetches must be less.

Wind speed was measured by an anemometer on a tripod in the loch, and air and surface water temperature were taken regularly.

At the site near Oban (56° 27.6′ N, 5° 27.1′ W; figure 3) the transducer was mounted on a quadpod resting on the sea bed, and was levelled by divers. The mean transducer depth was 34 m (similar to that in Loch Ness) and the mean tidal range about 3.5 m. A cable ran from the equipment to the recording instruments, including an anemometer, on shore. The average fetches are given in table 2. Average temperature and salinity profiles obtained near the echo sounder in calm weather near low tide on 30 January 1981 (figure 4) show a layer of water of lower salinity near the surface. This derives from the fresh water in the large catchment area around Loch Etive which discharges into the sea through the Falls of Lora to the east of the sonar.

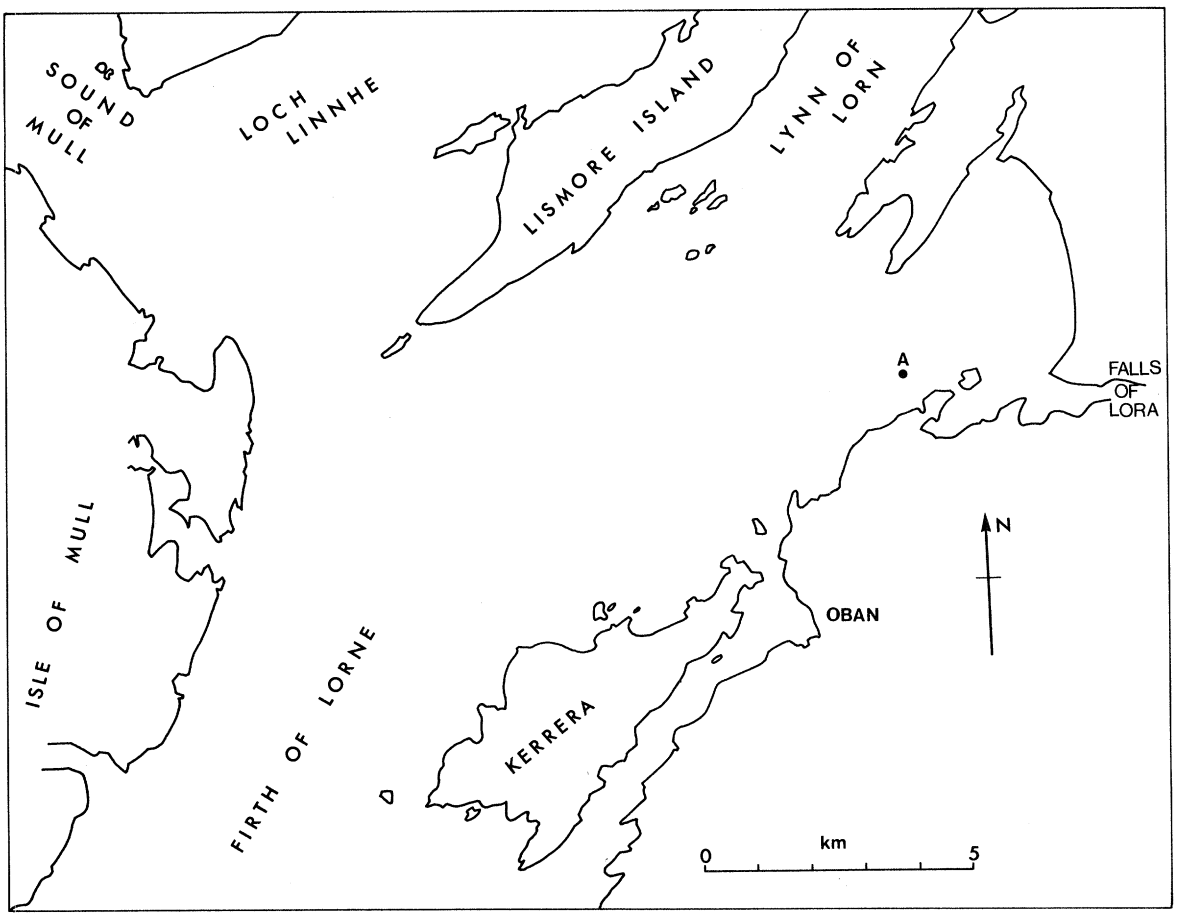

FIGURE 3. The site near Oban. Measurements were made at position A.

At both sites data were recorded on a sonagraph and in digital form on magnetic tape. Each digital record corresponded to the average amplitude of sound returned from reflectors within a selected depth range, or 'bin', over a period of 10 s. Seven such bins, each approximately 45 cm high, were sampled every 10 s. One bin was placed deep, normally well below the bubble clouds, and served to establish the noise level of the system or to detect extraneous noise due to passing vessels. The six remaining bins were arranged at intervals, with the uppermost close to, but below, the wave troughs. The effect of finite bin-height, and that of the surface waves in moving

water and bubbles through the bins, are considered in Appendix 1, and are shown to be generally small, in the sense that they do not significantly change the observed vertical average distribution of scattering cross section from that which would be observed if the bins were at constant depths below the surface. The positions of the bins relative to the surface were set manually at Loch Ness. Such a process was not practicable at Oban, however, because of the tides. The sonar was itself used to locate the average position of the surface over successive periods of about 10 min and the bins were then positioned automatically. The maximum adjustment in the bins' levels at peak tidal flow amounted to about 10 cm after each averaging period.

TABLE 2. MEAN WIND FETCH AT THE OBAN SITE

(Over a 4° sector the southwest fetch is virtually unrestricted in a direction down the Firth of Lorne, except for the island of Colonsay at 55 km, until the coast of Donegal at 165 km. The sector of short fetch in this direction is very narrow.)

wind direction	maximum fetch km	minimum fetch km	mean fetch km
SE	1.1	0.8	0.9
S	1.4	0.9	1.1
E	3.3	1.2	2.2
N	4.3	1.7	2.6
NE	4.4	3.3	3.9
NW	5.7	4.0	4.7
W	13.6	6.1	9.8
SW	165	1.4	

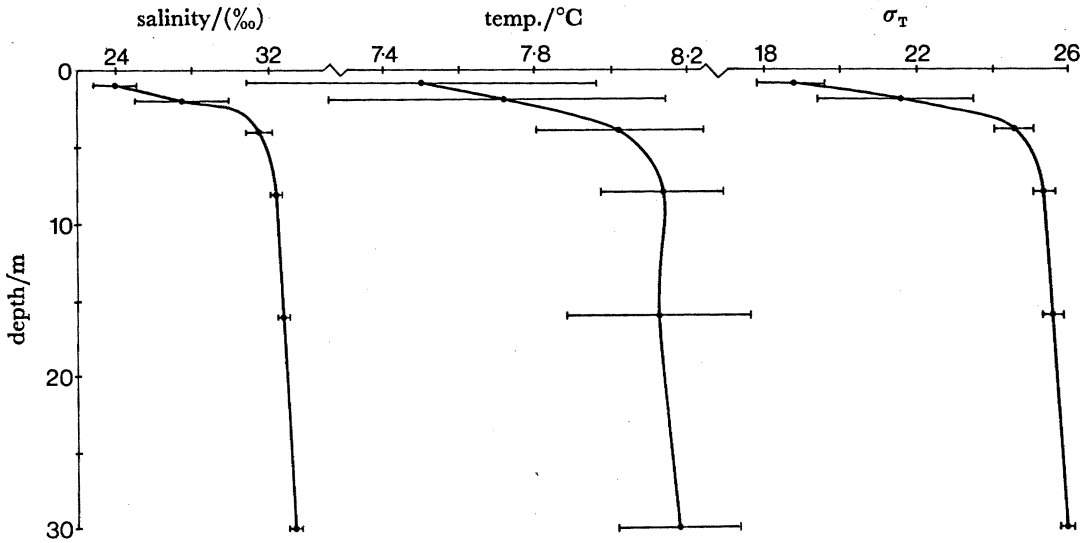

FIGURE 4. Mean and standard deviations of six profiles of salinity, temperature, and σ_T near position A (figure 3) on 30 January 1981. The data were obtained in calm weather during a four-hour period near low water.

Calibration was achieved in Loch Ness by recording the output of the system when a carefully machined spherical brass sphere of diameter 12.33 cm, supported by a submerged float, was located within one of the bins. Some details are described in Appendix 2. In practice the variation of target position within the sonar beam and other poorly known factors, such as the exact shape of the beam, make even this *in situ* calibration imprecise, and the estimates of M_v may be in error by a factor of two. The measurements are, nevertheless, of value in comparative experiments

(in fresh and salt water and at different wind speeds) and, as will be shown (§2.3) they are consistent with those of Johnson & Cooke.

In evaluating the sonagraph 'pictures' of bubble clouds, it is important to recognize two factors:

(i) The beam width is finite and details of a cloud narrower than about 2.6 m will not be resolved. Quantitative observations of the breaking of waves at sea are few. Small-scale breaking occurs in an irregular and disordered way, mostly near the crests of the largest waves. Casual observation in moderate and strong winds (more than 7 m s^{-1}) suggests that the most vigorous wave breaking is within groups of waves in which the highest continue to 'spill' and produce 'white water', and hence bubbles, for about one wave period (see also Thorpe & Humphries 1980). The horizontal scale of bubble clouds so produced is thus comparable with the length of the surface waves. This is over 6 m for the waves of 2 s, or more, typically seen in Loch Ness and at Oban in such winds, and the dominant clouds will usually exceed the width of the sonar beam, at least near their source at the water surface.

(ii) The sonar is in a fixed position and records the variation with time. It cannot resolve a difference between the growth of a cloud in a position fixed above the sonar and an apparent increase in cloud depth due to advection through the beam. The rate of descent of a cloud cannot be determined by the sonar alone.

In selecting those parts of the data set for presentation we have excluded periods in which the wind direction was changing rapidly, those in which the observed standard deviation of the wind speed varied by more than one fifth of the mean wind speed, or those in which biological scatterers were present in the bins (this never occurred in Loch Ness, but caused the rejection of about one third of the data at Oban). Such scatterers appeared as individual targets or as patches of individual targets, often showing a tendency to migrate upwards through the water column from near the sea bed at dusk, and were easily recognized on the sonagraph records.

2.2. *Loch Ness: bubbles in fresh water*

Figures 5*a–e* show examples of measurements made in Loch Ness. The upper panel of each figure shows the sonagraph display, with the mean level of the surface marked by arrows. The time increases to the *left* and is shown at the bottom. The second panel shows the contours of lg M_v, where M_v is the scattering cross section per unit volume (m^{-1}). The fairly uniform mean spacing suggests that M_v decreases almost exponentially with depth. The actual values of M_v are given in the third panel. These curves apply to the scattering from six 'bins' at equal depth intervals between the horizontal lines in the sonagraph display, the area of which is contoured.

The sonagraph displays show that the bubble clouds penetrate to greater depths, and last longer, as the wind speed increases. Two different cloud types can be recognized at similar wind speeds. Figures 5*a*, *b* and *d* show clouds with a vertical structure (columnar clouds) which appear predominantly during periods when the air temperature is less than the water temperature. The clouds presumably reflect the presence of vertical convection and low shear. Figures 5*c* and *e*, in contrast, show tilted roll-like structures (billow clouds) similar to the pattern seen in Kelvin–Helmholtz instability. These occur when the air temperature exceeds that of the water, and the heat flux tends to stabilize the water column. The patterns are a response to eddies developing in the stably stratified shear flow and are similar to those that appear on the crests of cumulus clouds as they penetrate into stable air in their final stages of growth. Unlike the cumulus clouds, however, the bubbles were not observed to penetrate to the boundary of the mixing layer (see

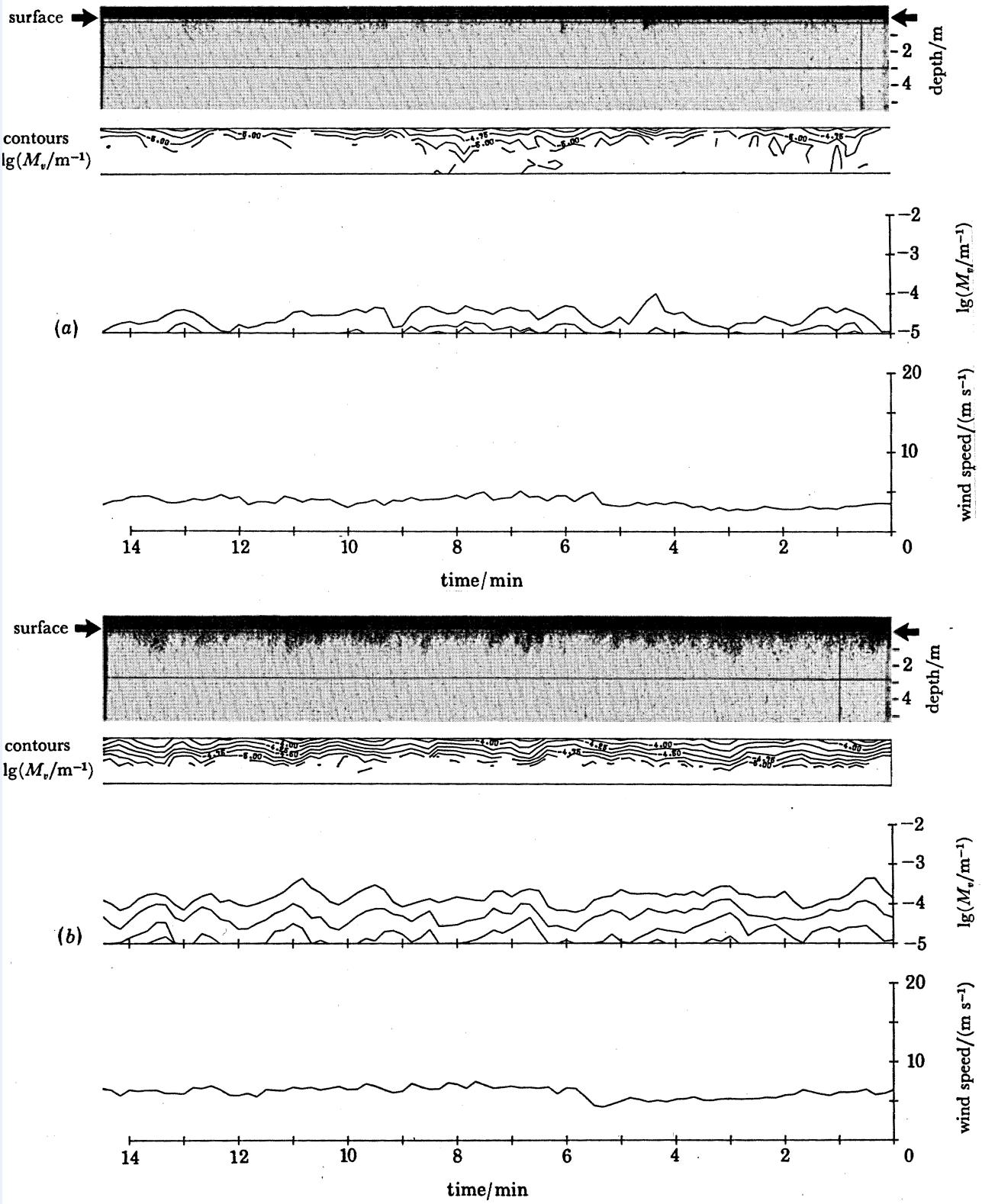

FIGURE 5 (*a*) and (*b*). For description see page 166.

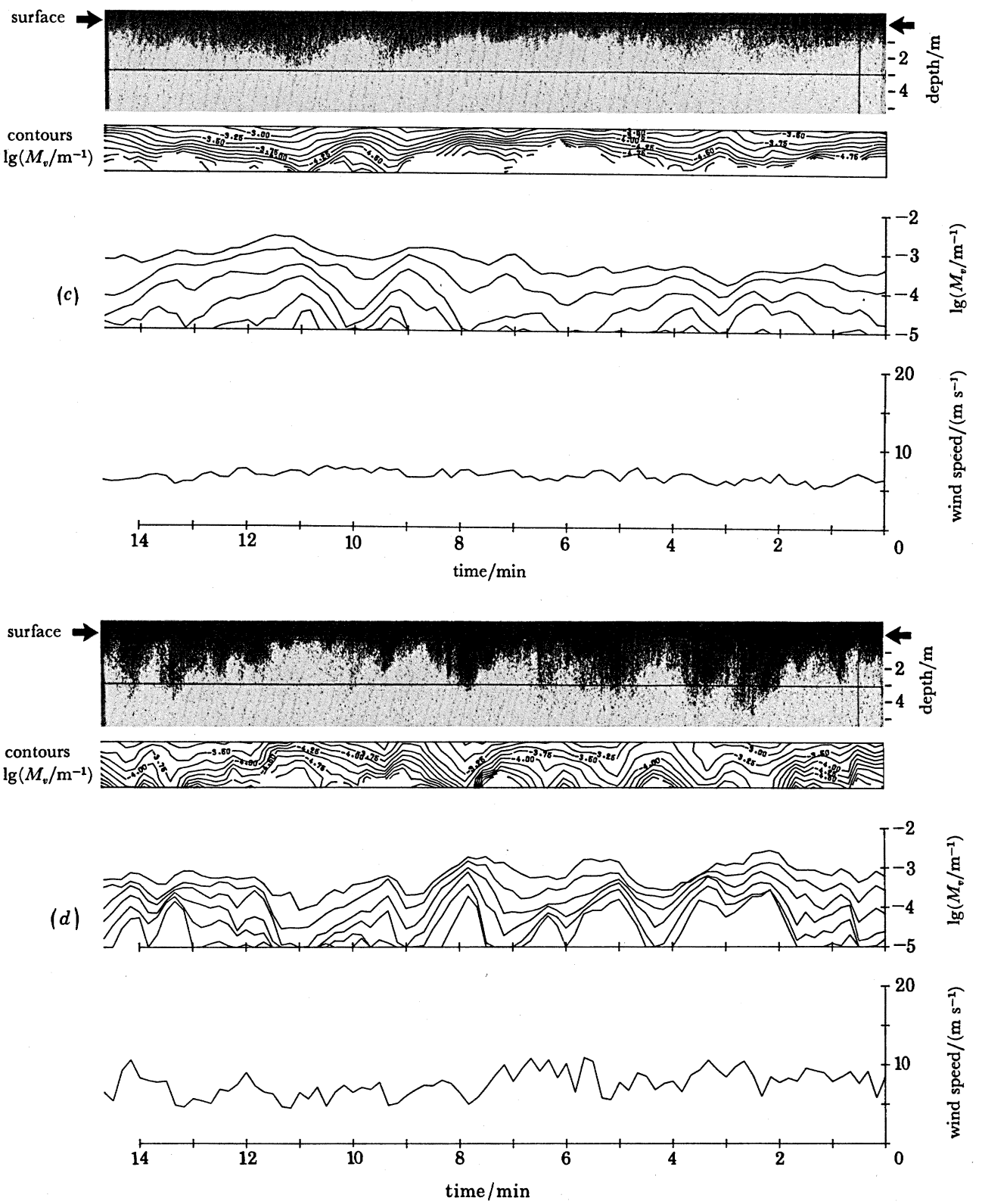

FIGURE 5 (*c*) and (*d*). For description see page 166.

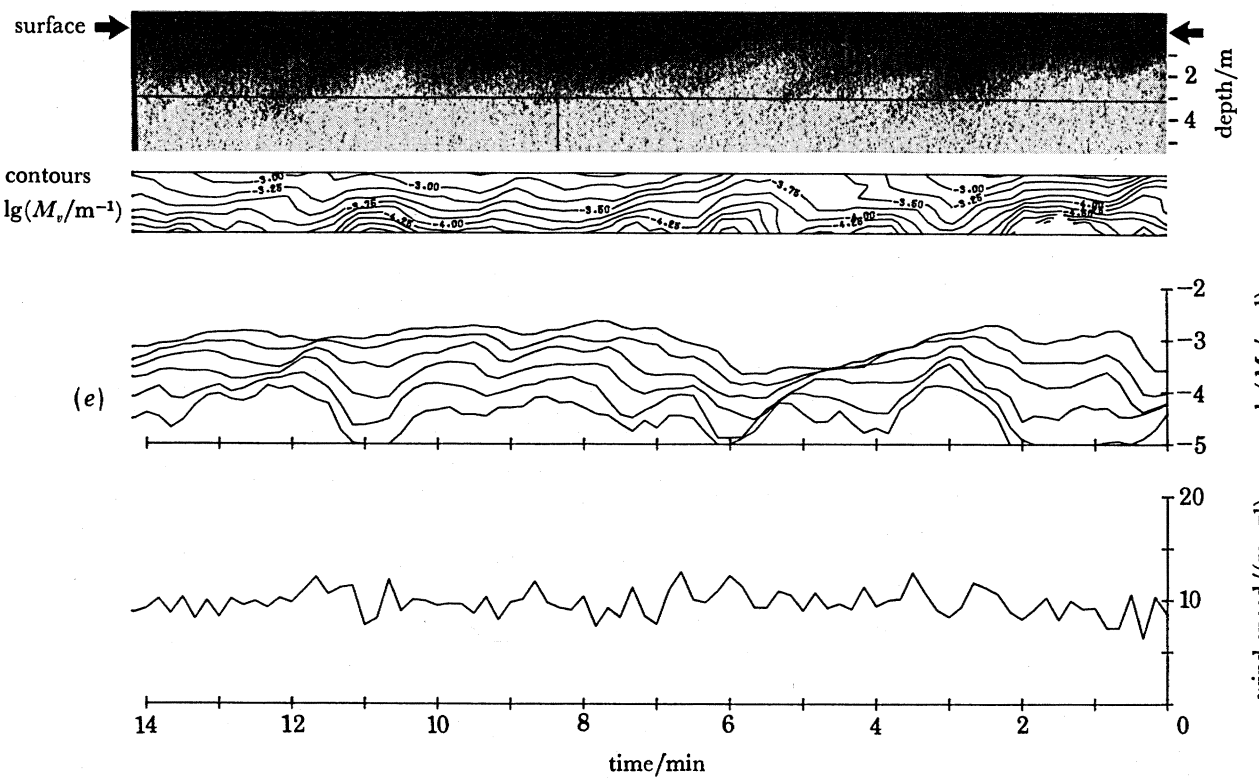

FIGURE 5. Sonagraph records, contours of lg M_v (contour interval 0.25) values of lg M_v, and wind speeds from Loch Ness. Values of air–water temperature differences are (*a*) −0.25 K, (*b*) −0.25 K, (*c*) 1.6 K, (*d*) −3.5 K, (*e*) 4.6 K. There is a difference in the appearance of cloud types in stable and unstable conditions.

Thorpe & Hall 1980; for temperature–depth profiles see Thorpe 1977). Clouds penetrated typically to only one half the mixing layer depth.

Figures 6*a* and *b* show the response to a squall and to an increase in wind speed. There is in each a delay of only about 2 min before the appearance or deepening of the clouds, reflecting the rapid response of the wave field and the increase in whitecaps. The bubbles persist for a much longer period after the passing of the squall.

Figure 7*a* is an example of bubble response to a temperature front. A strong line of foam parallel to shore and moving offshore at 4.43 cm s^{-1} towards the southeast crossed over the position of the echo sounder 6.5 min after the start of the record. This is marked by bubbles that descend (6.5–10 min after the start) much deeper than those before or afterwards. A temperature traverse across the loch (figure 7*b*) crossed the foam line 23 min after the beginning of the record in figure 7*a* and showed that the foam line was indeed associated with convergence of stratified water nearshore and relatively well mixed water offshore. Details of the techniques used for these measurements are given by Thorpe & Hall (1982).

Average values of M_v, $\overline{M}_v$, selected according to wind speed are plotted against depth in figure 8. Values of $\overline{M}_v$ decrease rapidly with depth, decaying approximately exponentially over a distance of about 47 cm at winds of 3–7 m s^{-1} or 61 cm at winds of 9–12 m s^{-1} (see figure 28). Distributions of M_v have large positive skewness and excess, both generally increasing with depth; those of lg M_v are close to Gaussian. There is a general increase in $\overline{M}_v$ at constant depth with wind speed (figure 9).

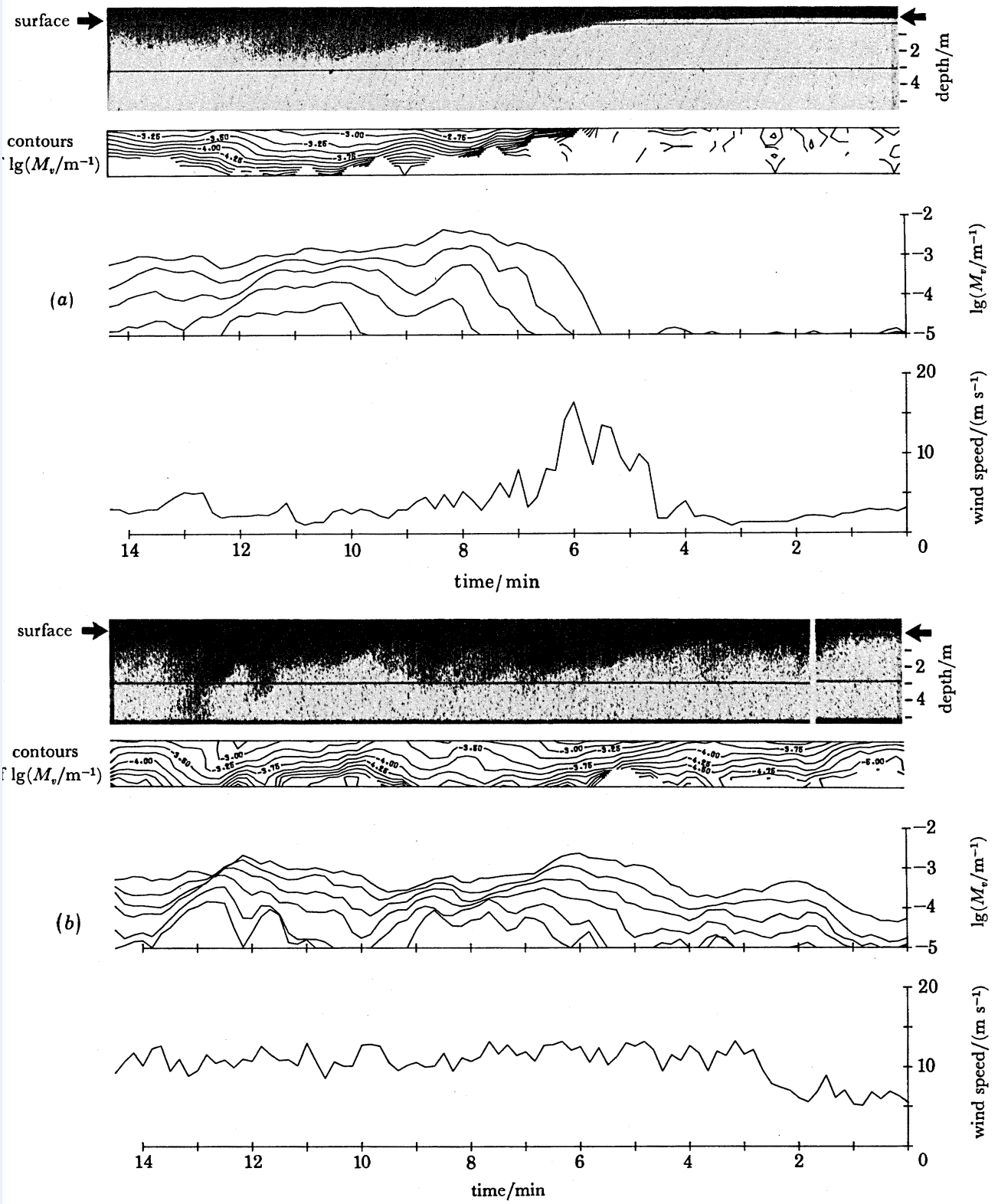

FIGURE 6. Sonagraph, M_v, and wind-speed records from Loch Ness for (*a*) a brief squall and (*b*) an increase in wind speed. The gap early in the sonagraph record is due to a recorder malfunction.

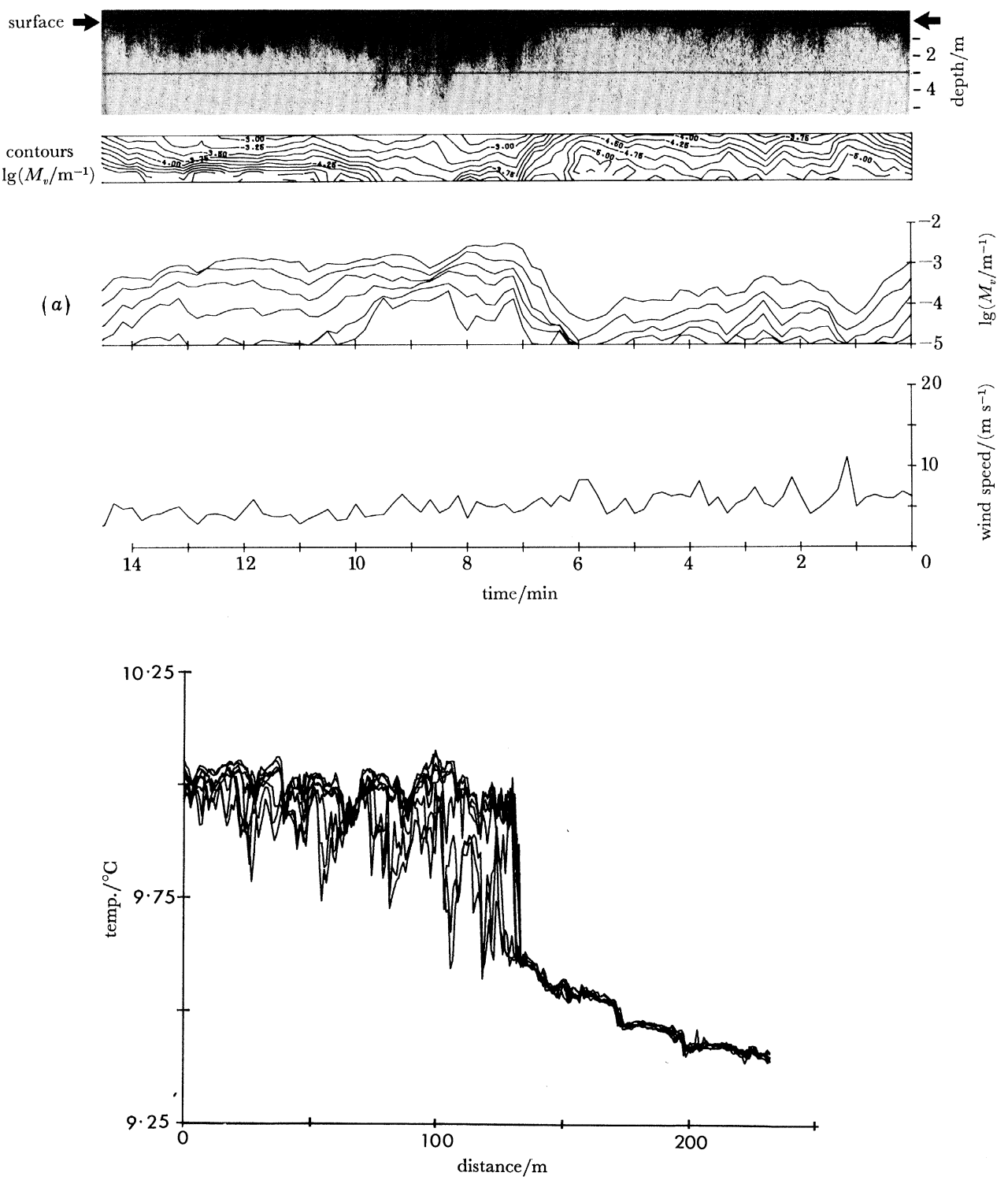

FIGURE 7. (*a*) Sonagraph, M_v, and wind records from Loch Ness during the passing of the temperature front shown in (*b*). (*b*) Eight records from thermistors at between 0.4 and 3.1 m depth in a section northwest–southeast across Loch Ness.

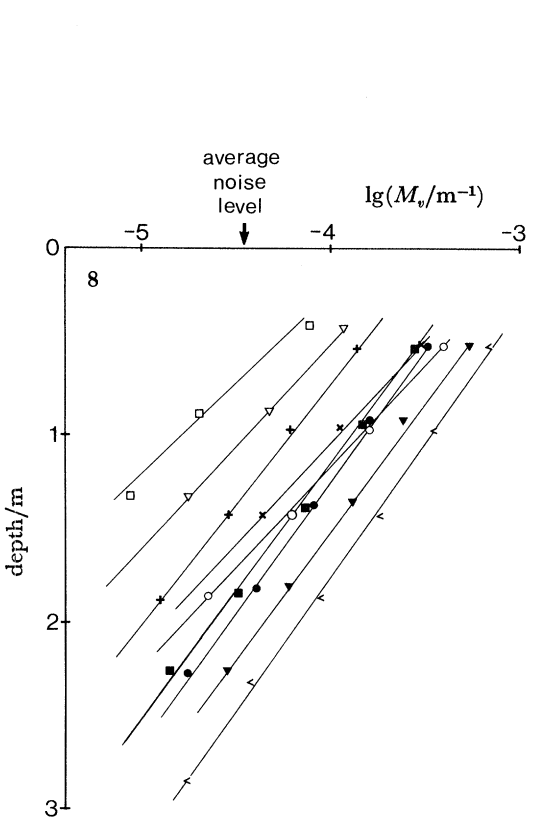

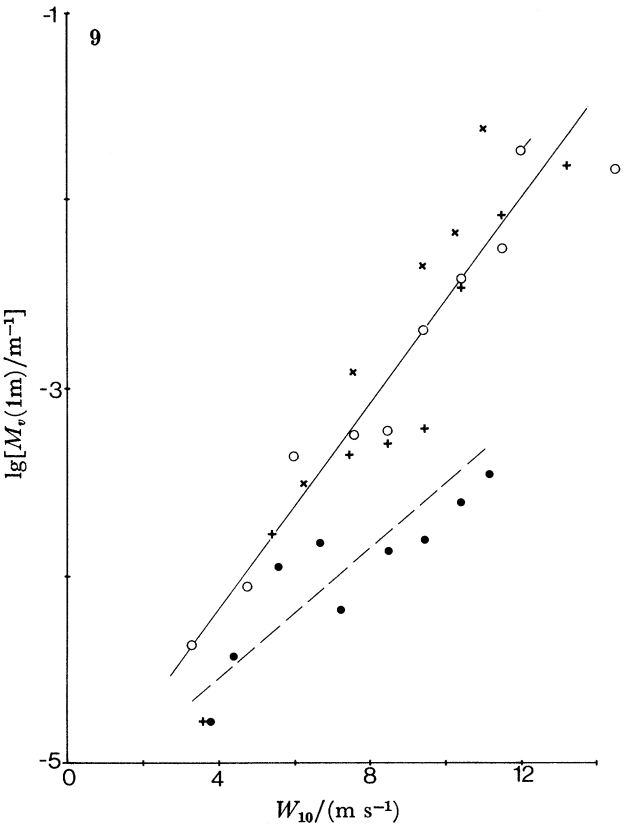

FIGURE 8. Logarithm of the average value of M_v from Loch Ness against depth at various wind speeds (m s^{-1}): □, 3.69; ▽, 4.40; +, 5.57; ○, 6.64; +, 7.16 ■, 8.48; ●, 9.45; ▼, 10.42; <, 11.13.

FIGURE 9. Logarithm of the average value of M_v at 1 m depth against wind speed in Loch Ness (●) and at Oban (○). Values for southwesterly and westerly fetches (×) and northeasterly and northwesterly fetches (+) at Oban are also shown. The symbol ♂ marks the measurement by Johnson & Cooke (1979) in winds of 11–13 m s^{-1}.

The average depth, measured over one hour, at which M_v decreases to the average noise level, 3.5×10^{-5} m^{-1}, is shown against wind speed in figure 10*a* with different symbols representing various air–water temperature differences, $\Delta\theta$. The data were interpolated exponentially when this depth lay outside the observed depth range. A general increase in depth with wind speed is apparent (the mean trend can be seen in figure 8), as observed by Thorpe & Stubbs (1979) (see equation (1)), although they based their analysis on the cloud depths determined from sonagraph records. Generally the average depth is increased by negative $\Delta\theta$. The points are fitted approximately by

$$d = 0.31(1 - 0.1\,\Delta\theta)\,(W_{10} - 2.5) \qquad (6)$$

for $|\Delta\theta| < 6$ K, where d is the average depth (in m) and W_{10} is the wind speed (in m s^{-1}). The maximum depths at which M_v reaches the noise level over one-hour periods are shown in figure 10*b*. The number, and scatter, of points give some indication of the time needed before a cloud will be observed to extend to a given depth.

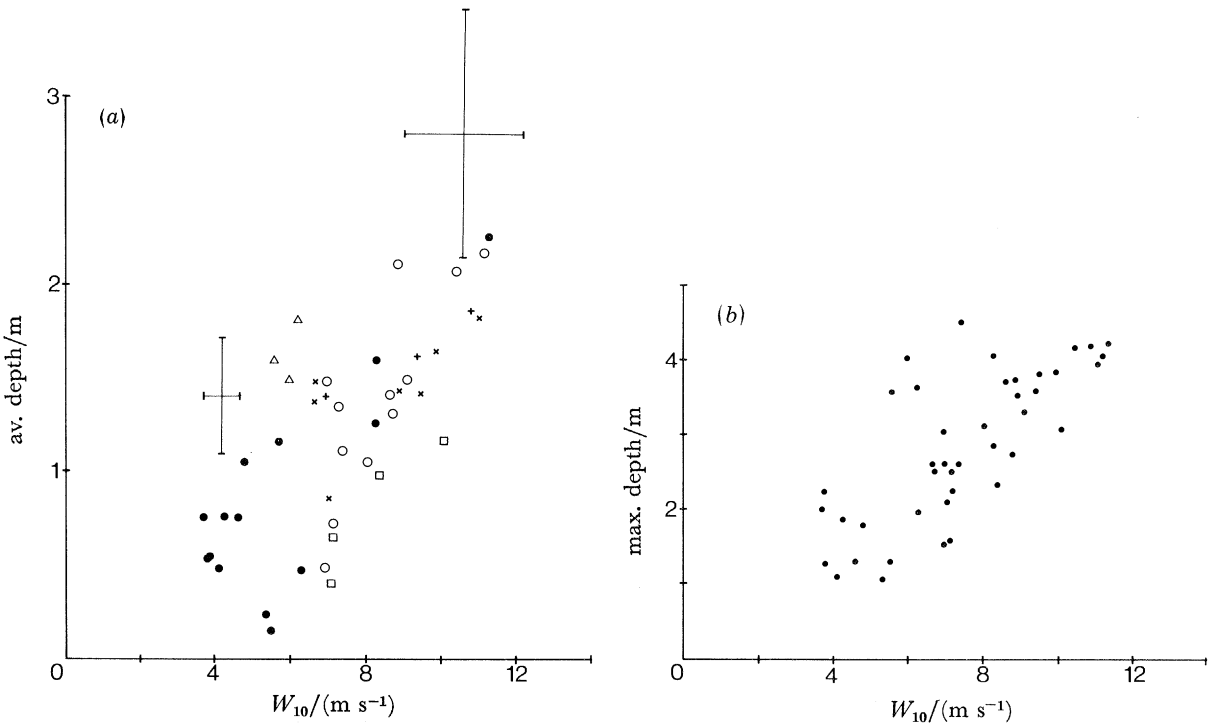

FIGURE 10. (*a*) The average depths, measured over an hour, at which M_v reached the average noise level in Loch Ness in different wind speeds for various values of $\Delta\theta$/K: △, < -3; +, -3 to -1; ●, -1 to 1; ×, 1 to 3; ○, 3 to 5; □, > 5. Standard deviations in wind and depth are shown at two wind speeds.

(*b*) The maximum depths, each point measured over an hour, at which M_v reached the average noise level in Loch Ness at different wind speeds.

2.3. *Oban: bubbles in salt water*

Figures 11–13 show records illustrating the variety of cloud forms observed at Oban between August 1980 and January 1981.

Figures 11*a–c* show bubbles produced during periods when the wind was from the southwest, the direction of largest fetch. The clouds at large winds (more than 10 m s^{-1}) penetrate deeper than those in Loch Ness, and gaps are sometimes visible between clouds through which the water surface can be seen. The undulations in the surface and in the bottom of the clouds (especially in figure 11*c*) are due to swell which was absent in Loch Ness. The horizontal lines (the upper pair mark the range of the six bins and the lower, where shown, the position of the noise bin) change level with the tide, which is falling in all three figures, as explained in § 2.1. In contrast, figures 12*a* and *b* for south and southeast fetches are not dissimilar from those from Loch Ness, and the cloud shapes show the effects of air–water temperature difference. Figures 13*a–c* show bubble clouds in increasingly strong northeasterly and northwesterly winds. The 10 s averaging interval in M_v is too long for us to be able to distinguish details of the cloud structure in figure 13*a*.

The variation of $\overline{M}_v$ with depth at various wind speeds is shown in figure 14 and may be compared with figure 8 from Loch Ness. Similar trends are apparent, but the values of $\overline{M}_v$ are generally much higher in the salt than in the fresh water. This is emphasized in figure 9 where values at 1 m depth can be directly compared. The slopes of the curves in figure 14 increase with wind speed, corresponding to an exponential decay with depth over about 42 cm in winds of

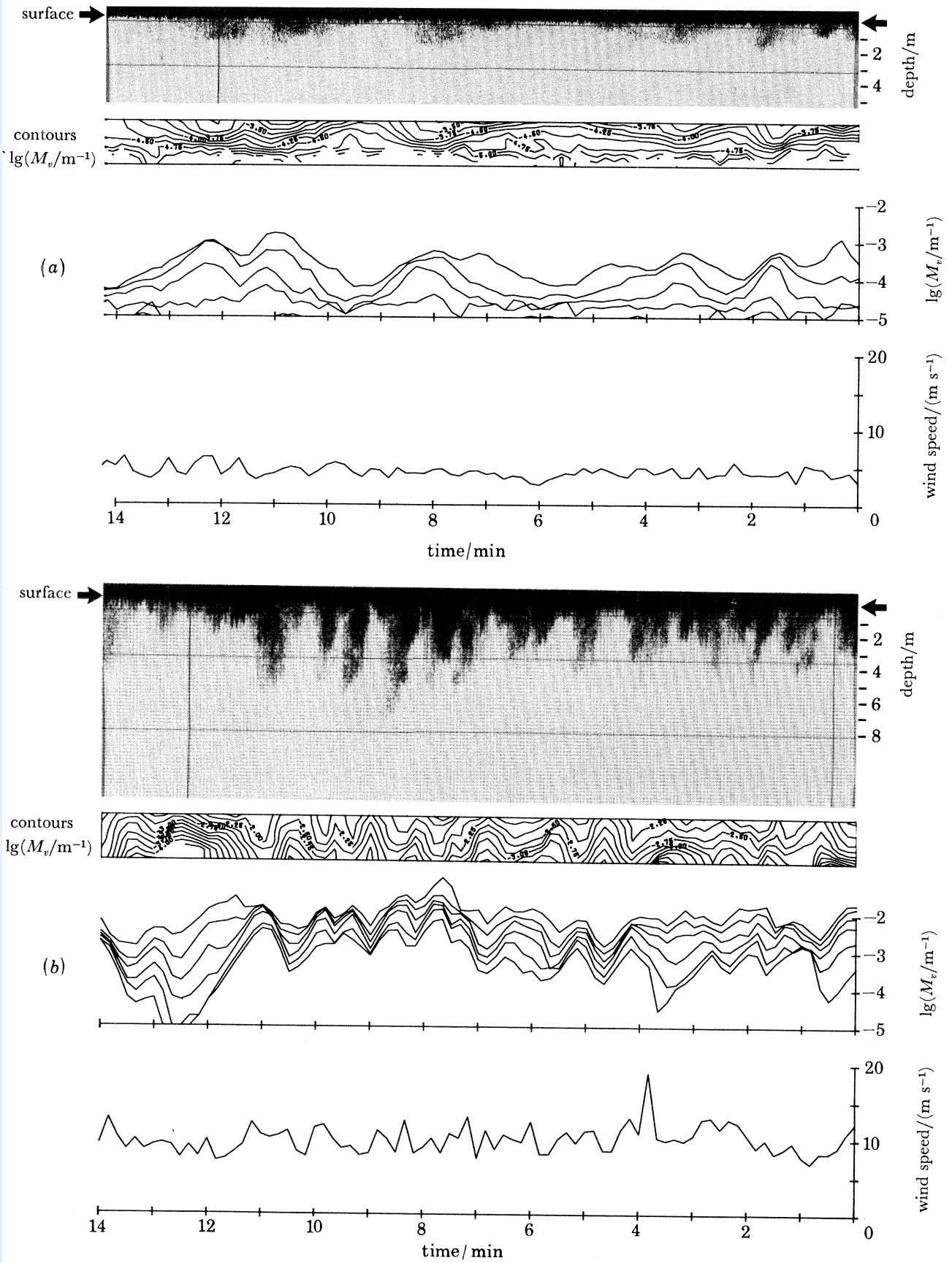

FIGURE 11(*a*) and (*b*). For description see page 172.

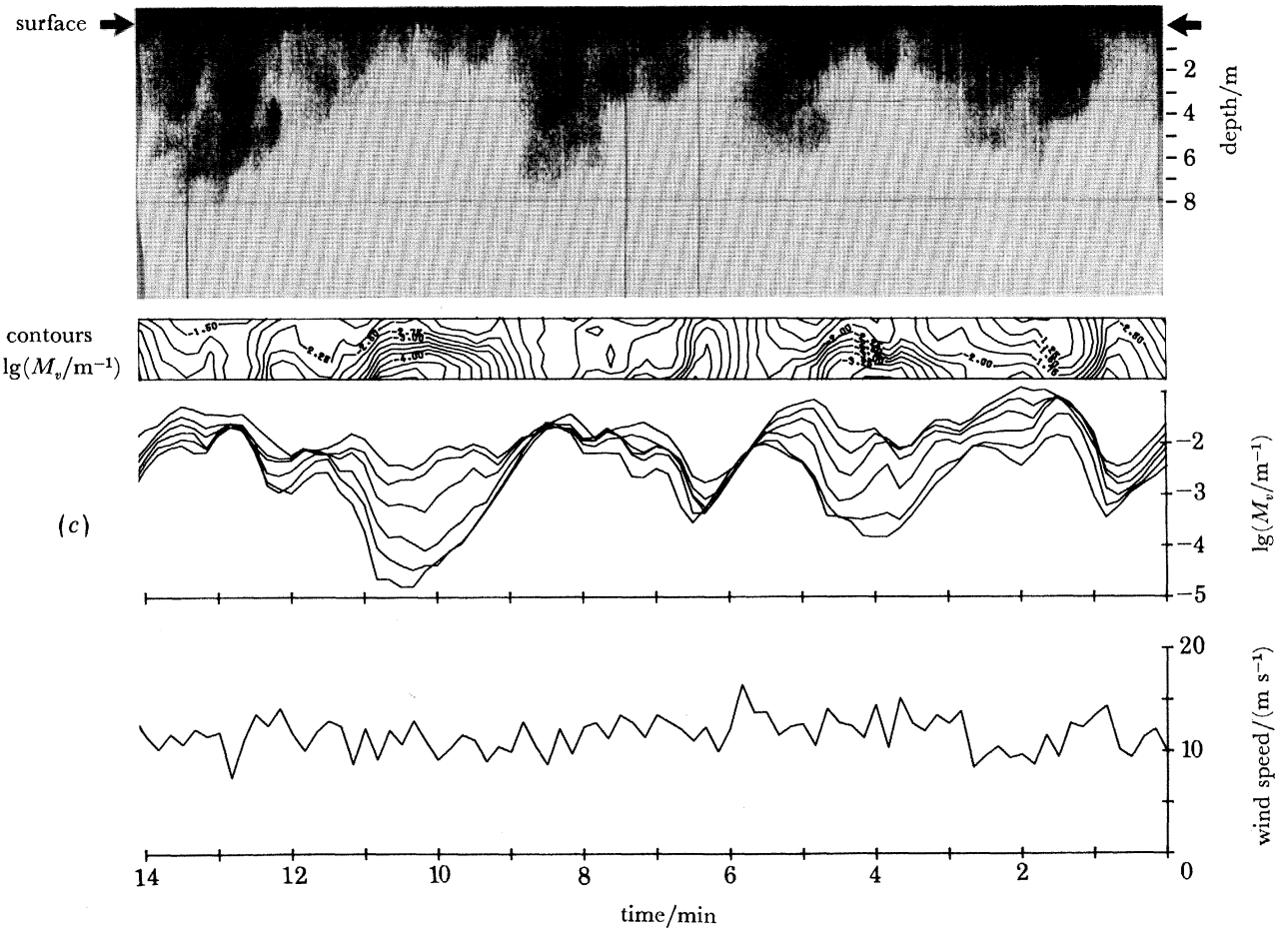

FIGURE 11. Sonagraph, M_v, and wind records from Oban in southwesterly winds: (*a*) $\Delta\theta = -0.4$ K; (*b*) $\Delta\theta = -1.2$ K; (*c*) $\Delta\theta = -1.8$ K.

3–8 m s^{-1} and 75 cm for winds of 9–12 m s^{-1} (see figure 28). Johnson & Cooke's (1979) observations (see table 1) are included in figures 9 and 14 and appear to be reasonably consistent with the present observations, in both their magnitude and trend with depth.

Figures 15*a* and *b* compare the mean and maximum depths of bubble clouds, determined as in figure 10, for various fetches. The mean noise level was 6.0×10^{-5} m^{-1}. There is an increase in cloud depth with wind speed (the mean trend is seen in figure 14) and clouds occasionally extend to about twice the mean cloud depth. At low wind speeds (less than 7 m s^{-1}) there appears to be little variation of depth with fetch, but above 9 m s^{-1} bubbles penetrate, on average, deeper at the larger fetch and there is some indication that the mean depth may increase more rapidly with wind speed as the wind increases. More data are needed to confirm this trend. The effect of air–water temperature difference is in accordance with the results from Loch Ness.

Data for southwesterly and westerly winds were all obtained at air–water temperature differences between 2 K and −2 K. The average depths exceed those observed in Loch Ness, being fitted approximately by

$$d = 0.4(W_{10} - 2.5), \tag{7}$$

though with some scatter. Comparison of figures 10*b* and 15*b* (it being remembered, however, that the noise levels are different) shows that the maximum depth of penetration of bubble

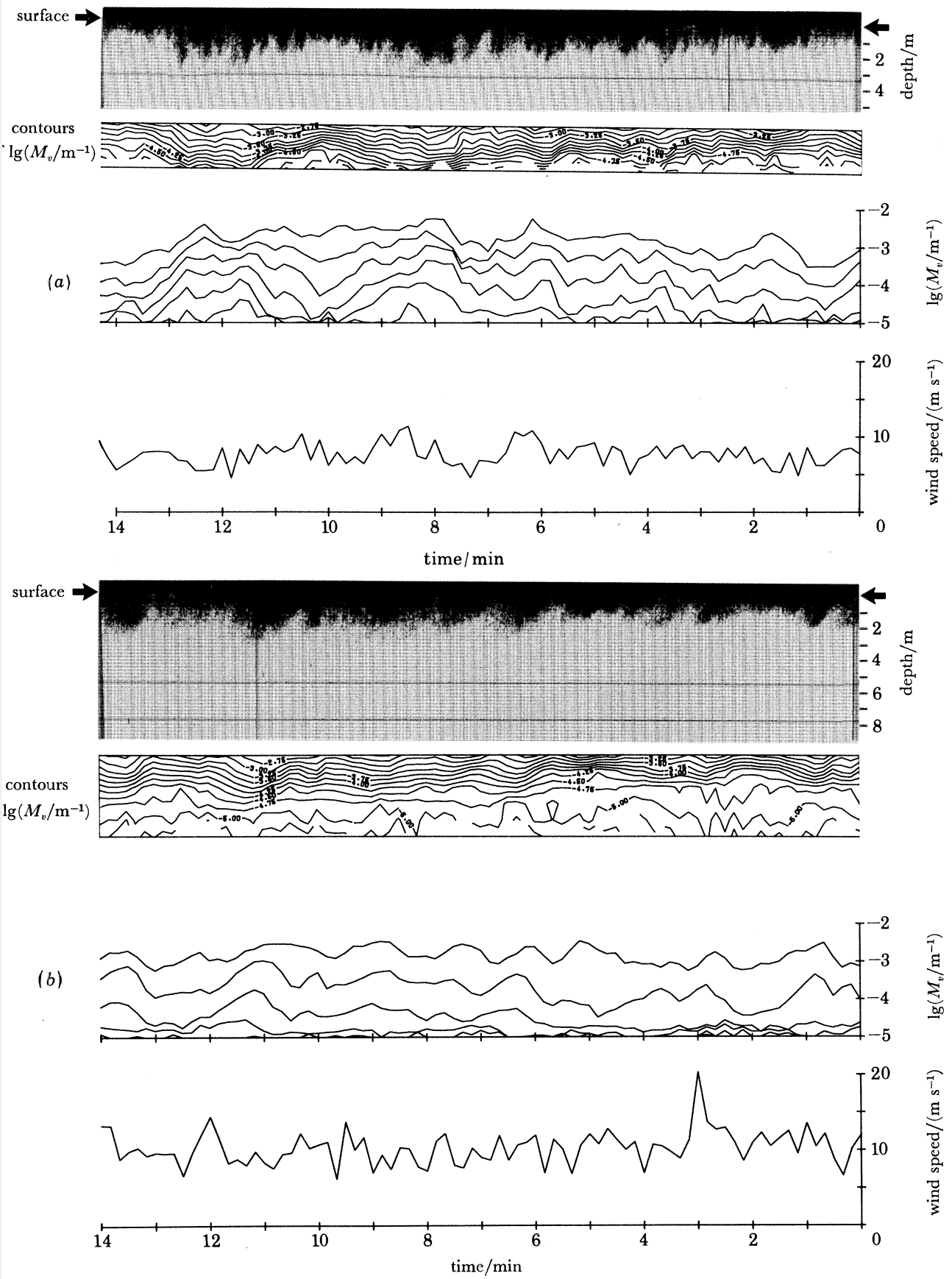

FIGURE 12. Sonagraph, M_v, and wind records from Oban in (*a*) southerly and (*b*) southeasterly winds: (*a*) $\Delta\theta = -2.4$ K (unstable conditions); (*b*) $\Delta\theta = 1.3$ K (stable conditions).

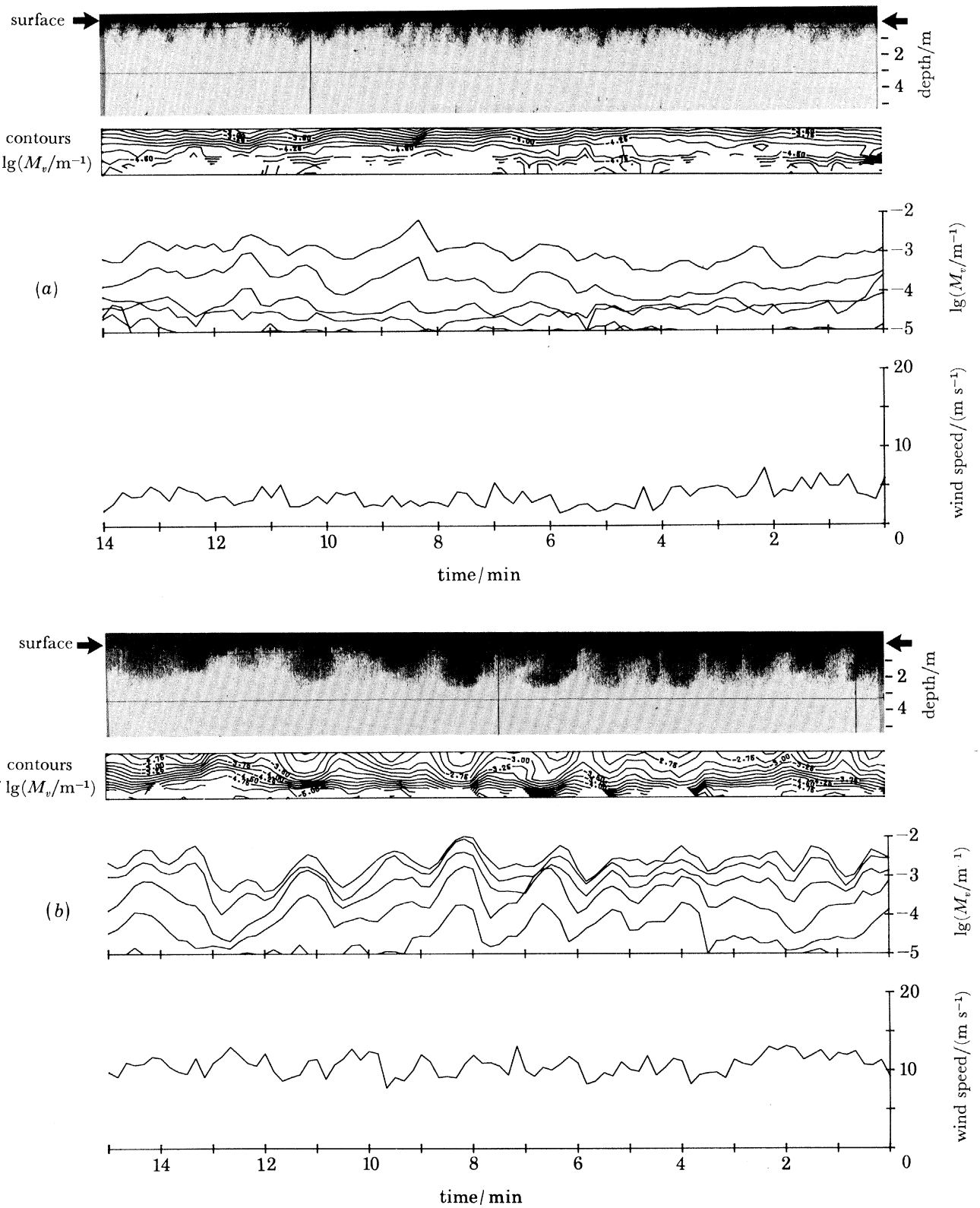

FIGURE 13(*a*) and (*b*). For description see opposite.

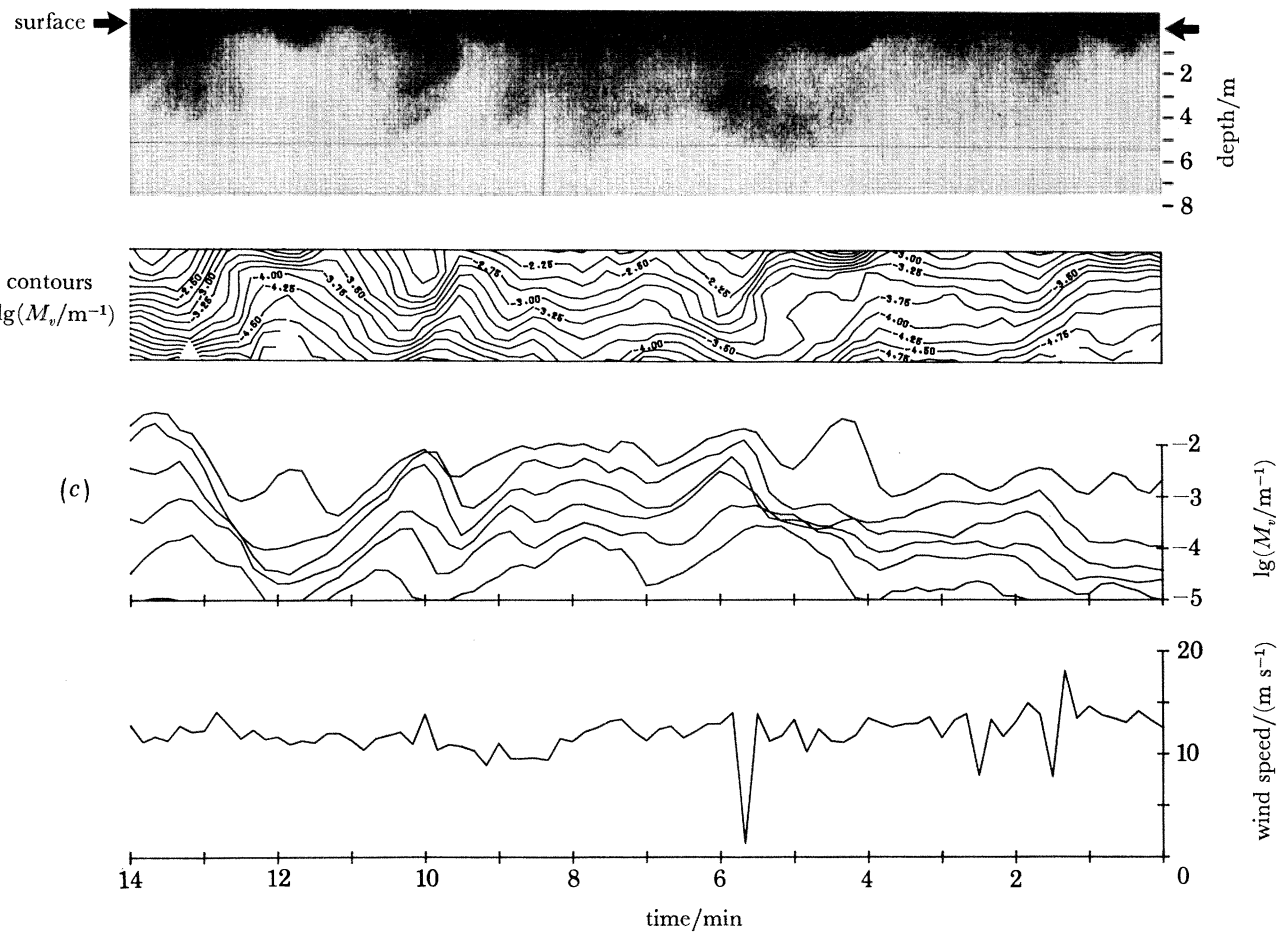

FIGURE 13. Sonagraph, M_v, and wind records from Oban in (*a*), (*c*) northeasterly and (*b*) northwesterly winds: (*a*) $\Delta\theta = -2.0$ K; (*b*) $\Delta\theta = -1.8$ K; (*c*) $\Delta\theta = -3.4$ K. The low value of wind speed at about 5.7 min is due to a fault in the anemometer.

clouds is similar in Loch Ness and Oban for wind speeds less than about 7 m s^{-1} but that at higher wind speeds bubbles penetrate deeper at sea than they do in the Loch.

3. THEORY: DYNAMICS OF INDIVIDUAL BUBBLES

The interpretation of the observations in terms of turbulent diffusion of clouds of bubbles (which we shall discuss in § 4), depends on the dynamics of, and gas flux from, individual bubbles.

3.1. *Bubble rise speeds*

We suppose that the water surrounding a bubble has a downward component of velocity, w. The bubble, being buoyant, will rise through the water at some speed w_b, so that its actual descent rate is given by

$$dp/dt = g\rho(w - w_b), \tag{8}$$

where $p = p_0 + g\rho d$ is the pressure in the water at depth d below the surface where the atmospheric pressure is p_0, g is the acceleration due to gravity and ρ is the water density.

The rise speed, w_b, and also the rate of transfer of gas across the surface of the bubble, depend on the state of the surface of the bubble. In natural bodies of water small bubbles rapidly absorb

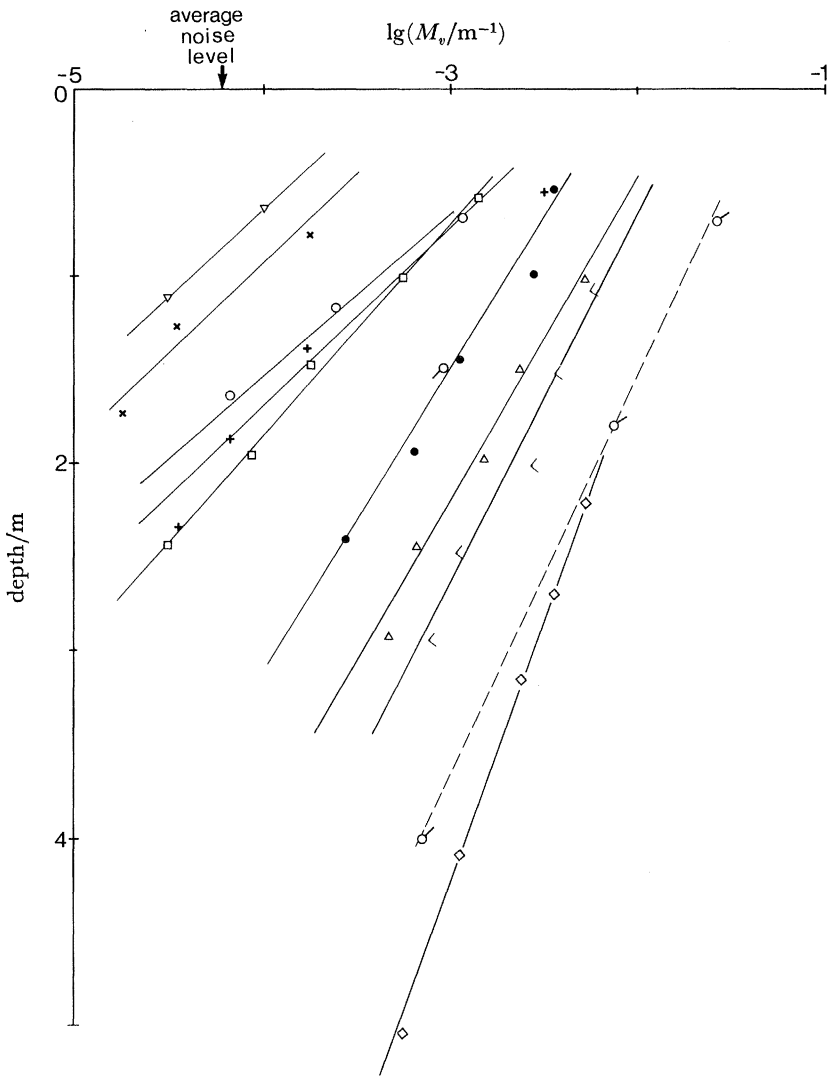

FIGURE 14. Logarithm of the average value of M_v from Oban against depth at various wind speeds: ▽, 3.25 m s^{-1}; ×, 4.75 m s^{-1}; ○, 5.99 m s^{-1}; +, 7.52 m s^{-1}; □, 8.42 m s^{-1}; ●, 9.41 m s^{-1}; △, 10.42 m s^{-1}; <, 11.51 m s^{-1}. The symbols ♀ and ♂ are from measurements by Johnson & Cooke (1979) at 8–10 and 11–13 m s^{-1} respectively; see table 1. The figure includes points, ◇, corresponding to data collected over five periods of three hours when the mean wind averaged 14.51 m s^{-1}. In each period the wind was southeasterly (the shortest fetch), and the wind speeds were determined from the anemometer at the Scottish Marine Biological Association, some 450 m away from the anemometer mounted at the shoreline used for the other wind observations, and sheltered in southeasterly winds by a ridge to the southeast. The average air temperature for these data is estimated to be 2.5 K below the water temperature.

surface-active material onto their surface (Detwiler & Blanchard 1978; Detwiler 1979) which can then sustain a stress. Once this material covers the surface, the bubble behaves dynamically like a rigid body. We shall call such bubbles 'dirty bubbles' to distinguish them from those carrying no surface-active material which are called 'clean bubbles'. Clean bubbles of radii less than about 100 μm become dirty in a few tens of seconds, and since this, as we shall see, is often a small part of their lifetime we may consider them as being always dirty. On larger bubbles the surface-active material forms a cap which changes the stress over part of their surface. Large bubbles may behave like 'clean bubbles'. Rather than attempt to describe fully the transition

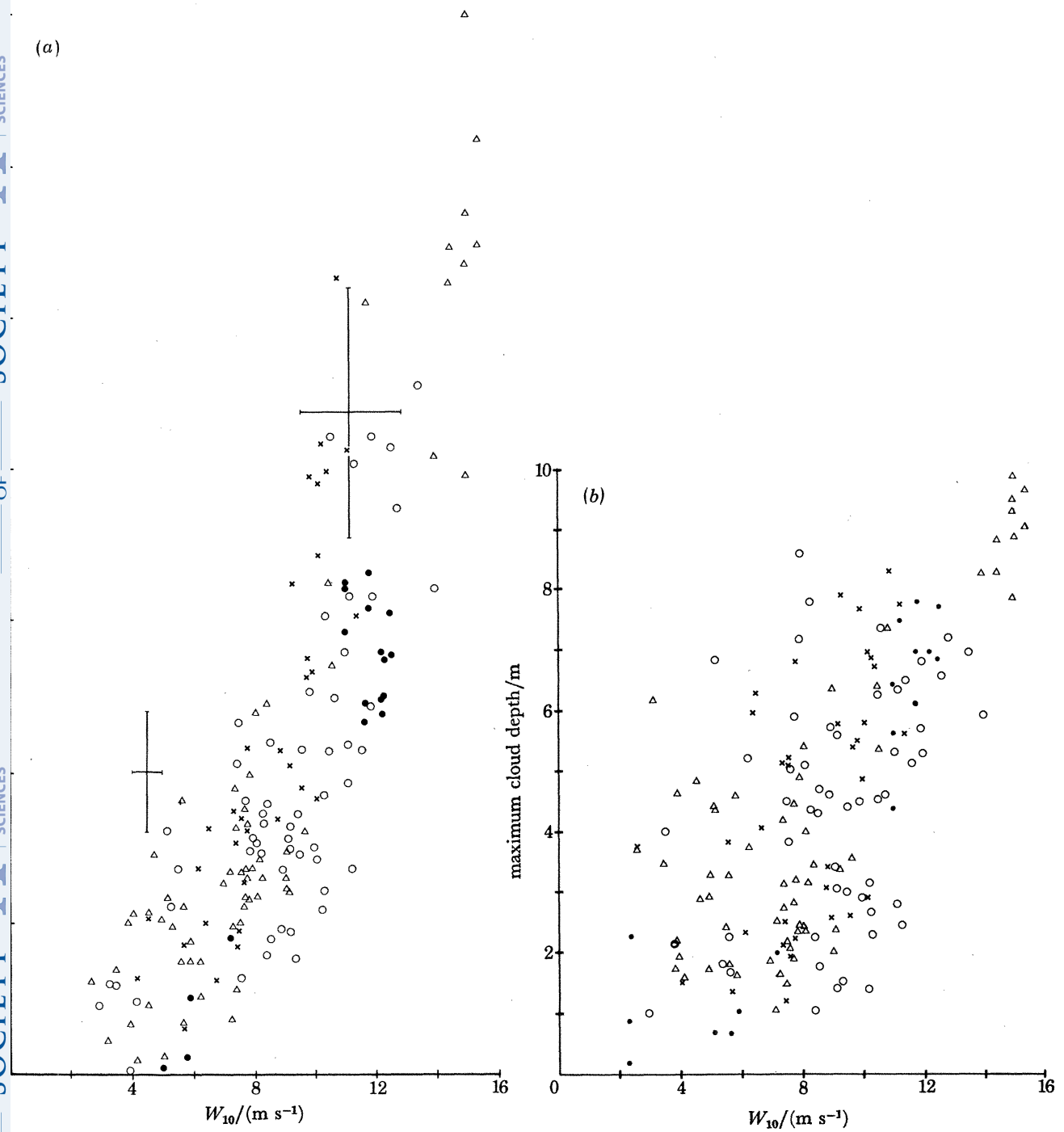

FIGURE 15. (*a*) The average depths, measured over an hour, at which M_v reached the average noise level at Oban in different wind speeds. Standard deviations in wind and depth are shown at two wind speeds.

(*b*) The maximum depths, each point measured over an hour, at which M_v reached the average noise level at Oban in different wind speeds. The symbols in both figures correspond to: △, southerly and southeasterly winds (mean fetch 0.9 km); ●, northerly winds (mean fetch 2.6 km); ○, northeasterly and northwesterly winds (mean fetch 4.3 km); ×, westerly and southwesterly winds (mean fetch exceeding 10 km).

from clean to dirty bubbles (see Davis & Acrivos 1966; Harper 1972) we shall attempt to describe only the two limits. In practice the bubbles will be small and almost spherical. The departure from a spherical shape is given by the Weber number $2\rho w_b^2 a/\gamma$, where γ is the surface tension (see Harper 1972), and is very small for bubbles less than 400 μm in radius.

For clean bubbles of radii less than about 80 μm, the rise speed is given by

$$w_b = \tfrac{1}{3}a^2 g/\nu, \tag{9}$$

where a is the radius and ν the kinematic viscosity (see Batchelor 1967). The bubble Reynolds number is

$$Re = 2aw_b/\nu < 0.33.$$

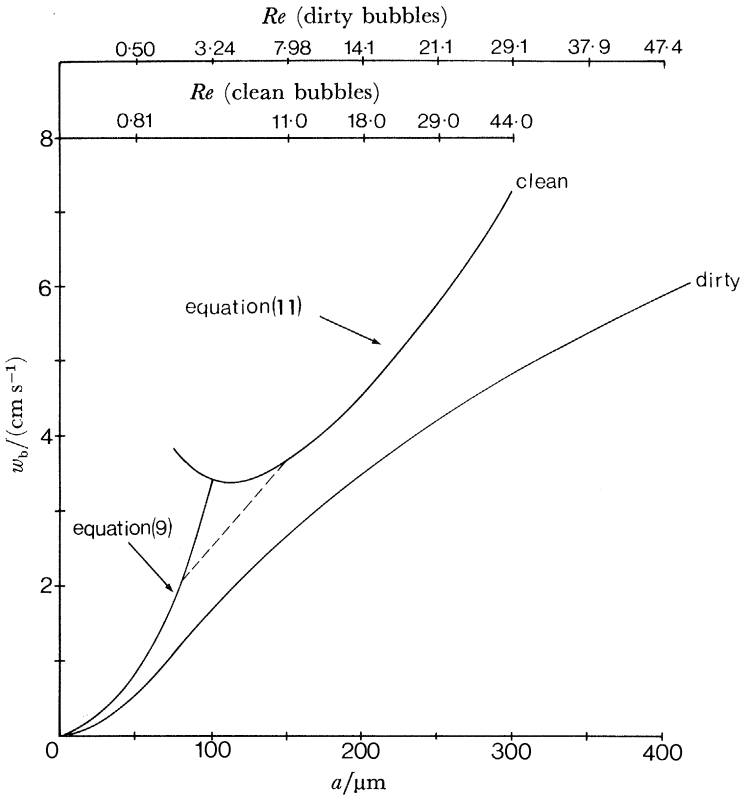

FIGURE 16. The variation of speed of ascent of bubbles, w_b, with radius, a, for 'clean' and 'dirty' bubbles.

For large Re such that $Re^{-\frac{1}{6}} \ll 1$, Moore (1963) has shown that

$$C_d = 48Re^{-1}[1 - 2.21\,Re^{-\frac{1}{2}} + O(Re^{-\frac{5}{6}})], \tag{10}$$

where C_d is the drag coefficient, equal to $4ga/3w_b^2$ (see also Harper 1972). Equation (10) may be rewritten

$$w_b = \frac{1}{18\{1 - 2/[1 + (1 + 0.091\chi)^{\frac{1}{2}}]\}}\,\frac{a^2 g}{\nu}, \tag{11}$$

where $\chi = ga^3/\nu^2$, $O(\mathrm{Re}^{-\frac{5}{6}})$ terms being neglected. These curves are shown in figure 16 for $g = 9.81\,\mathrm{m\,s^{-2}}$ and $\nu = 1 \times 10^{-6}\,\mathrm{m^2\,s^{-1}}$. In the subsequent numerical examples we interpolate linearly between the curves joining the points where $a = 80\,\mu\mathrm{m}$ (small Re) and $a = 150\,\mu\mathrm{m}$ (large Re).

The rise of dirty bubbles, effectively solid spheres, is described by Batchelor (1967). A good approximation to the empirical curve is

$$C_d = 12Re^{-1}(1 + 0.104\,Re), \tag{12}$$

for $Re \lesssim 10$, which we can write as

$$w_b = \tfrac{2}{9}(a^2g/\nu)\,[(y^2 + 2y)^{\frac{1}{2}} - y], \tag{13}$$

for $a \lesssim 180\,\mu m$, where $y = 10.82/\chi$ (w_b tends to $2a^2g/9\nu$ as χ tends to zero). This curve is also shown in figure 16. It tends to underestimate w_b at higher values of a, by about 20 % at radii of 400 μm. For $a \lesssim 80\,\mu m$ the rise speed of both clean and dirty bubbles is closely proportional to a^2. Most bubbles observed by Johnson & Cooke (1979) indeed have radii less than 80 μm and will be described either by (9) (for a short period), or by (13). At 0.7 m depth, however, in wind speeds of 11–13 m s^{-1} bubbles of sizes extending to 300 μm were found.

If $w_b > w$ in (8), the bubbles will not be carried downwards by the current, but will rise. The curves of figure 16 show that for a given vertical velocity all bubbles smaller than a critical radius (for which $w = w_b$) will be carried down. The critical radius of dirty bubbles is greater than that of clean bubbles.

3.2. *Gas diffusion from bubbles*

We shall suppose that the gas contained in the bubbles is composed of a mixture of oxygen and nitrogen which, at the surface, are in approximately the ratio 7:26, appropriate to air. The presence of other gases in the bubbles may be neglected, provided that they diffuse at rates comparable with those of oxygen and nitrogen, or, if they are present in such small quantities that when they eventually become major components of the gas within the bubbles (other gases having diffused out), the bubble size will be less than that which can be detected by the sonar (that is less than about 10 μm in radius).

Following Wyman *et al.* (1952), if x is the mole fraction of oxygen in the bubble and n_1 is the number of moles of oxygen (subscripts 2 will refer to nitrogen),

$$n_1 = \frac{4\pi a^3 x}{3RT}\left(p + \frac{2\gamma}{a}\right), \tag{14}$$

where $p + 2\gamma/a$ is the pressure of the gas inside the bubble, R is the gas constant (in m^3 kPa K^{-1} mol^{-1}) and T is the temperature (K). It is assumed that the water is isothermal, and the gas in the bubbles has the same temperature. This may be justified for the bubble sizes considered here, because the diffusion coefficient of heat is an order of magnitude greater than that of the gases in the bubbles, and hence the bubbles rapidly attain the water temperature. The term $2\gamma/a$ is the enhancement of the pressure in the bubble due to the surface tension, γ. The surface tension will depend on the state of the bubble surface, perhaps being lowered if the bubble is dirty. Similarly for nitrogen,

$$n_2 = \frac{4\pi a^3(1-x)}{3RT}\left(p + \frac{2\gamma}{a}\right). \tag{15}$$

Consider now diffusion of gas from the bubble. We let Nu be the value of the Nusselt number which we shall suppose is independent of the rate at which the pressure, p, varies; there is evidence to show that diffusion can be affected by very rapid changes, but in the sea the changes will be relatively slow. At high Péclet number, Pe (radii greater than about 20 μm), but small Re,

$$Nu = \frac{Q}{4\pi a D(C - C_\infty)} = \begin{cases} (2/3\pi)^{\frac{1}{2}}\,Pe^{\frac{1}{2}} & \text{(for clean bubbles)} \quad (16) \\ (2/\pi)\,Pe^{\frac{1}{3}} & \text{(for dirty bubbles)} \quad (17) \end{cases}$$

(Levich 1962; see also Garrettson 1973) where

$$Pe = aw_b/D, \tag{18}$$

Q is the rate of transfer of gas from the bubble surface, D is the diffusivity of bubble gas in water, C is the concentration of gas in the bubble and C_∞ is the concentration in the water far from the bubble. For dirty bubbles at small Pe (radii less than about 10 μm)

$$Nu = 1 + \tfrac{1}{2}Pe + \tfrac{1}{2}Pe^2 \ln 2Pe + 0.06808\,Pe^2 + \tfrac{1}{2}Pe^3 \ln 2Pe + \ldots, \tag{19}$$

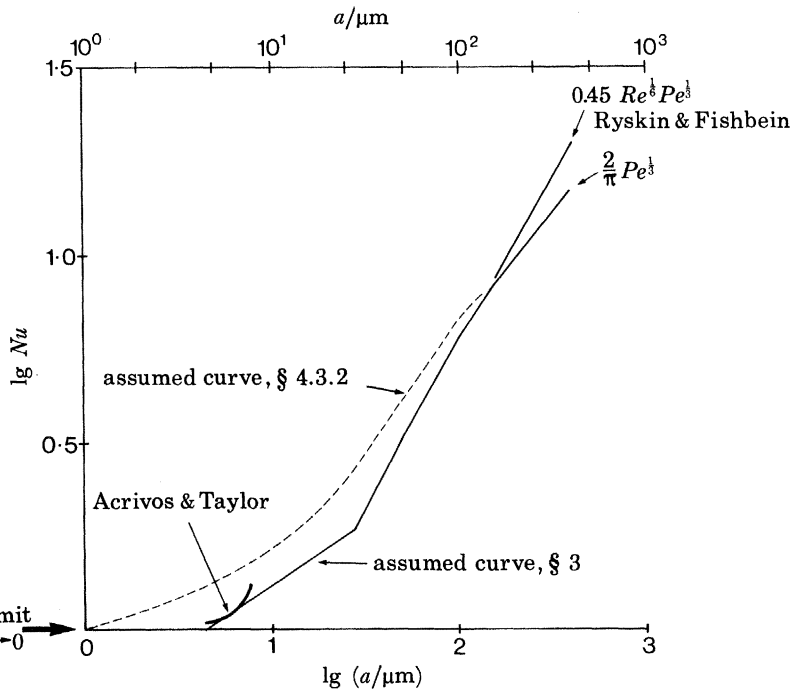

FIGURE 17. The variation of Nusselt number, Nu, with bubbles of radius, a, for dirty bubbles.

(Acrivos & Taylor 1962). (Note that Nu tends to unity as Pe tends to zero for both clean and dirty bubbles.) The curves for dirty bubbles are shown in figure 17, plotted as the variation of Nu with bubble radius, a. In the numerical experiments described later we have taken the curve

$$Nu = 1.292\,Pe^{\frac{1}{6}}$$

to represent the variation for dirty bubbles in the range $4.5 < a/\mu\text{m} < 28.1$. The semi-empirical curve $Nu = 0.45Re^{\frac{1}{6}}Pe^{\frac{1}{3}}$ of Ryskin & Fishbein (1976) shown in figure 17 predicts an increased diffusion rate at high Pe and $Re > 10$ amounting to about 34 % for bubbles of radius 400 μm.

It is pertinent to note here that for dirty bubbles in a statistically steady turbulent flow, Batchelor (1980) has shown that

$$Nu = 0.55Pe^{\frac{1}{3}}, \tag{20}$$

where now $Pe = a^2\epsilon^{\frac{1}{2}}/D\nu^{\frac{1}{2}} \gg 1$, the Reynolds number is small, and ϵ is the rate of dissipation of turbulent kinetic energy per unit mass. Whether (17) or (20) applies when the relevant Pe is much greater than unity depends on whether the r.m.s. vorticity in the turbulent flow, $(\epsilon/\nu)^{\frac{1}{2}}$, is less than or greater than order ϕ, where

$$\phi = (\tfrac{4}{81}g^2D/\nu^2)^{\frac{1}{3}}.$$

Taking typical values $D = 2 \times 10^{-9}\,\text{m}^2\,\text{s}^{-1}$ and $\nu = 1 \times 10^{-6}\,\text{m}^2\,\text{s}^{-1}$ we find $\phi = 21\,\text{s}^{-1}$.

There are very few observations of ϵ close to the surface of the sea. Stewart & Grant (1962) found a maximum value of $4.2 \times 10^{-6}\,\mathrm{m^2\,s^{-3}}$ at 1 m depth. The indirect observations of Dillon & Caldwell (1980) and Caldwell *et al.* (1980) suggest values that are not much greater in winds up to $16\,\mathrm{m\,s^{-1}}$, and in lakes where the wind fetch is less, smaller values might be expected (see for example Thorpe 1977). Except very close to the surface, within the top 1 m and in strong winds, it seems therefore likely that, on average, the r.m.s. turbulent vorticity will be less than order ϕ, so that (17) will hold even though the fluid surrounding the (dirty) bubble is turbulent. No comparable theory exists for clean bubbles in turbulent flow.

For bubble radii less than about 80 μm, which includes most of those observed, Pe (in (18)) is proportional to a^3. Hence for the dirty bubbles in the sea or in lakes with radii in the range 20–80 μm, Nu is proportional to a and hence the gas flux, Q, is proportional to a^2, that is to the bubble area. This result will be important when we estimate the gas flux from the bubble clouds.

If κ is the coefficient of absorption of the gas, $C = \kappa P$ and $C_\infty = \kappa P_\infty$, where P is the partial pressure of the gas in the bubble and P_∞ that in the surrounding water. Hence from the definition of the Nusselt number we may write

$$\mathrm{d}n_1/\mathrm{d}t = -4\pi a D_1 \kappa_1 N_1 [x(p + 2\gamma/a) - p_{10}], \tag{21}$$

and

$$\mathrm{d}n_2/\mathrm{d}t = -4\pi a D_2 \kappa_2 N_2 [(1-x)(p + 2\gamma/a) - p_{20}], \tag{22}$$

where $N_i (i = 1, 2)$ are the Nusselt numbers and p_{i0} $(i = 1, 2)$ are the partial pressures of oxygen and nitrogen respectively in the water far from the bubble, which we shall suppose are constant. It may be shown that the changes in these pressures occur on time scales far in excess of those that affect individual bubbles.

Equations (14), (15), (21) and (22) can be combined to give

$$\frac{\mathrm{d}a}{\mathrm{d}t} = \frac{-1}{(3p + 4\gamma/a)} \left\{ \frac{3RT}{a} \left[D_1 \kappa_1 N_1 \left(x \left(p + \frac{2\gamma}{a} \right) - p_{10} \right) + D_2 \kappa_2 N_2 \left((1-x) \left(p + \frac{2\gamma}{a} \right) - p_{20} \right) \right] + a \frac{\mathrm{d}p}{\mathrm{d}t} \right\}, \tag{23}$$

and

$$\frac{\mathrm{d}x}{\mathrm{d}t} = \frac{3RT}{a^2 (p + 2\gamma/a)} \left\{ D_2 \kappa_2 N_2 x \left[(1-x) \left(p + \frac{2\gamma}{a} \right) - p_{20} \right] - D_1 \kappa_1 N_1 (1-x) \left[x \left(p + \frac{2\gamma}{a} \right) - p_{10} \right] \right\}. \tag{24}$$

We have neglected the possibility of a growth in the size of the bubble by coalescence with other bubbles. (In the dynamics of clouds in the atmosphere the coalescence of neighbouring drops, with a consequent change in the distribution of droplet sizes, is an important factor.) In the most extreme conditions observed by Johnson & Cooke, the bubble density was $1.56 \times 10^5\,\mathrm{m^{-3}}$. The mean distance between bubbles was thus about 1.8 cm which is large compared with the mean radius, about 50 μm. This alone suggests that bubble collision will be infrequent. A further measure can be obtained by using the theoretical formula derived by Saffman & Turner (1956). In a turbulent flow containing particles of radius a_j and a_k with densities n_j and n_k respectively, the number of collisions per unit time per unit volume, N_{jk}, is given approximately by

$$N_{jk} = 1.3(\epsilon/\nu)^{\frac{1}{2}} (a_j + a_k) n_j n_k.$$

Taking $\epsilon \approx 5 \times 10^{-6}\,\mathrm{m^2\,s^{-3}}$, $\nu = 1.0 \times 10^{-6}\,\mathrm{m^2\,s^{-1}}$, $a_j = a_k \approx 50\,\mu\mathrm{m}$ and $n_j = n_k \approx 1.56 \times 10^5\,\mathrm{m^{-3}}$, we find that $N_{jk} \approx 0.09\,\mathrm{s^{-1}\,m^{-3}}$, which is negligible. This ignores the capture of small bubbles by rising larger bubbles but, even so, suggests that except very close to the surface in the zone where the waves are breaking and bubbles are being formed, coalescence may be neglected.

3.3. *Typical values*

In the subsequent calculations we take the following typical values of the various quantities appearing in the equations:

$$\nu = 1.0\times10^{-6}\,\mathrm{m^2\,s^{-1}},\quad D_1 = D_2 = 2\times10^{-9}\,\mathrm{m^2\,s^{-1}},$$

$$\kappa_1 = 0.49\,\mathrm{g\,m^{-3}\,kPa^{-1}},\quad \kappa_2 = 0.21\,\mathrm{g\,m^{-3}\,kPa^{-1}},$$

$$R = 8.31\times10^{-3}\,\mathrm{m^3\,kPa\,K^{-1}\,mol^{-1}},\quad T = 283\,\mathrm{K},$$

$$g = 9.81\,\mathrm{m\,s^{-2}},\quad \gamma = \begin{cases} 7.2\times10^{-2}\,\mathrm{N\,m^{-1}} & \text{for clean bubbles} \\ 3.6\times10^{-2}\,\mathrm{N\,m^{-1}} & \text{for dirty bubbles.} \end{cases}$$

The value of x at the surface, where the pressure is one atmosphere (*ca.* 10^2 kPa), is taken as 0.215. Some of the values (of ν, γ, D_1, κ, etc.) are functions of temperature, salinity or pressure, but the variations found during the observations (even of salinity) produce only small changes in the results. The value of γ for dirty bubbles is extreme, but again results are not very sensitive to the actual value chosen.

Using these values we may determine the relative size of the term appearing in (23). We take values appropriate to dirty bubbles of radius 50 μm (typical of those observed by Johnson & Cooke) that are saturated in oxygen and nitrogen with respect to the pressure at the surface. Then $w_b = 0.54\,\mathrm{cm\,s^{-1}}$ and if

$$|w - w_b| \approx 1\,\mathrm{cm\,s^{-1}},$$

at 1 m depth the diffusive terms exceed the advective terms ($a\,\mathrm{d}p/\mathrm{d}t$) by a factor of about 19. This factor will increase as the depth increases. It thus appears that, except close to the surface, the rate of change of the size of the bubbles is controlled not by Boyle's law but by diffusive processes, and it is likely that these determine the size distribution of bubbles found in the sea.

3.4. *A model of bubble advection*

Equations (8), (23) and (24) with appropriate choices of w_b, N_1 and N_2, now together define the vertical motion of the bubble, and its change in radius and composition with time. A steady state exists when $w = w_b$ and the right sides of (23) and (24) are zero; that is when the bubble rise speed equals the vertical water speed and when the partial pressures of the gases inside and outside the bubbles are equal. Consider for example a bubble composed entirely of nitrogen, with $x = p_{10} = 0$. Let

$$p_{20} = p_0(1 + 0.01 s_2),$$

so that s_2 is the percentage oversaturation of nitrogen in the water. Equilibrium occurs at a depth given by

$$p_0 + g\rho d + 2\gamma/a = p_{20},$$

that is

$$d = (1/g\rho)\,(0.01 s_2 p_0 - 2\gamma/a), \tag{25}$$

which is greater than zero only if $s_2 > 0$, where $a\,(= a_c)$ is given by the equation $w = w_b$. If, for example, the bubble is dirty and of radius less than 80 μm, $w_b \approx 2a^2 g/9\nu$ and so $a_c \approx 3(w\nu/2g)^{\frac{1}{2}}$. Bubbles at this equilibrium state will, however, be unstable, for if they are perturbed slightly upwards so that p decreases, (23) implies that the radius will increase, so that w_b will increase and, by (8), the bubble will continue to rise. The converse occurs if bubbles are perturbed

downwards. There is a flux of gas into bubbles of critical radius above their equilibrium depth (from (21), (22)) and flux from the bubbles below this depth. For the pure nitrogen bubbles, the equilibrium depth exists only if the water is supersaturated. In general, bubbles will not arrive at an equilibrium depth with the correct radius to satisfy (8) or, if they do, they will not have the composition such that $\mathrm{d}x/\mathrm{d}t = 0$.

An alternative way of regarding (25) is to write

$$s_2 = 100 z_s/H \quad \text{or} \quad p_{20} = p_0 + g\rho z_s,$$

where $H = p_0/g\rho$ is the depth at which the pressure is $2p_0$, and z_s is a 'saturation depth'. Then the equilibrium depth d is given by

$$d = z_s - 2\gamma/a$$

or, with reference to (22),

$$\mathrm{d}n/\mathrm{d}t > 0 \quad \text{if} \quad z_s - z > 2\gamma/a.$$

Hence if the fluid is supersaturated (s_2 and $z_s > 0$), there will be a flux of gas into bubbles shallower than depth z_s and of radius exceeding $2\gamma/(z_s - z)$. For dirty bubbles the critical radius is about 14.4, 7.2, 3.6, 1.8 μm for $z_s - z = 0.5, 1.0, 2.0, 4.0$ m respectively. Bubbles of smaller radius will lose gas.

We cast the governing equations into non-dimensional form, by taking a_0 to be the radius of a bubble at time $t = 0$ at the surface and writing

$$a' = a/a_0, \quad t' = twg\rho/p_0, \quad \Gamma = 2\gamma/a_0 p_0,$$
$$p' = p/p_0, \quad p_{10} = x_0 p_0(1 + 100 s_1), \quad p_{20} = (1 - x_0)\, p_0(1 + 100 s_2)$$

(where x_0 is the mole fraction of oxygen in the air),

$$w_b' = w_b/w, \quad A_i = 3RTp_0 D_i \kappa_i / g\rho w a_0^2 \quad (i = 1, 2),$$

to give (dropping the suffix ′)

$$\frac{\mathrm{d}p}{\mathrm{d}t} = 1 - w_b, \tag{26}$$

$$\frac{\mathrm{d}a}{\mathrm{d}t} = \frac{-1}{a(3p + 2\Gamma/a)} \left\{ A_1 N_1 \left[x\left(p + \frac{\Gamma}{a}\right) - x_0(1 + 100 s_1) \right] + A_2 N_2 \left[(1 - x)\left(p + \frac{\Gamma}{a}\right) - (1 - x_0)(1 + 100 s_2) \right] + a^2 \frac{\mathrm{d}p}{\mathrm{d}t} \right\}, \tag{27}$$

and

$$\frac{\mathrm{d}x}{\mathrm{d}t} = \frac{1}{(p + \Gamma/a)} \left\{ A_2 N_2 x \left[(1 - x)\left(p + \frac{\Gamma}{a}\right) - (1 - x_0)\,(1 + 100 s_2) \right] - A_1 N_1 (1 - x) \left[x\left(p + \frac{\Gamma}{a}\right) - x_0(1 + 100 s_1) \right] \right\}. \tag{28}$$

No general analytic solution of (26) to (28) appears possible. Some special cases are tractable, for example that in which diffusion may be neglected and Γ is negligible, when the bubble volume varies inversely with the depth, or that in which diffusion dominates and advection can be neglected (see Blanchard & Woodcock (1957) in which w_b and x_0 are both taken to be zero). The equations and the corresponding non-dimensional form of the equations for w_b, may, however, be solved numerically by using a Runge-Kutta technique with the parameters determined by the values given in §3.3.

Figure 18*a–c* shows the variation of depth with time of dirty bubbles composed entirely of nitrogen in water that is saturated ($s_2 = 0$) for various values of the vertical velocity w. Bubbles of

PHILOSOPHICAL TRANSACTIONS OF THE ROYAL SOCIETY A MATHEMATICAL, PHYSICAL & ENGINEERING SCIENCES

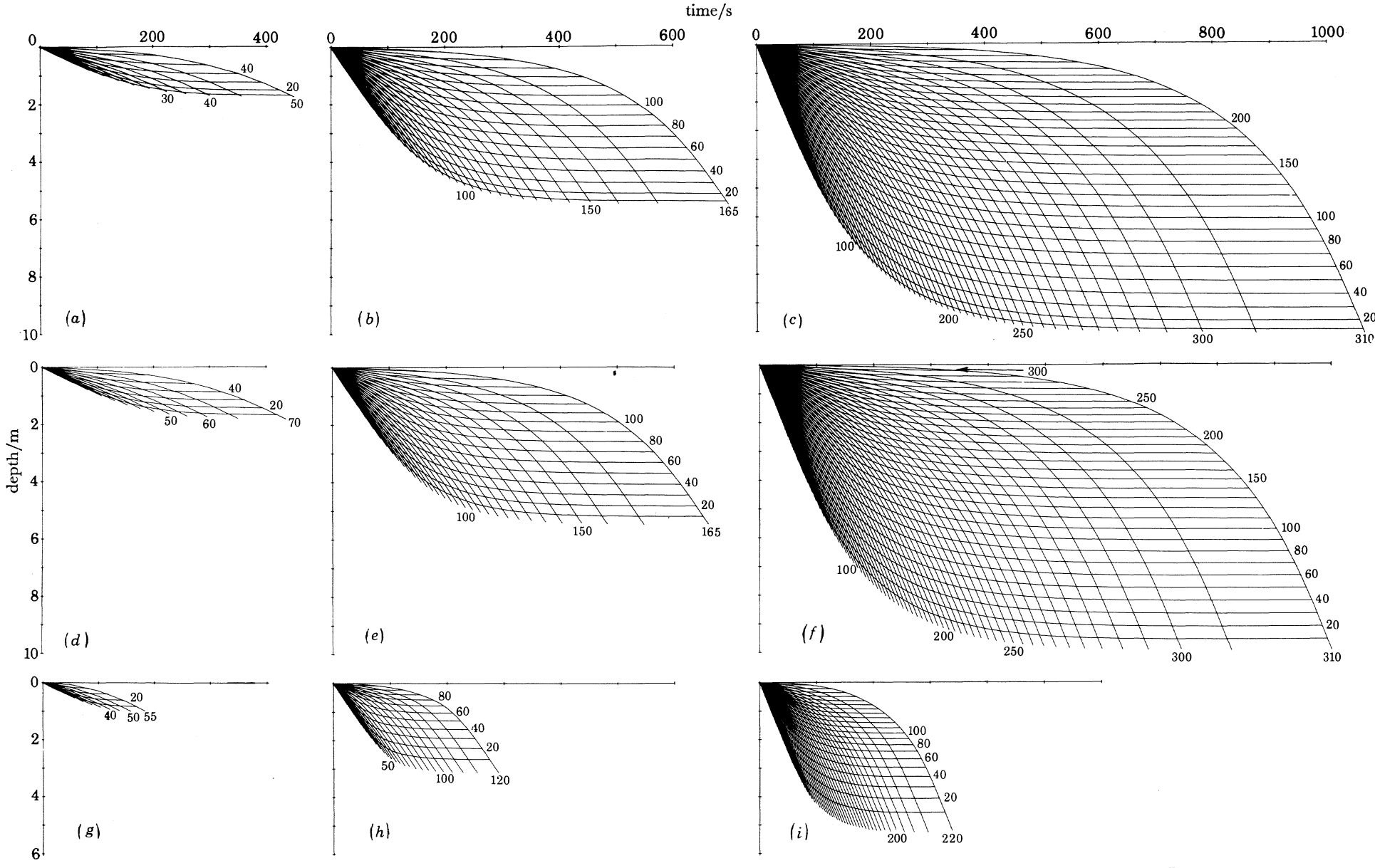

FIGURE 18. For description see opposite.

sizes up to the largest that can be carried down by the given velocity are shown, for initial radii that are integer multiples of 10 μm. The radius of the bubbles below the surface is shown by a second set of superimposed curves. The largest bubbles penetrate farthest and have the longest lifetimes. The effect of the changed dependence of Nusselt number on Péclet number for bubbles of radii less than 28.1 μm is indicated by the increased rate of reduction of size for small bubbles; the nearly horizontal lines of constant radius become closer together when $a < 30$ μm. The curve may slightly overestimate the lifetime and depth of penetration of large bubbles because of the underestimation of Nu (see figure 17) and w_b (at least at $a > 180$ μm).

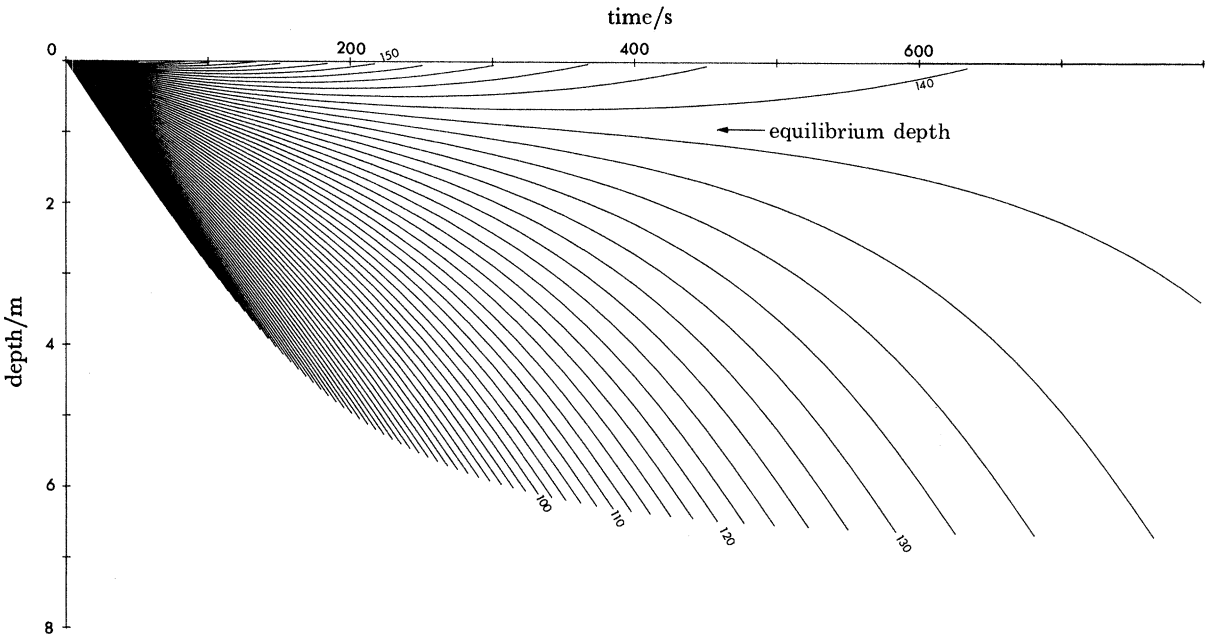

FIGURE 19. Curves showing the variation of depth with time of individual dirty bubbles of nitrogen as they are carried from the surface in 10 % supersaturated water by a uniform downward flow of 3 cm s^{-1}. The original bubble radii are at 2 μm increments.

Figure 18*d–f* is a similar figure for dirty bubbles composed of a mixture of oxygen and nitrogen with $x_0 = 0.215$, appropriate to air, but for simplicity the variation of Nusselt number given by (17) has been assumed to be valid for all a. The curves are very close to those of figure 18*a–c*, except for small radii where the diffusion rate is underestimated by (17); the presence of oxygen in the bubble has thus only a small effect, and for practical purposes we may simplify the calculations by considering bubbles entirely filled with nitrogen. The more rapid diffusion of oxygen leads to a reduction of x with time; typically the bubbles contain 15 % oxygen (i.e. $x = 0.15$) at radii

FIGURE 18. Curves showing the variation of depth and radius of bubbles with time as individual bubbles are carried from the surface in saturated water by uniform downward flows: (*a*), (*d*), (*g*), $w = 1$ cm s^{-1}, (*b*), (*e*), (*h*) $w = 3$ cm s^{-1}; (*c*), (*f*), (*i*), $w = 5$ cm s^{-1}. Each curve that is concave downwards is the depth–time locus of a bubble, the original radius of which is given by the label at the lowest point in the trajectory (or which can be inferred from neighbouring values; original radii are at 5 μm intervals). The curves that are concave upwards join bubbles of equal radius at 10 μm intervals, and show the level or time in the first set of curves at which the bubble radius has been reduced to the given value. (*a*)–(*c*) 'Dirty' bubbles composed of nitrogen only; (*d*)–(*f*) 'dirty' bubbles composed of nitrogen and oxygen in the ratio 26:7 at the surface; (*g*)–(*i*) 'clean' bubbles composed of nitrogen and oxygen in the ratio 26:7 at the surface.

$a = 25\,\mu m$ (see also table 3). For comparison with figure 18*d–f*, figure 18*g–i* shows the curves for clean bubbles composed of a similar oxygen and nitrogen mixture with Nu given by (16). Because of the more rapid diffusion (figure 17) and smaller descent rate (figure 16) the bubbles are not carried down as far before they vanish.

Figure 19 shows dirty nitrogen bubbles in 10 % supersaturated water with vertical velocity $w = 3\,cm\,s^{-1}$ sufficiently large that, for some bubbles that sink, d (given by (25)) is positive. From figure 16 the equilibrium radius is about 167 μm and from (25) the equilibrium depth is 0.96 m, as indicated in figure 19.

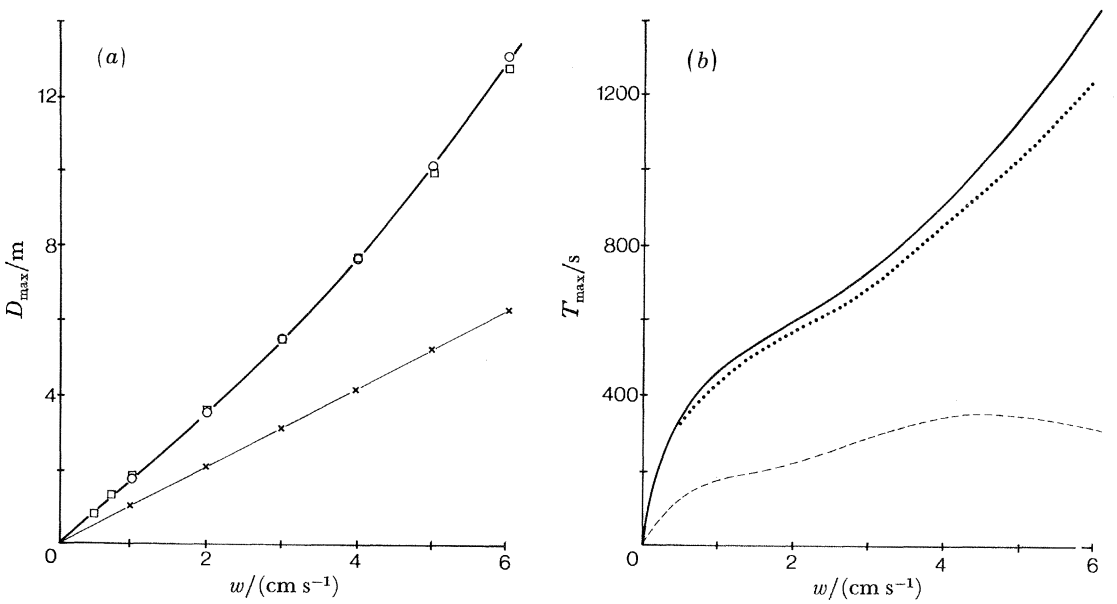

FIGURE 20. The maximum depths D_{max} and duration T_{max} of bubbles against vertical current w. (*a*) D_{max} against w: ×, clean bubbles composed of oxygen and nitrogen; □, dirty bubbles composed of oxygen and nitrogen; ○, dirty bubbles of nitrogen only. (*b*) T_{max} against w: ——, dirty nitrogen bubbles; ·····, dirty bubbles of oxygen and nitrogen; – – – –, clean bubbles composed of oxygen and nitrogen.

TABLE 3. THE VARIATION OF THE MINIMUM VALUE OF x (x_{min}) AND MAXIMUM PENETRATION DEPTH (D_{max}) FOR BUBBLES COMPOSED OF AN AIR MIXTURE OF OXYGEN AND NITROGEN ($x = 0.215$ AT ATMOSPHERIC PRESSURE) FOR VARIOUS VALUES OF THE SATURATION LEVELS p_{10}, p_{20} IN THE WATER WHEN THE BUBBLES ARE CARRIED BY A VERTICAL CURRENT OF 3 cm s^{-1}

(In the absence of oxygen, nitrogen bubbles would be carried to 6.8 m in 10 % oversaturated water.)

p_{10}	p_{20}	oversaturation of O_2 (%)	oversaturation of N_2 (%)	x_{min}	D_{max}/m
0.224	0.816	4	4	0.160	6.00
0.219	0.801	2	2	0.150	5.72
0.211	0.769	−2	−2	0.155	5.25
0.206	0.754	−4	−4	0.152	5.03
0.215	0.864	0	10	0.147	6.30
0.215	0.785	0	0	0.154	5.50
0.237	0.785	10	0	0.139†	5.72

† The value of x increases at small depths before decreasing in this case.

Graphs showing the maximum depth (D_{max}) to which bubbles are carried and the maximum lifetime of bubbles (T_{max}) in different vertical currents at 100 % saturation are shown in figures 20*a* and *b*. The effect of saturation levels on D_{max} and on the minimum value of x (x_{min}) in the bubbles is shown in table 3. Neither D_{max} nor x_{max} are very sensitive to changes in saturation levels of ± 10 %. The value of T_{max} is, however, sensitive to variation in positive saturation levels because of the possibility of bubbles coming into equilibrium (see figure 19), although in view of their expected instability, this effect is probably not very significant.

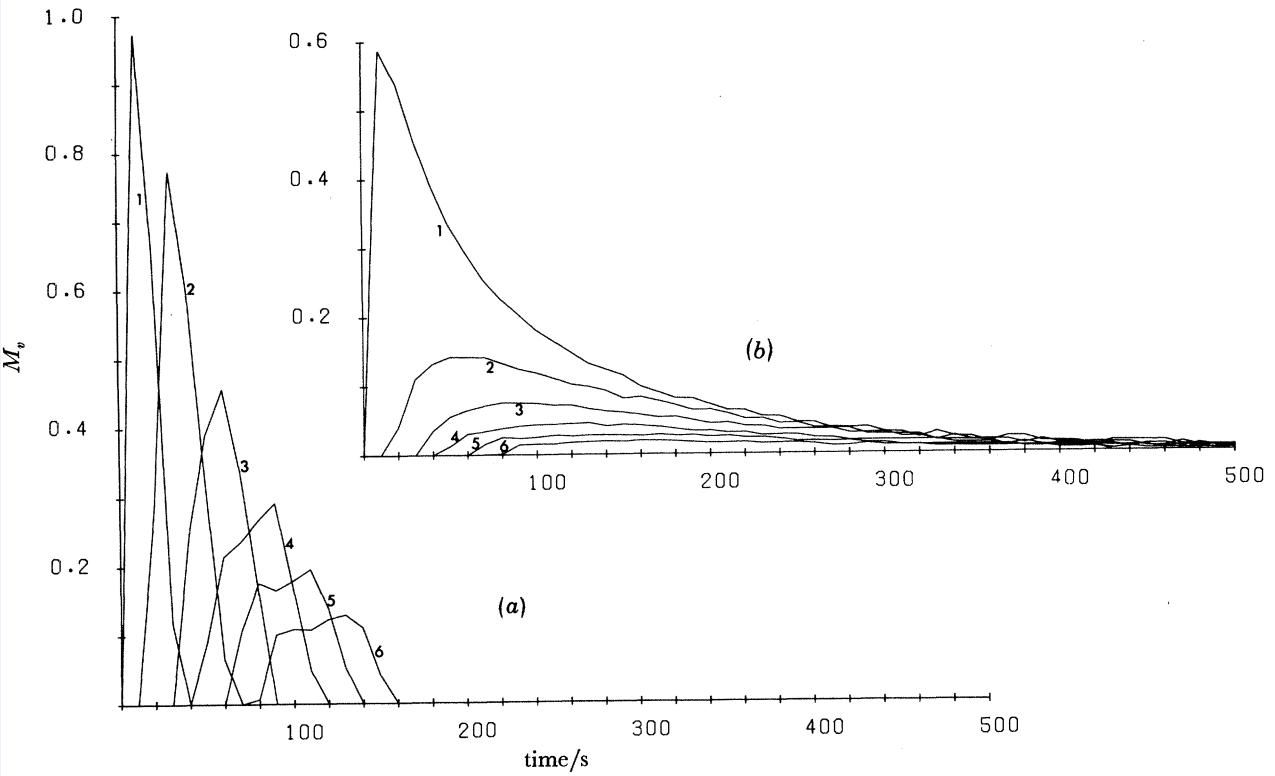

FIGURE 21. The variation in (normalized) M_v after the creation of a uniform cloud of bubbles at the surface when the downward current is 3 cm s^{-1}. Values of M_v are shown at 0.45, 0.90, 1.35, 1.80, 2.25, 2.7 m below the surface, marked 1 to 6. In (*a*) the bubbles are equally numerous for sizes up to 100 μm; none has greater size. In (*b*) the cloud extends to sizes of 200 μm.

The maximum depth to which dirty bubbles are carried (figure 20*a*) is given approximately by

$$D_{max} = 1.9w, \tag{29}$$

for $D_{max} \leqslant 8$ m, with a maximum error of less than 10 %. This equation may be interpreted as an estimate of the *least* vertical uniform current in which bubbles must have been advected from the surface if they are found at depth D_{max}. It also provides a lower bound on the downward vertical components of the turbulent currents relative to, and near, the water surface. For example the bubble clouds shown in figure 11*c* extend to 8 m and must have been carried downwards by a current of, at least, 4.2 cm s^{-1}. Some interpolation is needed to find the minimum vertical advection speeds necessary to carry bubbles to the 20 m depths reported by Kanwisher; we estimate 7.5 cm s^{-1} for dirty bubbles (19 cm s^{-1} for clean bubbles).

Figures 20*a* and *b* can be combined to find an empirical relation between maximum depth and lifetime, $T_{\max}$ (min):

$$T^2_{\max} = 25 D_{\max}, \tag{30}$$

for $D_{\max} < 6$ m. (For greater values of $D_{\max}$ the lifetime exceeds the prediction of this equation.) The clouds shown in figures 5–7, and 11–13 have much shorter durations than predicted by (30), and this suggests that they are being advected past the sonar rather than developing to their largest extent within the sonar beam.

3.5. *Variation of scattering cross section after bubble formation*

Figure 21 shows the variation in M_v (for the 248 kHz sonar frequency) at six equally spaced levels (1–6) between 0.45 and 2.7 m after the formation of bubbles at the surface at time $t = 0$. As an example it is here assumed that the vertical velocity is 3 cm s^{-1}, the bubbles are dirty and composed of nitrogen and, at the surface, the number of bubbles per unit volume per unit radius, $N(a)$, is constant for $a \leqslant a_c$ (100 or 200 μm) and zero for $a > a_c$. The value of M_v has been normalized by taking the initial value at the surface as unity. Values of M_v have been calculated by using (26) and (27) to follow the bubbles' changing size and path, and (2) and (5) to estimate M_v, with δ taken from Devin (1959).

The curves in figure 21 thus represent the scattering produced by bubbles created by a single breaking wave in a region of sustained downward current. The observed features that most closely correspond to this condition are perhaps at the front shown in figure 7*a* or in the squall shown in figure 6*a*. There is a qualitative similarity in these, and some of the other, observed cases but the effects of horizontal advection make close comparison impossible.

4. Theory: bubble cloud dispersion and diffusion

4.1. *Bubbles and turbulence*

The water near the sea or loch surface is turbulent, and although large-scale regular structures can sometimes be recognized in the density or velocity field, which may locally produce areas of relatively uniform vertical currents like those considered in §3 (see Thorpe & Hall 1980, 1981), the flows are generally unsteady and variable. The bubble generation processes, the breaking waves, are also random and, especially in light winds, sometimes infrequent. In Loch Ness the frequency of breaking wind waves has been studied by Thorpe & Humphries (1980). Although scattered, the data show that the frequency increases with wind speed roughly as 2.2×10^{-3} $(W_{10} - 2.5)$ (Hz) where W_{10} is the wind speed (m s^{-1}). From (6) and (30), as well as the sonagraphs, the average lifetime of bubbles is thus greater than the mean period between waves if the wind speed exceeds about 6.5 m s^{-1}. For lower wind speeds the bubble clouds will be isolated, while for much greater wind speeds the clouds will overlap, tending to form a continuous layer of bubbles. There is an analogy with diffusion in plumes from extended or isolated sources in the atmospheric boundary layer. For low winds, or those of short fetch, similar results may be expected at Oban, but figure 11 cautions that swell may have an important effect on the intermittency of clouds in open water.

When a wave breaks, it creates not only bubbles but also turbulence and vorticity and, in considering bubbles as indicators of diffusion from the surface, it is important to establish whether they are so biased towards these regions of enhanced turbulence as to be unrepresentative of the

general levels of turbulence below the water surface. There is as yet insufficient information about the generation of turbulence by breaking waves to be certain (see Peregrine & Svendson 1978), but it seems unlikely that the effect of the initial turbulent enhancement in the spilling wave can remain significant throughout much of the lifetime of the bubbles that it generates, a time much greater than the wave periods. (We have considered two simple models. The first likens the turbulence produced by a breaking wave to that of a turbulent spot in a wind tunnel (see for example Cantwell *et al.* 1978) and concludes that the growth rate of the turbulent region would be much less than the inferred diffusion speeds of small bubbles. The second supposes that the wave in breaking generates a double anti-rotating vortex (see Batchelor 1967) which traps and carries bubbles after the fashion described by Tooky *et al.* 1977. It proved very unlikely that the spilling breakers or white horses seen in deep water in windy conditions could provide sufficient vertical impulse to produce vortices capable of carrying bubbles to the observed depths.)

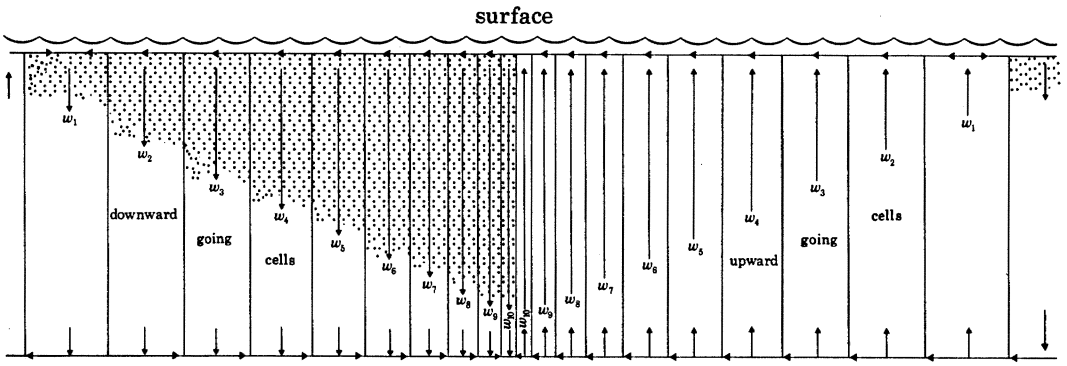

FIGURE 22. The cell model. The cells are supposed to extend with similar proportions over the horizontal plane. Recirculation is in a narrow region at the surface and at some (unspecified) level below the bubble clouds.

4.2. *A simple cell model for bubble diffusion*

We inferred in §3.4 that the depth to which bubbles are carried increases with the vertical velocity (figure 20*a*). Because the mean depth of bubble clouds is observed to increase with wind speed (see equations (1), (6) and (7)), there is a relation between the wind speed and the average velocity at which bubbles are carried from the surface. The velocity must be at least sufficient to carry bubbles to the depth at which they are observed for a given wind speed, before they dissolve completely into solution. We here suppose that the vertical velocity near the surface is distributed in a Gaussian way and that the average downward velocity of the components is w_*. Suppose also that the water near the surface is divided into cells of up-going and down-going water, continuity being achieved by recirculation at depth and in a narrow region at the surface (figure 22). In each cell the speed of the water is uniform. For numerical convenience we take ten 'downward going' cells with speeds $w_n = [0.25(n-1)+0.125]\,\sigma_w$ $(n = 1, \ldots, 10)$, where σ_w is the standard deviation of the vertical velocity, and a similar set of 'up-going' cells. (No bubbles will be carried downwards in the latter.) We suppose that the areas of the cells are proportional to

$$A_n = 0.25(2\pi)^{-\frac{1}{2}} \exp\{-\tfrac{1}{2}[0.25(n-1)+0.125]^2\}; \quad n = 1, \ldots, 10, \tag{31}$$

so that approximately $\sum_{1}^{10} A_n = 0.5,$

and the vertical velocities have a Gaussian distribution of probability. (The horizontal plane may be regarded as being completely covered by repeating sets of such cells.)

The mean downward speed is then obtained as

$$w_* = \sum_1^{10} w_n A_n = 0.383\sigma_w \tag{32}$$

by substituting the expressions for w_n and A_n.

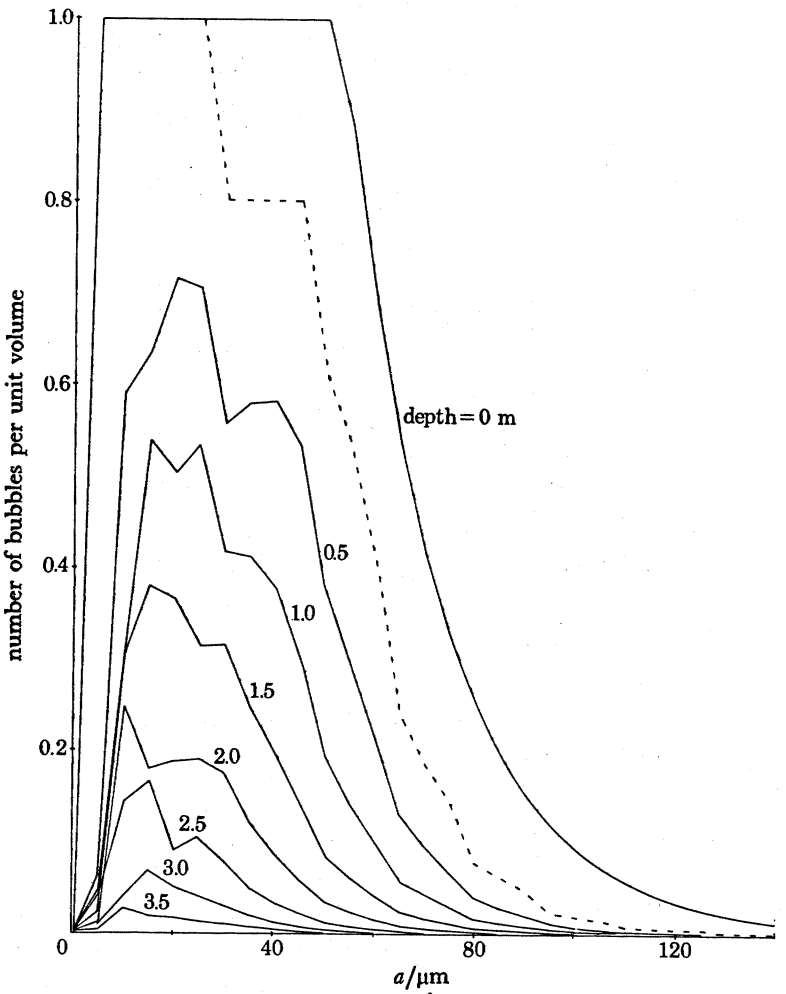

FIGURE 23. The distribution of bubble sizes in the cell model for wind speed of 6 m s^{-1} at different depths below the surface. Only the fraction, denoted by the dashed line, of the bubbles available at the surface (0 m) is carried down by the currents in the cells.

Writing (29) as $D_{\max} = qw$, we may calculate the average depth to which bubble clouds in the cells descend:

$$\bar{d} = \sum_1^{10} qw_n A_n = qw_*. \tag{33}$$

Hence using the relation $\bar{d} = 0.40\,(W_{10} - 2.5)$, where $\bar{d}$ is the mean cloud depth (m) and W_{10} the wind speed (m s^{-1}), found by Thorpe & Stubbs (1979) (which corresponds also to the data

for southwesterly winds at Oban†, equation (7)), we can find σ_w (in cm s^{-1}):

$$\sigma_w = 2.61 w_* = (2.61/q)\bar{d} \approx 0.55\,(W_{10} - 2.5), \tag{34}$$

and hence the speed in the cells.

We now use the numerical model of §§ 3.4 and 3.5 to estimate the variation of $\bar{M}_v$ with depth, given a suitable, and horizontally uniform, distribution of bubbles $N_0(a)$ at some level. The variation of $\bar{M}_v$ is not found to be very sensitive to the distribution selected. The results are illustrated by taking parameter values for dirty bubbles composed entirely of nitrogen (it makes little difference if oxygen is also present; see figure 18) so that $x = 0$, with

$$N(a) = \begin{cases} N_0, & a \leqslant 50\,\mu\text{m}, \\ N_0 \exp[-0.05(a-50)], & a > 50\,\mu\text{m}, \end{cases} \tag{35}$$

at $z = 0.5$ m.

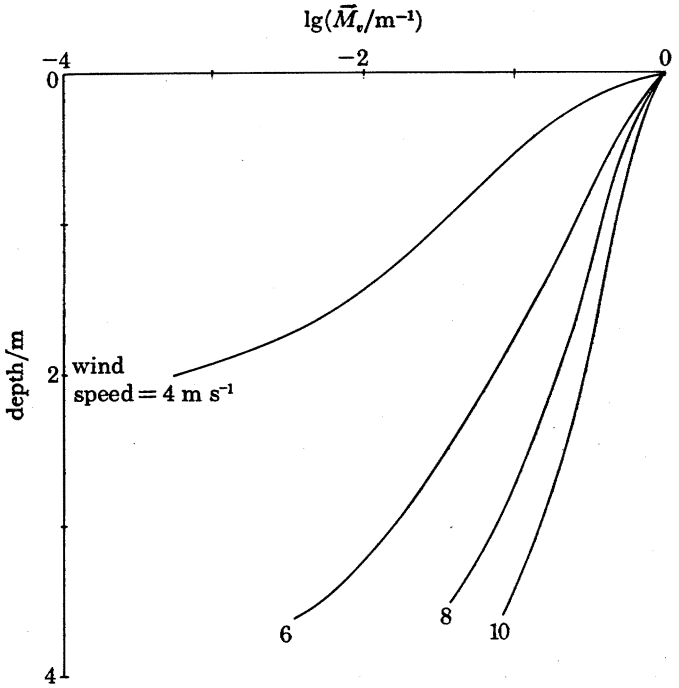

FIGURE 24. Logarithm of normalized M_v against depth at different wind speeds according to the cell model.

The calculations were made with a 1 μm radius interval. In calculating the bubble density at any depth it was necessary to take into account the increasing separation between bubbles, and consequent reduction in population density, as they accelerate.

Figure 23 shows an example of the variation in bubble size distribution with depth, and figure 24 shows how $\bar{M}_v(z)$ varies with increasing wind speed. We have normalized $\bar{M}_v$ using the value at the surface. The histogram of bubble size shows that the number of very small bubbles

† If the coefficient is taken to be 0.31 to correspond to the mean depth at which the signal reaches the noise level in Loch Ness in neutral conditions (equation (6)), the wind speeds corresponding to the curves of figure 24 should be 4.4, 7.0, 9.6 and 12.2 m s^{-1} respectively.

decreases rapidly (a consequence of the rapid diffusion from small bubbles: $da/dt \sim a^{-1}$ as $a \to 0$; see (23) and (19)) leaving a peak value of the bubble population near 15 μm radius at 3 m depth. In the numerical experiments there is a double peak in the histograms. This is artificial, a consequence of the selection of discrete cells and the fact that each cell carries downwards only a portion of the bubbles available at the surface. Thus only part of the population labelled zero in figure 23 is carried downwards. (This fraction is indicated by the dashed line.) This factor also explains the large change in $\overline{M}_v$ between zero and 0.5 m seen in figure 24. The curves steepen as the wind increases, in accordance with the observations, but are generally steeper than the observed curves at the same wind speed, suggesting that more bubbles are being carried down in the model than might be in practice. It is interesting to note the existence in both model and observations of large values of $\overline{M}_v$ well beyond the average depth to which bubbles penetrate.

Several assumptions are implicit in this model. It is supposed that the cells are 'steady' so that the bubbles will be carried downwards steadily until they dissolve. For this to be valid the turbulent eddies in the near-surface waters would have to have lifetimes large compared with those of the bubbles. While there is evidence that some 'eddies' may indeed have this property (in particular the Langmuir vortices leading to the appearance of wind rows have a lifetime that generally exceeds 5 min), it is not true in general (see Thorpe & Hall 1977, 1980). Moreover the source of bubbles (the breaking waves) is not continuous so that, if the cells existed and were themselves steady, the bubble populations would not be steady and the cells would not on average be filled by bubbles to the depths predicted. The model suffers from the need to impose an empirical relation between the wind speed and mean cloud depth. Other empirical relations could be used to derive (34). For example, it might be assumed that the wind stress, τ, on the water surface is continuous, so that $\tau = \rho_a C_d W_{10}^2$ is equal to ρu_*^2, where u_* is a friction velocity in the water (in cm s^{-1}), and ρ_a is the air density. Then

$$u_*/W_{10} = (\rho_a C_0/\rho)^{\frac{1}{2}} \approx 0.13, \tag{36}$$

if the drag coefficient, $C_d = 1.3 \times 10^{-3}$. In a turbulent boundary layer, however, $\tau/\rho\sigma_w^2 \approx 0.52$ (Heathershaw 1979), so that $\sigma_w \approx 0.18 W_{10}$. It would be possible to refine the model to account (in some quasi-empirical way) for the time-dependent nature of the cells and the bubble source. However, in view of the other assumptions inherent in the model (for example, the unrealistic cell circulation; that might also be improved), it seems at best useful to provide a qualitative interpretation of the observations.

4.3. *A turbulent diffusion model*

4.3.1. *Analytical solutions*

The extensive work on the diffusion of a passive contaminant in the atmospheric boundary layer is not directly applicable to bubbles because of their tendency to rise and to dissolve. The similarity between bubble clouds and clouds of droplets in cumulus or fog, offers a closer analogy which might be exploited by regarding the condensation onto droplets in the clouds as the reverse of the transfer of gases into solution across the bubble surface. Other analogous cases are the maintenance in suspension of particles of sediment by turbulence against their tendency to fall out of suspension, the antithesis of bubble rise, or perhaps the decay of a short-half-life radioactive tracer on such particles supported by turbulence, thus modelling the gas loss.

Garrettson (1973) has discussed the equation governing the size distribution $N(a, z, t)$ of a cloud of bubbles at depth z. If accelerations can be ignored† this equation may be written

$$\frac{\partial}{\partial t}(N+n)+\nabla\cdot[\boldsymbol{u}(N+n)]+\frac{\partial}{\partial a}\left\{(N+n)\left[\frac{\mathrm{d}a}{\mathrm{d}t}+\left(\frac{\mathrm{d}a}{\mathrm{d}t}\right)'\right]\right\}=0,$$

where $n(a, x, y, z, t)$ is the difference between the instantaneous bubble size distribution at x, y, z at time t and the horizontal mean $N(a, z, t)$, $\boldsymbol{u}=(u, v, w-w_{\mathrm{b}})$ is the speed of bubbles of size a at x, y, z in a flow u, v, w with w_{b} the bubble rise speed, $\mathrm{d}a/\mathrm{d}t$ is the mean rate of decay of bubbles of size a and $(\mathrm{d}a/\mathrm{d}t)'$ is the deviation of this decay rate from the mean. Taking averages over time, and assuming horizontal isotropy and a steady mean state, we find

$$\frac{\partial}{\partial a}\left[N\frac{\mathrm{d}a}{\mathrm{d}t}+\overline{n\left(\frac{\mathrm{d}a}{\mathrm{d}t}\right)'}\right]-w_{\mathrm{b}}\frac{\partial N}{\partial z}+\frac{\partial}{\partial z}(\overline{wn})=0, \tag{37}$$

where

$$\mathrm{d}a/\mathrm{d}t=-(3p+4\gamma/a)^{-1}[3RTD_2\kappa_2N_2(p+2\gamma/a-p_{20})-aw_{\mathrm{b}}] \tag{38}$$

(and we have supposed that bubbles are composed of a single gas, nitrogen, so that $x=0$, using the notation of §3.2) and

$$(\mathrm{d}a/\mathrm{d}t)'=-ag\rho w/(3p+4\gamma/a), \tag{39}$$

using (8) and (23), and supposing that $\bar{u}=\bar{v}=\bar{w}=0$.

The three terms in (37) arise from fluxes in a, z-space. They are respectively due to

(i) variation in bubble size (see (23); the divergence $\partial/\partial a$ represents bubbles accumulating at size a),

(ii) the vertical rise of bubbles of size a at level z, and

(iii) the vertical divergence of the vertical turbulent flux of bubbles of size a.

Let us now suppose that the cloud is composed of small bubbles of almost equal size, a_0. The first term in (37) will then correspond to the rate of loss of bubbles from the cloud at level z through absorption of gas and may be represented by a term $\sigma_*(a_0, z)N$, where σ_* is the rate of decay of bubbles of size a_0. If we assume that the total number of bubbles decreases at the same rate as the radius decreases, then $\sigma_*\sim(1/a_0)\,\mathrm{d}a/\mathrm{d}t$ evaluated at $a=a_0$ and at level z for $w_{\mathrm{b}}=0$. We have here abandoned the possibility of describing the size distribution of bubbles and N will henceforth in this section represent the total number of bubbles per unit volume at level z. The second term in (37) remains unchanged except that it can now be written $-w_{\mathrm{b}}(a_0)\,\mathrm{d}N/\mathrm{d}z$. We shall write the third term in terms of the vertical gradient and a diffusion coefficient K,

$$\overline{wn}=-K\,\mathrm{d}N/\mathrm{d}z, \tag{40}$$

and thus obtain

$$\sigma_*N-w_{\mathrm{b}}\frac{\mathrm{d}N}{\mathrm{d}z}+\frac{\mathrm{d}}{\mathrm{d}z}\left(K\frac{\mathrm{d}N}{\mathrm{d}z}\right)=0. \tag{41}$$

Equation (41) represents a balance between the downward turbulent diffusion of bubbles from the surface, the vertical rise of bubbles towards the surface, and the decay of bubbles at a rate σ_*. For $\sigma_*=0$, the equation has been used to predict the vertical distribution of heavy particles above an erodable bed, and for fine sediment satisfactory agreement with observations can be found when K is taken to be approximately equal to the diffusion coefficient appropriate to turbulent momentum transfer near a rigid wall (see for example Raudkivi 1976; Yalin 1977).

† The neglect of acceleration terms leads to the omission of the 'car jam' effect, a reduction in N occurring in regions where the bubble speed, u, increases, because the flux Nu is conserved. This effect was included in the cell model (§4.2) and found to be small but not insignificant.

PHILOSOPHICAL TRANSACTIONS OF THE ROYAL SOCIETY A MATHEMATICAL, PHYSICAL & ENGINEERING SCIENCES

CO_2 intoxication, severe 'bends', or thermal danger. The interaction between high pressure and anaesthesia has aroused considerable interest, and pressure reversal has been proposed as a test of 'true' anaesthesia. Diver selection has hardly been explored. It is clear that there is considerable individual human variation in the response to oxygen, in liability to decompression sickness, and in the effects of pressure; Professor Naquet's suggestion that, just as astronauts are selected, divers should be too, offers considerable potential when the principles of selection can be established.

TABLE 1. SURVEY OF PROGRESS

problem	*solution offered*	*practical success*	*scientific understanding*
optimal respiratory pressure	apparatus design	reasonable to around 350 m s.w.	partial
'burst lung' in submarine escape	screening training equipment design	reasonable	partial
respiratory gas density at raised pressures	helium	reasonable to 300–400 m s.w.	good
CO_2 accumulation	equipment for removal	good	good (except for mechanism of narcosis)
oxygen poisoning	avoidance of excess O_2 tension	reasonable, but gross practical constraint	poor
decompression sickness	avoidance by slow decompression	reasonable, by empirical adjustment, but gross practical constraint	inadequate on nucleation, gas movement, and pathogenesis of lesions
inert gas narcosis	helium	good	partial (as with anaesthesia in general)
high pressure nervous syndrome	palliated by (*a*) adaptation (*b*) drugs or gases	partial	poor
hypothermia or hyperthermia	heating control systems	reasonable	good
communications	'unscramblers'	partial	partial

Even if the future course of hyperbaric work is uncertain, it is hard to believe support will not be found when one considers that there are problems of such scientific generality as the biological effects of pressure, anaesthesia, and nucleation, together with the continuing need by navies and by industry for at least a maintenance of a body of expertise, and the existence of a very considerable field of amateur diving. The discussion made it clear that for some of the work needed, the facilities required called for a major national centre; but there was an equal stress on the need for diversification, particularly in university centres, so that the subject could be exposed to cross-fertilization by other sciences.

Discussion

H. V. HEMPLEMAN (*A.M.T.E. Physiological Laboratory, Gosport, U.K.*). One of the criticisms made of human diving trials is that such small numbers are used that it is difficult to draw useful conclusions.

Although the small numbers of subjects undoubtedly prevent firm decisions on some issues,

where $\mathscr{K}_{\frac{1}{2}\lambda}$ is the modified Bessel function chosen so that $N \to 0$ as $z \to \infty$, $\lambda = w_b/ku_*$, $\mu = (\alpha/ku_*)^{\frac{1}{2}}$ and N_0 is a constant. Alternatively, if $w_b = ku_*$, we can solve (41) without imposing the condition $z \ll H$ to give

$$\frac{N}{N_0} = \frac{H}{z}\left(1+\frac{z}{H}\right)^{\frac{1}{2}} \mathscr{K}_1\left[2\mu H\left(1+\frac{z}{H}\right)^{\frac{1}{2}}\right]. \tag{44}$$

Both solutions behave as z^{-1} at $\lambda = 1$ for small z. (A solution may also be found for $z \ll H$ in conditions corresponding to unstable stratification; see (47) with $L < 0$ and $z \ll |L|$. The solution is identical to (44) with $\frac{1}{4}|L|$ replacing H.)

We choose $a_0 = 50\,\mu\text{m}$ to correspond approximately to the peaks of the bubble size distributions observed by Johnson & Cooke, which we note do not vary greatly with wind speed. For dirty bubbles we then find that $\alpha \approx 4 \times 10^{-5}\,\text{s}^{-1}\,\text{cm}^{-1}$, and $w_b \approx 0{\cdot}54\,\text{cm s}^{-1}$.

The solutions are plotted in figure 25. We might estimate the values of u_* corresponding to the observations by assuming that the wind stress on the water surface is transmitted to the water (see (36)); then

$$u_* \approx 0.13 W_{10}.$$

The majority of observations are in $0.67 < u_*/(\text{cm s}^{-1}) < 1.56$ $(5.2 < W_{10}/(\text{m s}^{-1}) < 12)$. The solutions predict a rapid decrease in bubble numbers with depth, the e-folding scale at 1.5 m being 48 cm at $W_{10} = 5.2\,\text{m s}^{-1}$ $(u_* = 0.67\,\text{cm s}^{-1})$ increasing to 70 cm at $W_{10} = 10.4\,\text{m s}^{-1}$ $(u_* = 1.35\,\text{cm s}^{-1})$, which corresponds quite well to the observed variation of $\bar{M}_v$, here proportional to Na_0^2. The depth scales with $(u_*/\alpha)^{\frac{1}{2}}$ and is not strongly sensitive to choice of α or a_0 (see the dotted curve in figure 25).

The assumptions leading to the solutions and choice of parameter values are, however, tenuous (even if plausible).

4.3.2. *Numerical solutions*

Returning again to (37) we notice that

$$\overline{n\left(\frac{\mathrm{d}a}{\mathrm{d}t}\right)'} = -\frac{ag\rho\overline{wn}}{(3p+4\gamma/a)}.$$

Hence

$$\frac{\partial}{\partial a}\left[\overline{n\left(\frac{\mathrm{d}a}{\mathrm{d}t}\right)'}\right] = -g\rho\frac{\partial}{\partial a}\left(\frac{a\overline{wn}}{3p+4\gamma/a}\right) \approx -\frac{g\rho}{3p}\overline{wn},$$

provided that $\overline{wn}$ is a weak function of a, and $\gamma/a \ll \frac{3}{4}p$. This is of order $|\overline{wn}/3H|$ where $H \approx 10\,\text{m}$, and is negligible when compared with $|\partial/\partial z(\overline{wn})|$ if $\overline{wn}$ varies with z over a scale much less than H, as it would do if it has the same vertical structure as the observed $\bar{M}_v$. If also we may write $\overline{wn}$ in the gradient form of (40), (37) reduces to

$$K\frac{\partial^2 N}{\partial z^2} + \left[w_b(a) + \frac{\mathrm{d}K}{\mathrm{d}z}\right]\frac{\partial N}{\partial z} - \frac{\partial}{\partial a}\left(\frac{\mathrm{d}a}{\mathrm{d}t}\right)N = \frac{\mathrm{d}a}{\mathrm{d}t}\frac{\partial N}{\partial a}, \tag{45}$$

where $\mathrm{d}a/\mathrm{d}t$ is given by (38).

This equation has been solved numerically with boundary conditions

$$N = \begin{cases} N_0(a) & \text{at} \quad z = z_0, \quad a < a_{\max}, \\ 0 & \text{at} \quad a = a_{\max}, \\ 0 & \text{at} \quad z = z_{\max}, \quad a < a_{\max}, \end{cases} \tag{46}$$

for some chosen values of z_0, $a_{\max}$, $z_{\max} > z_0$ and a suitable choice of N_0, for $K = ku_*z$. The second boundary condition in (46) is appropriate for subsaturated water, but may not be suitable

in supersaturated conditions, when bubbles may increase in radius beyond that given by the condition at z_0. The singularity at $z = 0$ (where, to preserve the flux $K\partial N/\partial z$, the value $\partial N/\partial z \to \infty$) was avoided by selecting $z_0 = 0.5$ m, $z_{max} = 10$ m. This also avoids discussion of the near-surface breaking-wave zone where the assumed form of K is unlikely to be valid.

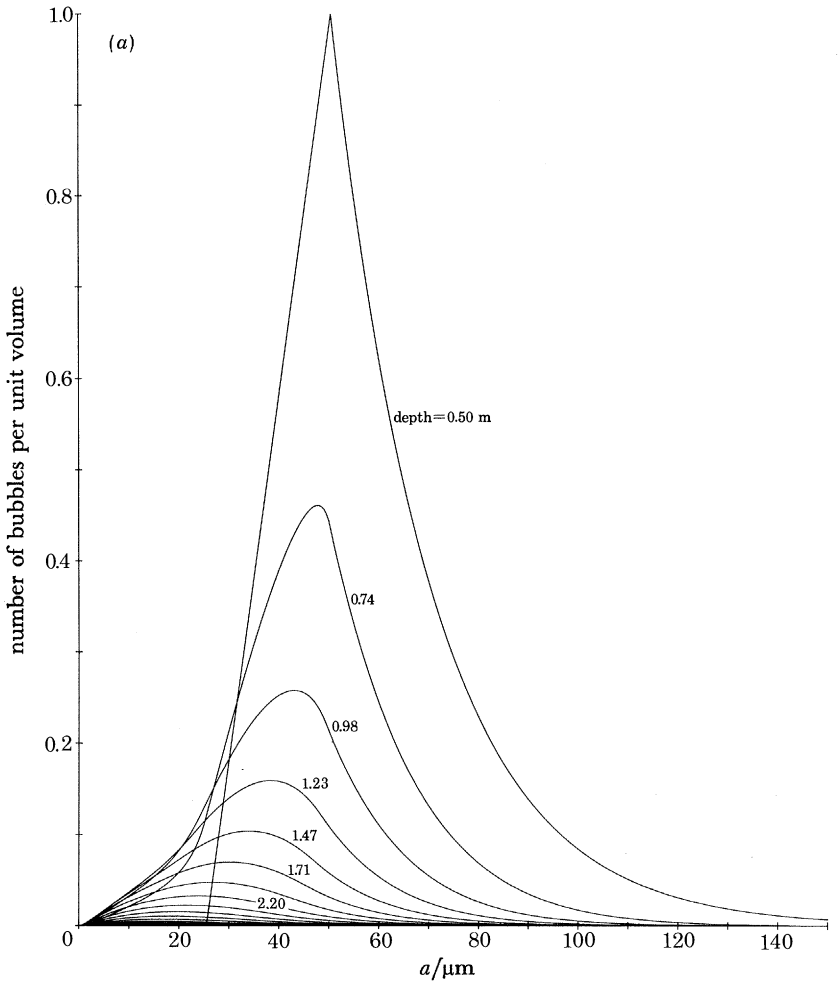

FIGURE 26(*a*). For description see opposite.

Figures 26*a* and *b* show the bubble size distributions, normalized to unity, for the choice of $N_0(a)$ shown by the upper curve and specified in the figure caption, for $u_* = 1.35\,\mathrm{cm\,s^{-1}}$ with the parameter values for dirty bubbles (see §3.2). In the present numerical experiments the Nusselt number, Nu, was taken to be $1 + (2/\pi)\,Pe^{\frac{1}{3}}$ as shown in figure 14, to give correct behaviour as the Péclet number, Pe, tended to zero or infinity. The model used in §3 was not used because of the discontinuous derivatives). The general development of the histogram with depth is similar in the two cases presented, and resembles that seen in figure 23.

The variation of lg $\overline{M}_v$ corresponding to the 248 kHz sonar, for the $N_0(a)$ of figure 26*a*, is shown in figure 27 for various values of u_*. The curves (figure 27*a*) have been normalized at 1 m and are similar to the analytical solutions shown in figure 25. They are almost linear, except at small depths where the bubble size distribution $N(a)$ is affected by the choice of $N_0(a)$. The slope of the

curves increases with u_*, approximately as $u_*^{\frac{2}{3}}$. The exponentiation length (in cm) is approximately equal to $47u_*^{\frac{2}{3}}$ ($0.67 < u_*/(\mathrm{cm\,s^{-1}}) < 2.7$). The two-thirds power law is alone not sufficient to explain the linear increase in bubble cloud depth with wind speed (equations (6) and (7)), or the increase in $\bar{M}_v$ with wind speed (figure 9), and some increase in N_0 is needed to account for these observations.

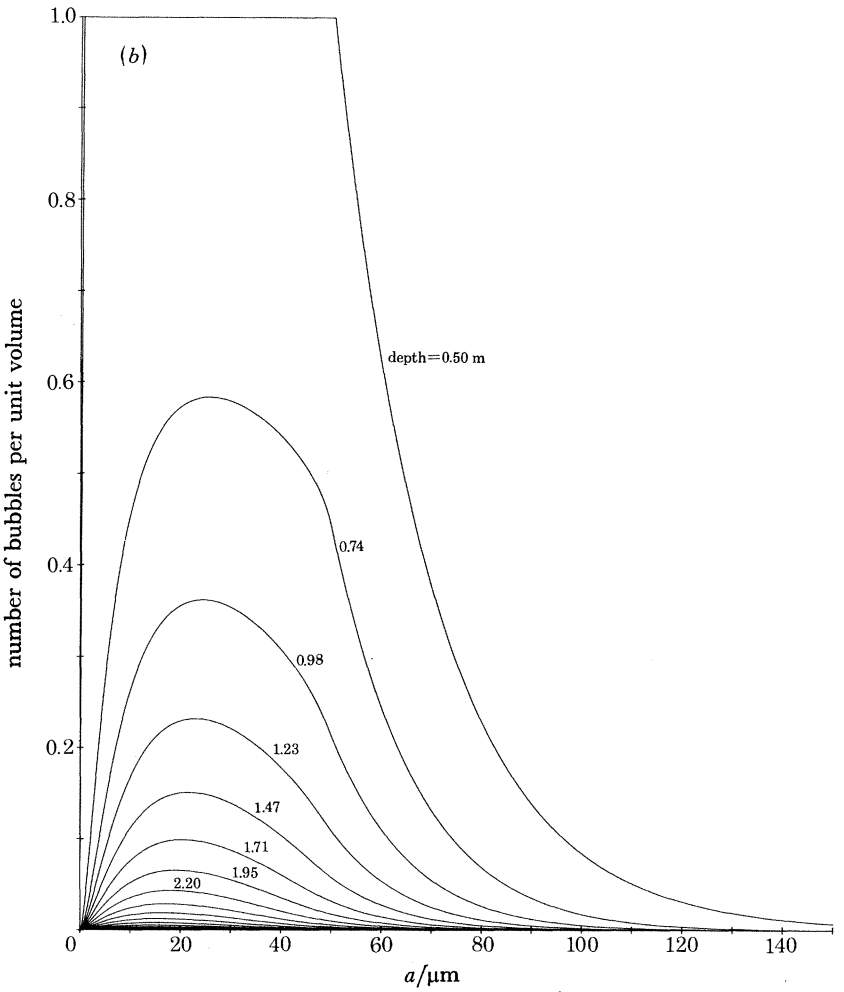

FIGURE 26. The distribution of bubble sizes in the numerical model at different depths below the surface for $u_* = 1.35$ cm s^{-1}:
(*a*) $N(a) = 0$ ($a \leqslant 25\,\mu$m); $N(a) = 0.04(a-25)$ ($25 \leqslant a/\mu\mathrm{m} \leqslant 50$); $N(a) = \exp[0.05\,(50-a)]$ ($50 \leqslant a/\mu\mathrm{m} \leqslant 150$);
(*b*) $N(a) = 1$ ($a \leqslant 50\,\mu$m); $N(a) = \exp[0.05\,(50-a)]$ ($50 \leqslant a/\mu\mathrm{m} \leqslant 150$).

Figure 27*a* also shows the effect of varying the stability of the water column, achieved by choosing

$$K = ku_* z\phi_m^{-1}, \tag{47}$$

with

$$\phi_m = \begin{cases} 1 + 7z/L, & 0 < z/L < 0.2 \quad \text{(stable conditions)}, \\ (1 - 16z/L)^{\frac{1}{4}}, & -1 < z/L < 0 \quad \text{(convectively unstable conditions)}, \end{cases}$$

where L is the Monin–Obukov length scale. Positive (or negative) values of L appear to decrease (or increase) the slopes of the curves and hence, for a fixed value of $\bar{M}_v$ near the surface, decrease

(or increase) the depth to which bubbles might penetrate before the signal reaches the noise level (see figures 10*a*, 15*a*). At $u_* = 1.35\,\mathrm{cm\,s^{-1}}$ the value $|L| = 20\,\mathrm{m}$ produces a variation of about 15 % in the depth to which bubbles will penetrate provided that the value of $\bar{M}_v$ at the surface is held constant, and is not affected by the change in air–water temperature difference. This 15 % change would, from (6), then correspond to the effect of an air–water temperature difference, $\Delta\theta$, of 1.5 K. The value of L is larger than might be expected for this temperature difference in Loch Ness (see Thorpe 1977, p. 168).

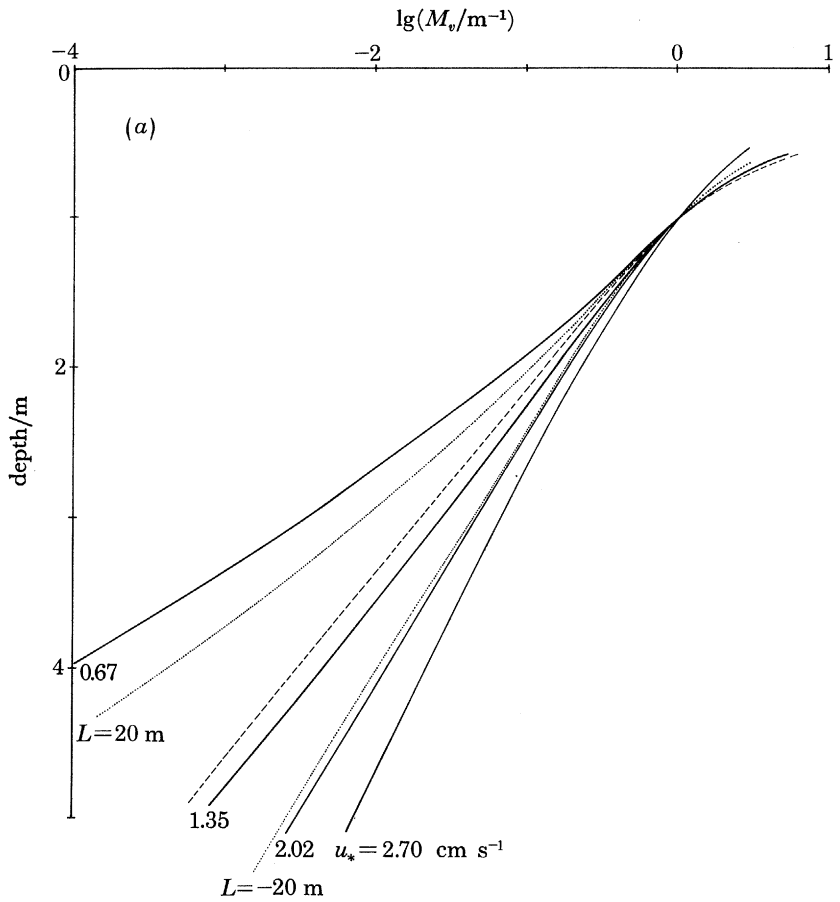

FIGURE 27(*a*). For description see opposite.

Figure 27*b* shows the effect of varying the saturation level of the gas in the water. The variation in the slope of the curves is about 9.6 % for variation in saturation level of 5 %. By selecting a small saturation level variation, and hence a saturation depth $z_s \leqslant 0.5\,\mathrm{m}$, the level at which the upper boundary condition is applied, we have avoided the problem of specifying N at $a = a_{\max}$ when, in supersaturated conditions at $z < z_s$, some bubbles can grow. The effect of increasing the absorption coefficient κ_2 is also shown in figure 27*b*. It is clear from (45) that a set of similar solutions may be obtained if z and K are scaled with κ_2^{-1}. Although diffusion from clean bubbles occurs more rapidly than from dirty† and an increase in κ_2 might be taken to indicate the effect

† For example, for clean bubbles *Nu* which appears in (22) is 6.6 (16.3) at $a = 50$ (100) μm, while for dirty bubbles of the same radius *Nu* has values 3.2 (5.9). The change in κ_2 by a factor of four is, on this count, extreme.

of the bubbles being 'cleaner', the change from dirty to clean bubbles affects w_b (§3.1), and Nu (§3.2) and is not adequately modelled by change in κ_2 alone. Fresh water values of κ_2 are normally greater than those in sea water by about 25 %. The effect of this increase in κ_2 is slightly to reduce the slope of the M_v against depth curve as shown in figure 27.

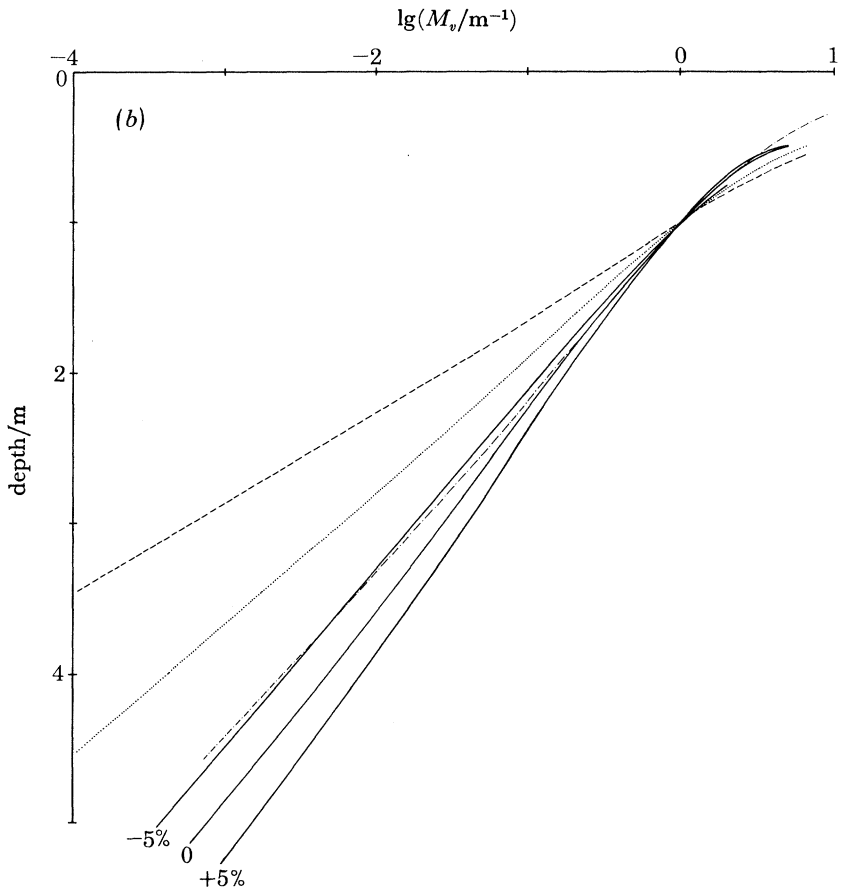

FIGURE 27. Logarithm of (normalized) M_v against depth according to the numerical model for $N(a)$ as given in the caption of figure 26*a*. (*a*) ——, Variation at various values of u_* for neutral stability; · · · · ·, variation at $u_* = 1.35$ cm s^{-1} for $L = \pm 20$ m; – – –, neutral stability curve for $u_* = 1.35$ cm s^{-1} with $N(a)$ given in the caption of figure 26*b*. (*b*) $u_* = 1.35$ cm s^{-1}. ——, Effect of varying the saturation level in the water by ±5 %; – · – · –, · · · · ·, – – –, effect of increasing the solubility κ by factors of 1.25, 2 and 4 respectively.

Figure 28 is a comparison of the observed and calculated depths in which $\bar{M}_v$ decreases by a factor e. The depth scale is determined from the lines drawn in figures 8 and 14 showing the observations and is plotted against wind speed. The points from Oban include one at a wind speed of 14.5 m s^{-1} about which special comment has been made earlier. The theoretical curve, estimated from the slopes of figure 27 at 2 m, is plotted against u_*, (36) being used to relate u_* to W_{10}, and shows fair agreement with the observations. The deviations from this neutral theoretical curve may be explained by variation in either saturation level (see error bars) which is normally greater than 100 %, or in the stability of the water column.

5. Gas flux

The diffusion of gas from individual bubbles was considered in §3.2. Equations (21) and (22) give the rate of change of the number of moles of gas in a bubble. For simplicity we shall again suppose that the bubbles are composed of one gas only, nitrogen, and take (22) with $x = 0$. (For bubbles containing both nitrogen and oxygen it is necessary to retain the factor x and to use (21) with $p_{10} = x_0(p_0 + g\rho z_s)$. The equation may then be approximated by writing $x = x_0$ and ignoring the reduction in x within the bubbles (§3.4 and table 3). This would result in a probable overestimate of the gas flux of some 15 %.) We shall use the saturation depth as defined in §3.4 to characterize the saturation level of the gas in the water.

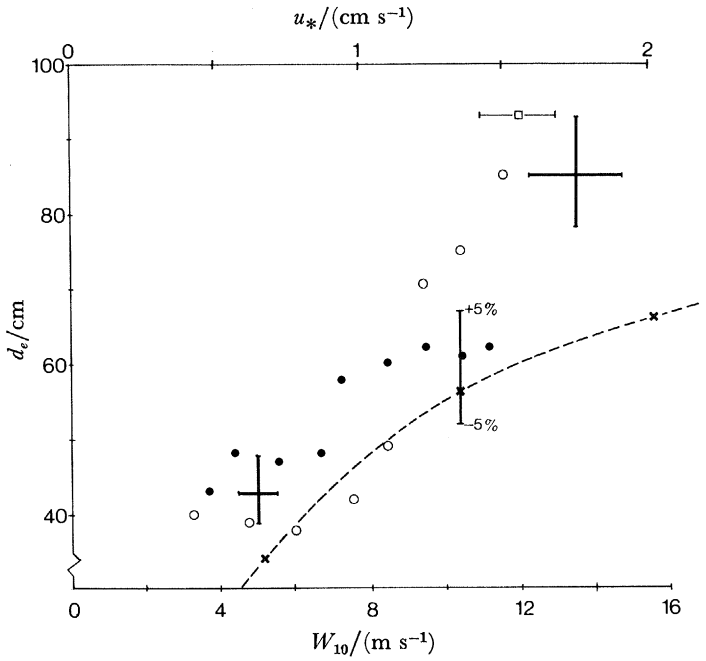

Figure 28. The depth, d_e, over which $\overline{M}_v$ decreases by a factor e against wind speed, W_{10}, or friction velocity, u_* from data for Loch Ness (●) and Oban (○). The square corresponds to Johnson & Cooke's observations and the dashed line to theoretical estimates in 100 % saturation and neutral stability. The vertical bar shows the effect of a 5 % variation in saturation level in the theoretical estimates, while the large crosses are error estimates in the data.

The gas flux (moles per unit time) from a bubble is $-\mathrm{d}n/\mathrm{d}t$, where n is the number of moles of gas in the bubble. Hence, by using (22), the net gas flux from the bubbles per unit volume at depth z is

$$f(z) = 4\pi D\kappa \int aNu\, \bar{N}[g\rho(z - z_s) + 2\gamma/a]\,\mathrm{d}a, \tag{48}$$

where $\bar{N}$ is the mean number of bubbles per unit volume of radius a at depth z, and D, κ, Nu are written for D_2, κ_2, N_2 respectively.

The variation of f with z may be estimated by using the models described in §4. Figure 29 shows $f(z)$ for the numerical model of §4.3.2 for various values of z_s. Most of the gas flux occurs in the upper 2 m of the water where the bubble density is greatest.

We may approximate $f(z)$ by neglecting the terms containing surface tension γ, which are important only for very small bubbles, and by taking the value of the Nusselt number, Nu, appropriate to dirty bubbles at large Péclet number (equation (17), a conservative estimate) with $w_b \approx 2a^2g/9\nu$ (a good approximation for bubbles with $25 < a/\mu\text{m}) < 80$). We then obtain

$$f(z) = 8D\kappa\left(\frac{2g}{9D\nu}\right)^{\frac{1}{3}} g\rho(z-z_s)\int a^2\bar{N}\,\mathrm{d}a. \tag{49}$$

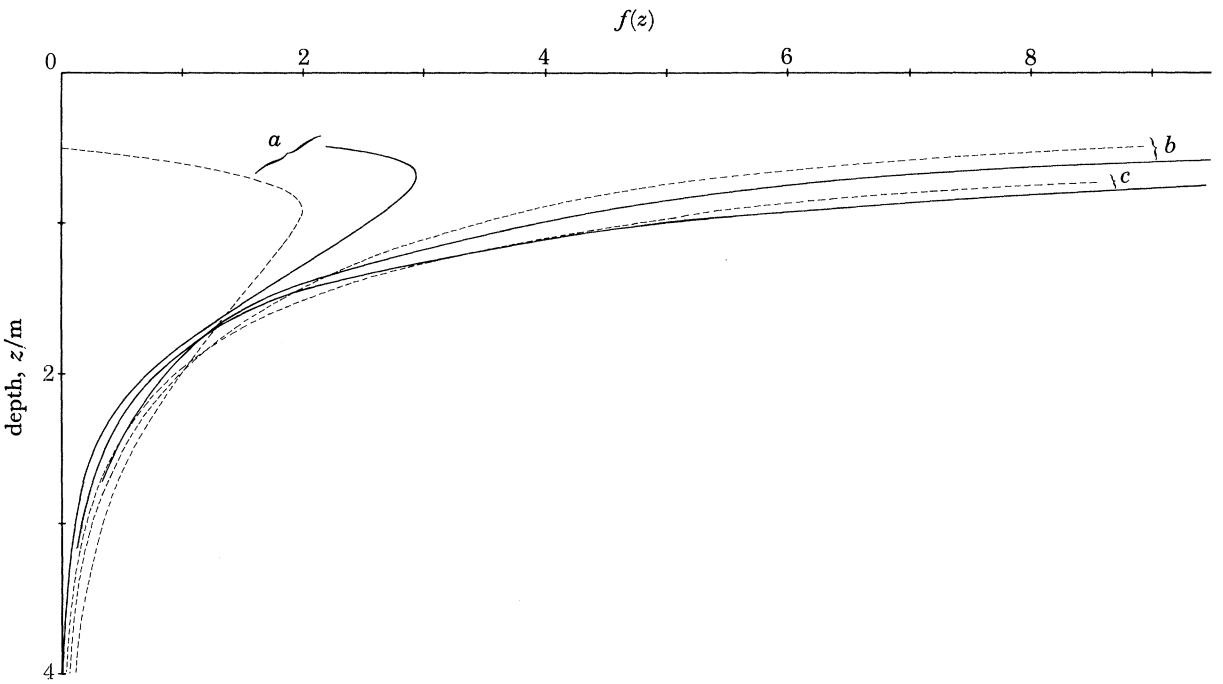

FIGURE 29. The variation of gas flux with depth according to the numerical model of §4.3.2 with $u_* = 1.35$ cm s^{-1} and $N(a)$ as given in the caption of figure 26a. The function $f(z)$ has been calculated by using the same normalization for each curve. ——, Solution according to (48); – – –, approximate solution (50). The pairs of curves correspond to (a) $z_s = 0.5$ m, (b) $z_s = 0$ m, (c) $z_s = -0.5$ m.

(We may estimate the effect of neglecting surface tension as follows. Suppose that

$$\bar{N} = N_0(z)\,a^2\exp(-ba)$$

where b is a constant. This distribution has a peak at $a_{\max} = 2/b$ and is a fairly good approximation to the observed or predicted distributions. Then making the approximations for Nu and w_b we have from (48)

$$f(z) = 8D\kappa\left(\frac{2}{9}\frac{g}{D\nu}\right)^{\frac{1}{3}} g\rho N_0(z)\int a^4\,\mathrm{e}^{-ba}\left(z-z_s+\frac{2\gamma}{ag\rho}\right)\mathrm{d}a$$

$$= \frac{2D\kappa}{\pi}\left(\frac{2}{9}\frac{g}{D\nu}\right)^{\frac{1}{3}} g\rho\,\overline{M_v(z)}\left[z-\left(z_s-\frac{\gamma b}{2g\rho}\right)\right].$$

Since $\bar{M}_v$ is not a strong function of z_s (see figure 27b), comparing this equation with (50) we see that the effect of including surface tension is approximately the same as that of reducing the saturation depth by $\gamma b/2g\rho$ or $\gamma/g\rho a_{\max}$. For dirty bubbles this is about 24 or 8 cm s^{-1}, with $a_{\max}$ equal to 15 μm, a value observed in the numerical models, or 45 μm, observed by Johnson & Cooke, respectively.)

Now

$$4\pi \int a^2 \bar{N}\, da \approx \bar{M}_v,$$

provided that the contribution to $\bar{M}_v$ from bubbles near the resonant radius is not important. Hence we have

$$f \approx f_1(z) = \frac{2D\kappa}{\pi}\left(\frac{2g}{9D\nu}\right)^{\frac{1}{3}} g\rho(z - z_s)\, \bar{M}_v(z). \tag{50}$$

This approximation to $f(z)$ is shown by the dotted curves in figure 29. Near the surface (where the greatest flux occurs) it underestimates the flux, while it overestimates the flux below a few metres depth. For $u_* = 1.35\,\mathrm{cm\,s^{-1}}$ we find that the overall gas flux $\int f(z)\,dz$ is underestimated by 8.1, 11.3 and 20.8 % at $z_s = -0.5$, 0.0, $+0.5$ m respectively (saturation levels -5, 0, and $+5$ %), while for $z_s = 0.0$ m, the flux is underestimated by -10.5 and 19.5 % for $u_* = 0.67$ and $2.7\,\mathrm{cm\,s^{-1}}$ respectively. These errors are fairly small in comparison with those inherent in estimating $\bar{M}_v$ from observations, and with the range of $\bar{M}_v$ observed (see figure 9).

Taking $f_1(z)$ as the gas flux at level z, we may determine the net gas flux by integrating over depth. The observations (figures 8 and 14) are fairly well fitted by

$$\bar{M}_v(z) = 4.5 \times 10^{-5} \exp[(-z/z_1) + (W_{10} - 5.7)/W_1], \tag{51}$$

where z_1 appears to increase with wind speed from about 45 cm at $6\,\mathrm{m\,s^{-1}}$ to 75 cm at $12\,\mathrm{m\,s^{-1}}$, and $W_1 = 3.2\,\mathrm{m\,s^{-1}}$ in fresh water and $1.3\,\mathrm{m\,s^{-1}}$ in the sea. (It should be noticed that these observations are average values without regard to variation of stability or saturation level in the water column.)

Hence the net gas flux from the bubbles is

$$F_b = \int f_1\,dz = \frac{9 \times 10^{-5}}{\pi} D\kappa \left(\frac{2}{9}\frac{g}{D\nu}\right)^{\frac{1}{3}} g\rho \exp[(W_{10} - 5.7)/W_1]\, z_1(z_1 - z_s), \tag{52}$$

(with a possible net error of about 70 %, this being most probably an underestimate). This is positive for all $z_s < z_1$. For fixed z_s it grows at least exponentially with wind speed (more if z_1 increases with wind). If $z_s = 0$ more than 80 % of the flux occurs above $z = 3z_1$, while if $z_s = 0.5z_1$, more than 65 % occurs above $z = 3z_1$. For wind speeds up to $12\,\mathrm{m\,s^{-1}}$, and for moderately supersaturated water, or for subsaturated water, the gas flux is thus concentrated near the sea surface. If $z_s > z_1$ the net effect of bubbles is to remove gas from the water.

Is this flux large enough to contribute significantly to the air–sea gas transfer rate? There have been several laboratory experiments made to determine the flux of gas between water and air, notably those by Downing & Truesdale (1955), Kanwisher (1963) and Liss (1973). These were all made in wind tunnels with shallow water tanks and, although the surface was broken, the results probably represent fairly well the direct transfer across the air–water surface alone since the water depths were too small to allow bubbles to be carried to depths at which the pressure becomes important in driving the gas flux. The experiments found gas exchange rates that varied as the square of the wind speed, although Broecker *et al.* (1978) have suggested a linear dependence while Emerson (1975), reviewing laboratory and field data, suggests an exponential dependence in wind speed.

Indirect measurements have been made at sea by using the naturally occurring radio-isotope gas, radon 222. This method provides an estimate of the gas flux from the sea (the radon source) to the air, and includes a positive contribution operating via the bubbles provided that the

saturation length for radon exceeds z_1. Although spray provides an equivalent physical mechanism of water–air transfer, the spray droplets are not exposed to the same pressure differences as are bubbles. Diffusion via spray is likely to be much less effective, and there is thus an asymmetry in the physical processes of transfer operating at the air–sea interface. Peng *et al.* (1979) surveying the radon diffusion results of the Geosecs programme detected no clear relation between wind and the gas flux as measured by the 'piston velocity', given by

$$V = D/\delta_s = F/(C_0 - p\kappa),$$

where D is the molecular diffusivity of the gas in water, δ_s is a length scale proportional to the (fictional) thickness of the film at the water surface across which diffusion takes place, F is the flux of gas from the water to air, C_0 is the concentration in the water just below the film, p is the partial pressure of the gas in the water and κ is the solubility of the gas in water. In our notation $C_0 = \kappa(p_0 + g\rho z_s)$ and $p = p_0 x_0$ (taking x_0, if oxygen is the gas in question). Peng *et al.* found values of δ_s ranging from 14 to 130 μm with a mean value near 34 μm. Their mean wind speed was 7.9 m s^{-1}, although winds ranged up to 16 m s^{-1}. The radon results provide a reference against which to compare our results of gas flux via the bubbles.

We can estimate, from F_b, a length scale equivalent to the film thickness, δ_s, by finding

$$\delta_b = |D(C - p\kappa)/ - F_b| = |D\kappa g\rho z_s/F_b|.$$

Note that the term x_0 has been omitted; the results are valid under the assumptions made in deriving (52) for any gas. The expression δ_b/δ_s is the ratio of the net flux of gas through the surface to that occurring via the bubbles alone. Taking typical values $D = 2 \times 10^{-9}$ m^2 s^{-1} and $\nu = 1.0 \times 10^{-6}$ m^2 s^{-1}, we have

$$\delta_b = 33.9\{\exp[(W_{10} - 5.7)/W_1]z_1|1 - z_1/z_s|\}^{-1},$$

measured in centimetres. Then $\delta_b|1 - z_1/z_s|$ takes the values 6.2 and 0.63 mm in Loch Ness at winds of 6 and 12 m s^{-1} respectively or 5.4 mm and 35 μm in the sea at equal respective wind speeds. Noting that the flux is inversely proportional to film thickness, it thus appears that within the wind range of the observations, the bubble contribution to the gas flux is unlikely to contribute significantly in Loch Ness, values of net flux quoted by Emerson (1975) being used for comparison. However, even if we recognize the errors inherent in the estimates, comparing the results with those of Peng *et al.* the flux appears to make an important contribution at sea for winds of 12 m s^{-1}, at least when the saturation depth z_s is less than $0.5z_1$ (that is when the percentage oversaturation is less than about 4 %) or greater than $2z_1$ (oversaturation exceeds 16 %). The bubble gas flux may, depending on the (currently uncertain) variation of surface flux with wind speed, be the dominant and controlling factor in higher winds.

If the effects of other processes (such as biological removal of gas from the water, or the addition of water of a different gas saturation level and different temperature into the mixing layer by thermocline erosion) are negligible then, after the onset of wind over a subsaturated ocean, the saturation level in the water will be enhanced by a gas flux both through the surface and through the bubbles, until the surface waters become saturated. Further increase (driven by the bubble contribution) will result in a flux out of the water through the surface, which is eventually balanced at some value of supersaturation by a flux into the water via bubbles. For a given wind speed, the level of supersaturation at which this balance will occur, and the time

taken to achieve balance, may easily be calculated if the variation of the surface flux contribution with wind is known, and the yet inadequately determined variation of z_1 with wind is found (or perhaps estimated at proportional to $u_*^{\frac{8}{3}}$ from the model of §4.3.3).

6. Discussion and conclusions

It is apparent from the observations (see for example, figure 9) that at fetches both shorter and longer than those in Loch Ness, the scattering cross sections found at sea are in excess of those found at similar wind speeds in the fresh-water loch. The cause of this difference is unlikely to be associated with the mechanisms of wave generation or those that lead to breaking, although it is possible that some subtle effect of surface tension may be involved. The solubility of gases decreases as salinity increases, but not by an amount sufficient to explain the observed variation (see figure 27*b*). It seems more plausible that an effect reported by Scott (1975) is involved whereby, under identical physical conditions of generation, bubbles formed in salt water appear to be more numerous, having especially a larger number of small bubbles, than those in fresh water. The physical processes leading to this effect are not fully understood, but bubbles appear to coalesce more readily in fresh water (see also Zieminski *et al.* 1976).

The existence of different cloud types (see figures 5*d* and *e* or 12*a* and *b*) in different conditions of air–water heat flux suggests that the bubble clouds may be used to determine and perhaps quantify the processes of turbulence and diffusion near the sea surface where *in situ* observations are very difficult. Some progress in this direction was reported in §4.3.2. Broad agreement is found between the observed and predicted variation of $\bar{M}_v$ with depth, and the effects of surface heating or cooling on this variation, provided that the values taken for u_* in the water are estimated by assuming continuity of stress across the water surface. The increased penetration of bubbles in unstable conditions is, however, accompanied by an increase in values of $\bar{M}_v$ near the surface (this contributes to the scatter of points in figure 9, particularly those at winds of 5–7 m s^{-1} in Loch Ness) and not simply by the change in slope indicated by figures 27*a* or 28. It appears, therefore, that changes in the depth at which $\bar{M}_v$ reaches the noise level reflect processes of increased or decreased bubble generation in unstable or stable conditions, and not only the turbulent processes within the water column. More research is needed into the frequency of wave breaking and the effect of air–water temperature differences on this phenomenon. The relation between $\bar{M}_v$ and W_{10} (equation (51)), is entirely empirical and should be related to the processes of bubble generation, that is to wave breaking. The apparent exponential relation is consistent with Kanwisher's (1963) conclusion that the bubble volume increases more rapidly than the square of the wind speed. In spite of the uncertainty of saturation levels and heat flux, the general agreement between theory and observations with K chosen as in equation (47), lends further substance to the evidence that the upper boundary layer of the ocean is largely similar to the lower boundary layer of the atmosphere and that waves modify the turbulent structure only in a very shallow region near the surface.

It is interesting to note that the observations suggest that there is a wind speed below which no bubbles will be found beneath the surface. This is in part due to the fact that waves seldom break in low wind speeds. It might also be argued that at low wind speeds the vertical components of the turbulent velocities in the water will be less than the bubble rise speeds and hence unable to carry bubbles from the surface and to maintain them below the surface. This argument is used by Bagnold (1966) (quoted by Raudkivi 1976) to determine the threshold of sediment movement.

PHILOSOPHICAL TRANSACTIONS OF THE ROYAL SOCIETY A MATHEMATICAL, PHYSICAL & ENGINEERING SCIENCES

Following Bagnold's argument and his selection of constant of proportionality leads to minimum vertical velocity and a critical minimum surface stress τ given by

$$w_b \approx 1.25 u_* = 1.25(\tau/\rho)^{\frac{1}{2}},$$

where u_* is the friction velocity in the water, w_b the rise speed of the bubbles and ρ the water density. If the stress is less than or equal to the wind stress, $\rho_a C_d W_{10}^2$, where C_d is the drag coefficient, then

$$w_b < 1.56 \times 10^{-3} W_{10}.$$

Now for small dirty bubbles $w_b \approx \frac{2}{9} a^2 g/\nu$ (see § 3.1). Hence we find that the largest bubble that can be carried down in a wind W_{10} is less than $26.7 W_{10}^{\frac{3}{2}}$, where W_{10} is in m s^{-1}. For $W_{10} = 2.5$ m s^{-1} (the lowest wind speed at which bubbles are observed) this is about 42 μm, close to the size most frequently observed under breaking waves by Johnson & Cooke. The relation is intriguing, suggesting that at low wind speeds waves may not produce bubbles very much smaller than this, but is perhaps fortuitous. The difference between the bubble size distributions predicted here (figures 23, 26) and those observed, particularly the shape of the distributions for small bubble radii, deserves further study. There are, however, severe difficulties in accurately sampling and measuring small bubbles.

The most important conclusion of this paper is that relating to the flux of gases between the ocean and the atmosphere (§ 5). We have shown that, even recognizing the approximations involved in the estimates, the flux through the bubbles is significant at winds of 12 m s^{-1}. It would, however, be cavalier at present to make seasonal, ocean-wide or even regional estimates of this effect. More needs to be known of the variation of $\bar{M}_v$ at greater wind speeds, where present trends suggest that bubble gas flux will dominate. It appears, however, imprudent to disregard the effect of bubbles on the global budget of gas flux. A study of $\bar{M}_v$ in the open sea, together with the variation of saturation levels and air–water heat flux, would be very valuable.

Other aspects of this work, the air–water heat flux, the removal of surface-active material from the sea surface by bubbles, the quantity of particles left by dissolving bubbles, and the use of the sonar to locate the sea surface in rough conditions, deserve further consideration.

This paper was begun when the author was a Cecil Green Scholar at IGPP, La Jolla, and I am grateful to Dr Walter Munk, F.R.S., for inviting me there.

The observations would have been impossible without the clever instrumental developments made by Messrs Alan Hall and Ron Stubbs. Their help, and that of Messrs Chris Hughes and Bob Turner in processing and collecting the data, are gratefully acknowledged. The profiles in figure 4 were obtained by Mr D. Gaunt.

I thank the Scottish Marine Biological Association for providing shelter for the recording instruments at Oban, for help in laying the sonar and in monitoring the instruments, and for supplying copies of their meteorological records.

Appendix 1. Effects of finite bin height and surface waves

The six bins from which the scattered sound is received are about 45 cm in height and are at constant depth. The finite height results in a bin-average M_v being different from the mean M_v at the mean bin depth. If M_v falls exponentially with depth ($M_v = M \exp(-qz)$ say) the average

value in the depth range $z-\delta$, $z+\delta$ is

$$\bar{M}_v = \frac{1}{2\delta}\int_{z-\delta}^{z+\delta} M\exp(-qz)\,\mathrm{d}z$$
$$= M\,\mathrm{e}^{-qz}\sinh(q\delta)/q\delta$$

Now $\delta \approx 22.5\,\mathrm{cm}$, $40 < q^{-1}\,\mathrm{cm} < 125$ (from the observations) and hence

$$1.005 < \bar{M}_v/M\exp(-qz) < 1.054$$

and the error in equating $\bar{M}_v$ to the value of M_v at the mean bin depth is negligible.

Surface waves induce vertical motions and advect water through the bins. To first order the displacement of a surface on which the mean scattering cross section per unit volume is $M_v(z_0)$ from its mean level z_0 is

$$z - z_0 = A\exp(-kz_0)\cos\omega t,$$

where ω is the wave frequency, k the wavenumber and A is its amplitude. Approximately,

$$z_0 = z - A\phi,$$

where $$\phi = \exp(-kz_0)\cos\omega t = \exp(-kz)\cos\omega t(1 + Ak\phi + \ldots),$$

or to first order $$\phi = \exp(-kz)\cos\omega t.$$

Hence $$M_v(z,t) = M_v(z_0) = M_v(z - A\exp(-kz)\cos\omega t].$$

Suppose now that $$M_v(z_0) = M\exp(-qz_0).$$

Then $$M_v(z,t) = M\exp\{-q[z - A\exp(-kz)\cos\omega t]\},$$

and the average value

$$\overline{M_v(z,t)} = \frac{\omega}{2\pi}\int_0^{2\pi/\omega} M_v(z,t)\,\mathrm{d}t,$$
$$= \frac{\omega}{2\pi}M\exp(-qz)\int_0^{2\pi/\omega}\exp[-qa\exp(-kz)\cos\omega t]\,\mathrm{d}t,$$
$$= M\exp(-qz)\,I_0[qA\exp(-kz)],$$

where I_0 is the modified Bessel function (Abramowitz & Stegun 1964). The effect of surface waves is contained in the factor $I_0[qA\exp(-kz)]$ which increases the value of M_v observed at a fixed level above that pertaining to the value at a fixed depth relative to the surface. This effect is greatest at $z = 0$ when A and q take their largest values. For Loch Ness the maximum value of I_0 is about 1.4. At Oban the maximum values is about 2.5. Waves can thus contribute to $\bar{M}_v$ but not enough to explain either the large increase with wind speed, or the differences observed between Oban and Loch Ness. Choosing extreme values of q, A and k, we estimate that the waves may contribute, through the I_0-term, to a 50% variation in $\bar{M}_v$ between the surface and 2 m depth for wave parameters appropriate to Oban, but only about 20% over the same depth range in Loch Ness. These are to be compared with observed changes by factors up to 30 over the equivalent depth ranges, and are thus negligible. The effect of the presence of waves will be to reduce the slope of the curves in figures 8 and 14 near the surface, and thus the estimates of the exponentiation scale in figure 28 may, on this account, be slightly low.

Appendix 2. Calibration and sound scattering by bubbles

Consider the sound intensity $I(r)$ at distance r from a source in a medium with absorption coefficient n per unit distance and containing bubbles with extinction cross section per unit volume σ_e which is a function of r.

The flux of energy over the sphere of radius r is

$$4\pi r^2 I(r) = 4\pi(r+\delta r)^2 I(r+\delta r) + 4\pi r^2 n\,\delta r\, I(r) + 4\pi r^2 \delta r(\sigma_e/4\pi)\, I(r),$$

so that if

$$I(r+\delta r) = I(r) + \delta I,$$

we have

$$\frac{\delta I}{I} = -\frac{2}{r}\delta r - n\delta r - \frac{\sigma_e}{4\pi}\delta r.$$

Hence

$$\lg I = -2\lg r - nr - \frac{1}{4\pi}\int \sigma_e \,\mathrm{d}r + \text{constant},$$

or

$$I = \frac{P}{4\pi r^2}\exp\left(-nr - \frac{1}{4\pi}\int_0^r \sigma_e \,\mathrm{d}r\right), \tag{A 1}$$

where the power $4\pi r^2 I \to P$ as $r \to 0$.

Consider now the scattering from a target of scattering cross section σ at range R. The intensity of the incident sound is given by $I(R)$ in (A 1). The intensity of the scattered sound at the target is $\sigma I(R)/4\pi$, and the intensity at the centre of the sphere of radius R (the source of the sound and the receiver are both at the centre) is

$$\frac{\sigma I(R)}{4\pi}\frac{1}{R^2}\exp\left(-nR - \frac{1}{4\pi}\int_0^R \sigma_e \,\mathrm{d}r\right),$$

from (A 1). Hence the intensity of the reflected sound from the target is

$$\frac{\sigma P}{16\pi^2 R^4}\exp\left(-2nR - \frac{1}{2\pi}\int_0^R \sigma_e \,\mathrm{d}r\right).$$

In making this calculation we have assumed that the scattering from one bubble to another and back to the receiver can be neglected.

The voltage produced by the receiver is proportional to the sound pressure, which is proportional to the square root of the intensity.

For a spherical 'calibration' target with no bubbles between the target and receiver, the voltage output is given by

$$v_t = \frac{q}{R^2}\left(\frac{\pi d^2}{4}\right)^{\frac{1}{2}}\exp(-nR), \tag{A 2}$$

where d is the diameter of the spherical target ($\sigma = \pi d^2/4$) and q is a constant for constant source strength, which can be determined from (A 2) by measuring v_t.

For a target composed of bubbles of scattering cross section $\sigma_s(R)$ per unit volume, the voltage output is given by

$$v_b = \frac{q}{R^2}[\sigma_s L A(R)]^{\frac{1}{2}}\exp\left(-nR - \frac{1}{4\pi}\int_0^R \sigma_e \,\mathrm{d}r\right), \tag{A 3}$$

where $L \ll R$ is the thickness of the layer of bubbles and $A(R)$ is its area:

$$A(R) = \pi\theta^2 R^2/4 \tag{A 4}$$

where θ is the effective beam angle. The thickness L is determined by the size of the range bins from which sound is reflected, that is by the time over which v_b is averaged.

From (A 3) and (A 4), given q from (A 2) and with an assumed value† for n, we can determine

$$\sigma_s(R)\exp\left(-\frac{1}{2\pi}\int_0^R \sigma_e\,\mathrm{d}r\right) = M_v(R), \quad \text{say.} \tag{A 5}$$

Now
$$\sigma_e(r) = \int \sigma'_e(a)\,N(a,r)\,\mathrm{d}a,$$

where σ'_e is the extinction cross section of a bubble of radius a and $N(a,r)$ is the number of bubbles per unit volume of size a to $a+\mathrm{d}a$ at range r. We can write

$$\sigma'_e = \delta c_0 \sigma_b/2\pi\omega_0 a = \delta c_0(\rho/3\gamma' p)^{\frac{1}{2}}\sigma_b(a)$$

(Urick 1975, p. 225) using the notation of §1, where σ_b is the scattering cross section of a bubble of radius a, and c_0 is the speed of sound. For bubbles of radii 10–200 μm, $0.065 < \delta < 0.13$ (Devin 1959). Hence

$$\begin{aligned}\sigma_e(r) &= c_0\left(\frac{\rho}{3\gamma' p}\right)^{\frac{1}{2}}\int \delta(a)\,\sigma_b(a)\,N(a,r)\,\mathrm{d}a\\ &= \delta_1 c_0\left(\frac{\rho}{3\gamma' p}\right)^{\frac{1}{2}}\sigma_s(r),\end{aligned}$$

approximately, for the range of bubble sizes observed, with $\delta_1 \approx 0.1$. Let

$$F(r) = \delta_1 c_0\left(\frac{\rho}{3\gamma' p}\right)^{\frac{1}{2}},$$

then (A 5) becomes
$$\sigma_s(R)\exp\left(-\frac{1}{2\pi}\int_0^R F(r)\,\sigma_s(r)\,\mathrm{d}r\right) = M_v(R). \tag{A 6}$$

Differentiating logarithmically we find

$$\frac{\mathrm{d}\sigma_s}{\mathrm{d}R} = \left(\frac{1}{M_v}\frac{\mathrm{d}M_v}{\mathrm{d}R} + \frac{F\sigma_s}{2\pi}\right)\sigma_s,$$

which may be integrated to give

$$\sigma_s = M_v\left(1 - \frac{1}{2\pi}\int_{R_0}^R FM_v\,\mathrm{d}R\right)^{-1}, \tag{A 7}$$

where $\sigma_s = M_v$ at $R = R_0$ (for example at the base of the bubble cloud). Now

$$\eta \equiv \frac{1}{2\pi}\int_{R_0}^R FM_v\,\mathrm{d}R < \frac{1}{2\pi}\delta_{\max} c_0\left(\frac{\rho}{3\gamma' p_0}\right)^{\frac{1}{2}}\int_0^{z_0} M_v(z)\,\mathrm{d}z,$$

where p_0 is the atmospheric pressure, $\delta_{\max} \approx 0.13$ is the maximum value of δ, and z_0 is the depth of the bubble cloud. (In transferring from spherical coordinate R to the depth coordinate z we have assumed that the effective beam angle θ is small so that spherical surfaces approximate to plane surfaces at constant depth levels.) Hence, taking typical values for c_0, p_0, we obtain

$$\eta < 1.47\int_0^\infty M_v\,\mathrm{d}z.$$

† We have adopted the equation

$$n = A\frac{S\omega\omega_T}{\omega^2+\omega_T^2} + B\frac{\omega^2}{\omega_T}\ (\mathrm{dB\ km^{-1}}),$$

where $A = 7.48\times10^{-4}$, $B = 1.08\times10^{-3}$, $\omega = 248$ kHz and $\omega_T = 21.9\times10^{6-1.52/T}$, S is the salinity (‰) and T is the temperature (K), adapted from that found by Schulkin & Marsh (1963).

Hence, by (A 7), the quantity M_v, determined from observations, is approximately equal to the scattering cross section per unit volume of the bubble cloud, and the correction due to the attenuation of sound passing through the bubble cloud can be neglected, provided

$$\int_0^\infty M_v \, dz \ll 0.68,$$

which is satisfied by the currently observed values.

References

Abramowitz, M. & Stegun, I. A. 1964 Handbook of mathematical functions. New York: Dover Publications.

Aleksandrov, A. P. & Vaindruk, E. S. 1974 In *The investigation of the variability of hydrophysical fields in the ocean* (ed. R. Ozmidov), pp. 122–128. Moscow: Nauka Publishing Office.

Bagnold, R. A. 1966 An approach to the sediment transport problem from general physics. *Prof. Pap. U.S. geol. Surv.* 422–I.

Batchelor, G. K. 1967 *An introduction to fluid dynamics*. Cambridge University Press.

Batchelor, G. K. 1980 Mass transfer from small particles suspended in turbulent flow. *J. Fluid Mech.* **98**, 609–623.

Blanchard, D. C. & Woodcock, A. H. 1957 Bubble formation and modification in the sea and its meteorological significance. *Tellus* **9**, 145–158.

Broecker, H.-C., Petermann, J. & Siems, W. 1978 The influence of wind on CO_2 – exchange in a wind-wave tunnel, including the effects of monolayers. *J. mar. Res.* **36**, 595–610.

Brtko, W. J. & Kabel, R. L. 1978 Transfer of gases at natural air–water interfaces. *J. phys. Oceanogr.* **8**, 543–556.

Caldwell, D. R., Dillon, T. M., Brubaker, J. M., Newberger, P. A. & Paulson, C. A. 1980 The scaling of vertical temperature gradient spectra. *J. geophys. Res.* **85**, 1917–1924.

Cantwell, B., Coles, D. & Dimotakis, P. 1978 Structure and entrainment in the plane of symmetry of a turbulent spot. *J. Fluid Mech.* **87**, 641–672.

Davis, R. E. & Acrivos, A. 1966 The influence of surfectants on the creeping motion of small bubbles. *Chem. Engng Sci.* **21**, 681–685.

Detwiler, A. 1979 Surface-active contamination on air-bubbles in water. In *Surface contamination: genesis detection and control*, vol. 2 (ed. K. L. Mittal), pp. 993–1007. New York: Plenum Press.

Detwiler, A. & Blanchard, D. C. 1978 Ageing and bursting bubbles in trace-contaminated water. *Chem. Engng Sci.* **33**, 9–13.

Devin, C. 1959 Survey of thermal, radiation and viscous damping of pulsating air bbubles in water. *J. acoust. Soc.* **31**, 1654–1667.

Dillon, T. M. & Caldwell, D. R. 1980 The Batchelor spectrum and dissipation in the upper ocean. *J. geophys. Res.* **85**, 1910–1916.

Dillon, T. M., Richman, J. G., Hansen, C. G. & Pearson, M. D. 1981 Near-surface turbulence measurements in a lake. *Nature, Lond.* **290**, 390–392.

Downing, A. L. & Truesdale, G. A. 1955 Some factors affecting the rate of solution of oxygen in water. *J. appl Chem.* **5**, 570–581.

Emerson, S. 1975 Gas exchange rates in small Canadian Shield Lakes. *Limnol. Oceanogr.* **20**, 754–761.

Garrettson, G. A. 1973 Bubble transport theory with application to the upper ocean. *J. Fluid Mech.* **59**, 187–206.

Harper, J. F. 1972 The motion of bubbles and drops through liquids. *Adv. appl. Mech.* **12**, 59–129.

Heathershaw, A. D. 1979 The turbulent structure of the bottom boundary layer in a tidal current. *Geophys. Jl. R. astr. Soc.* **58**, 395–430.

Johnson, B. D. & Cooke, R. C. 1979 Bubble populations and spectra in coastal waters: a photographic approach. *J. geophys. Res.* **84**, C7, 3761–3766.

Jones, E. P. 1980 Gas exchange. In *Air–sea interactions: instruments and methods* (ed. F. Dobson, L. Hasse & R. Davis). New York: Plenum Press.

Kanwisher, J. 1963 On the exchange of gases between the atmosphere and the sea. *Deep Sea Res.* **10**, 195–207.

Kolovayev, P. A. 1976 Investigation of the concentration and statistical size distribution of wind produced bubbles in the near-surface ocean layer. *Oceanology* **15**, 659–661.

Levich, V. G. 1962 *Physico-chemical hydrodynamics*. New York: Prentice-Hall.

Liss, P. S. 1973 Processes of gas exchange across an air–water interface. *Deep Sea Res.* **10**, 221–238.

Medwin, H. 1970 *In situ* acoustic measurements of bubble populations in coastal ocean water. *J. geophys. Res.* **75** 599–611.

Medwin, H. 1977 *In situ* acoustic measurements of microbubbles at sea. *J. geophys. Res.* **82**, 971–976.

Moore, D. W. 1963 The boundary layer on a spherical gas bubble. *J. Fluid Mech.* **16**, 161–176.

PHILOSOPHICAL TRANSACTIONS OF THE ROYAL SOCIETY A MATHEMATICAL, PHYSICAL & ENGINEERING SCIENCES

Peng, T. H., Broecker, W. S., Mathieu, G. G., Li, Y.-H. & Bainbridge, A. G. 1979 Radar evasion rates in the Atlantic and Pacific Oceans as determined during the Geosecs programme. *J. geophys. Res.* **84**, C5, 2471–2489.

Peregrine, D. H. & Svendson, I. A. 1979 Spilling breakers, bores and hydraulic jumps. *Proc. 16th Coastal Engng Conf., Hamburg* 1978, vol. 1, pp. 540–550. New York: American Society of Civil Engineers.

Raudkivi, A. J. 1976 *Loose boundary hydraulics* (2nd edn). Oxford: Pergamon Press.

Ryskin, G. M. & Fishbein, G. A. 1976 Extrinsic problem of mass exchange for a solid sphere and a drop at high Péclet numbers and $Re \leqslant 100$. *J. engng Phys.* **30**, 49–52.

Saffman, P. G. & Turner, J. S. 1956 On the collision of drops in turbulent clouds. *J. Fluid Mech.* **1**, 16–30.

Schulkin, M. & Marsh, H. W. 1963 Absorption of sound in sea water. *Radio Electron. Engr* **25**, 493–500.

Scott, J. C. 1975 The role of salt in whitecap persistence. *Deep Sea Res.* **22**, 653–657.

Stewart, R. W. & Grant, H. L. 1962 Determination of the rate of dissipation in the upper ocean. *J. geophys. Res.* 3177–3180.

Thorpe, S. A. 1977 Turbulence and mixing in a Scottish Loch. *Phil. Trans. R. Soc.* A **286**, 125–181.

Thorpe, S. A. & Hall, A. J. 1977 Mixing in upper layer of a lake during heating cycle. *Nature, Lond.* **265**, 719–722.

Thorpe, S. A. & Hall, A. 1980 The mixing layer of Loch Ness. *J. Fluid Mech.* **101**, 687–703.

Thorpe, S. A. & Hall, A. J. 1982 Observations of the thermal structure of Langmuir circulation. *J. Fluid Mech.* **114**, 237–250.

Thorpe, S. A. & Humphries, P. N. 1980 Bubbles and breaking waves. *Nature, Lond.* **283**, 463–465.

Thorpe, S. A. & Stubbs, A. R. 1979 Bubbles in a freshwater lake. *Nature, Lond.* **279**, 403–405.

Tooky, P. F., Wick, G. L. & Isaacs, J. D. 1977 The motion of a small sphere in a rotating velocity field; a possible mechanism for suspending particles in turbulence. *J. geophys. Res.* **82**, 2096–2100.

Urick, R. J. 1975 *Principles of underwater sound* (2nd edn). New York: McGraw-Hill.

Wu, J. 1981 Bubble populations and spectra in near-surface ocean: summary and review of field measurements. *J. geophys. Res.* **86**, 457–463.

Wyman, J., Scholander, P. F., Edwards, G. A. & Irving, L. 1952 On the stability of gas bubbles in sea water. *J. mar. Res.* **11**, 47–62.

Yalin, M. S. 1976 *Mechanics of sediment transport* (2nd edn). Oxford: Pergamon Press.

Zieminski, S. A., Hume, R. M. & Durham, R. 1976 Rates of oxygen transfer from air bubbles to aqueous NaCl solutions at various temperatures. *Mar. Chem.* **4**, 333–346.

PHILOSOPHICAL TRANSACTIONS OF THE ROYAL SOCIETY A MATHEMATICAL, PHYSICAL & ENGINEERING SCIENCES

FIGURE 5 (*a*) and (*b*). For description see page 166.

surface

depth/m

contours of $\lg(M_v/\mathrm{m}^{-1})$

(c)

$\lg(M_v/\mathrm{m}^{-1})$

wind speed/(m s^{-1})

time/min

surface

depth/m

contours of $\lg(M_v/\mathrm{m}^{-1})$

(d)

$\lg(M_v/\mathrm{m}^{-1})$

wind speed/(m s^{-1})

time/min

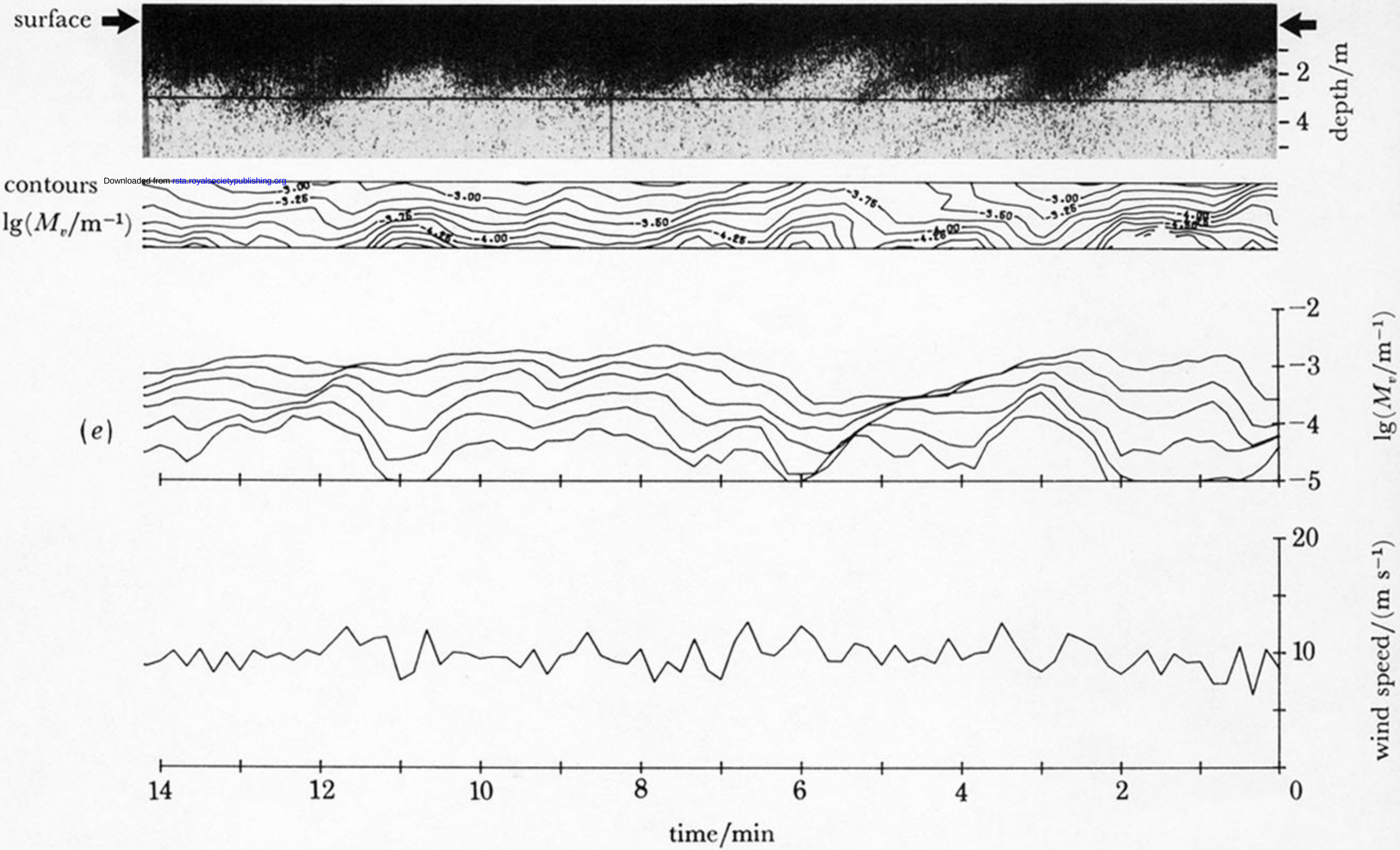

FIGURE 5. Sonagraph records, contours of lg M_v (contour interval 0.25) values of lg M_v, and wind speeds from Loch Ness. Values of air–water temperature differences are (*a*) −0.25 K, (*b*) −0.25 K, (*c*) 1.6 K, (*d*) −3.5 K, (*e*) 4.6 K. There is a difference in the appearance of cloud types in stable and unstable conditions.

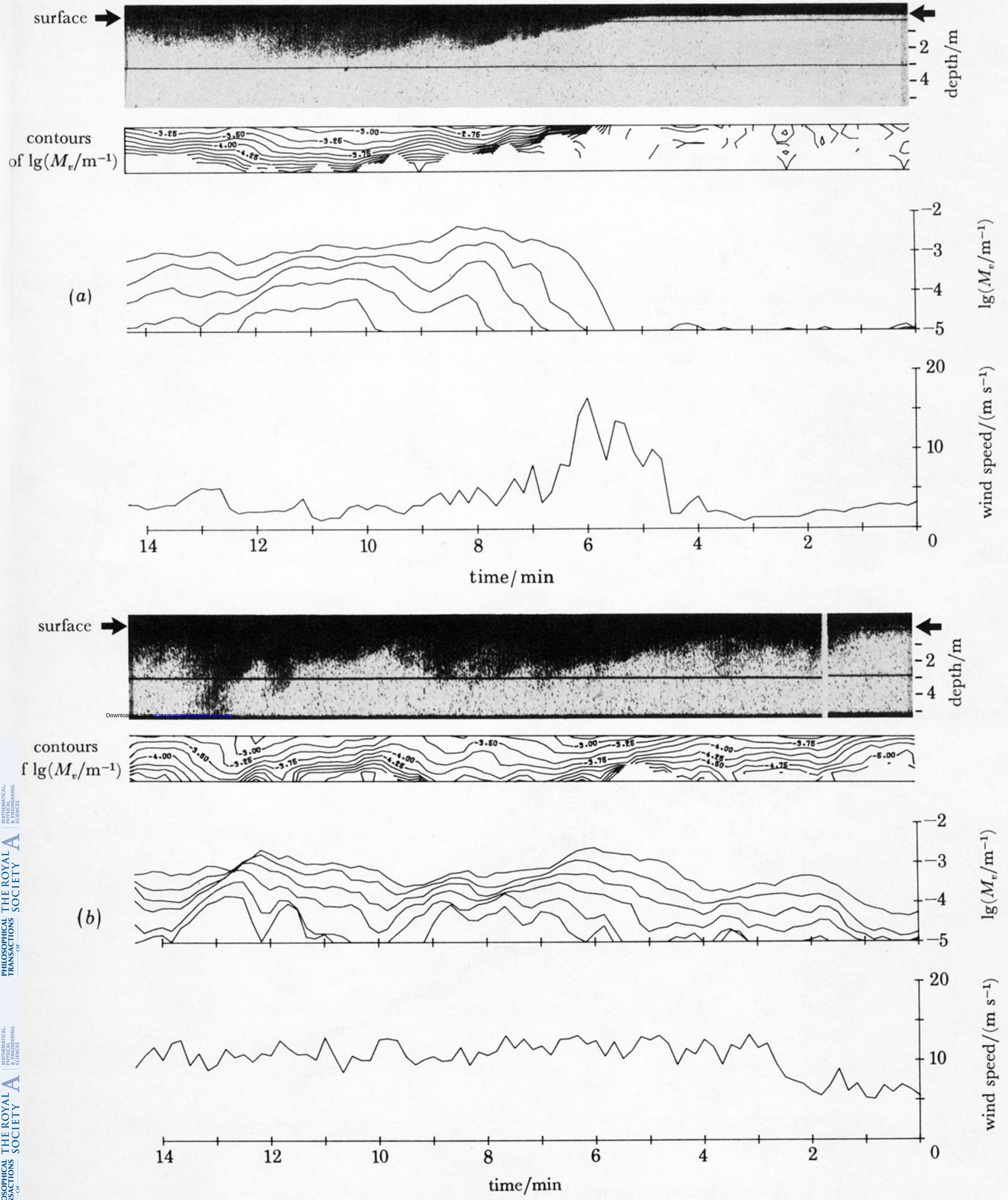

FIGURE 6. Sonagraph, M_v, and wind-speed records from Loch Ness for (*a*) a brief squall and (*b*) an increase in wind speed. The gap early in the sonagraph record is due to a recorder malfunction.

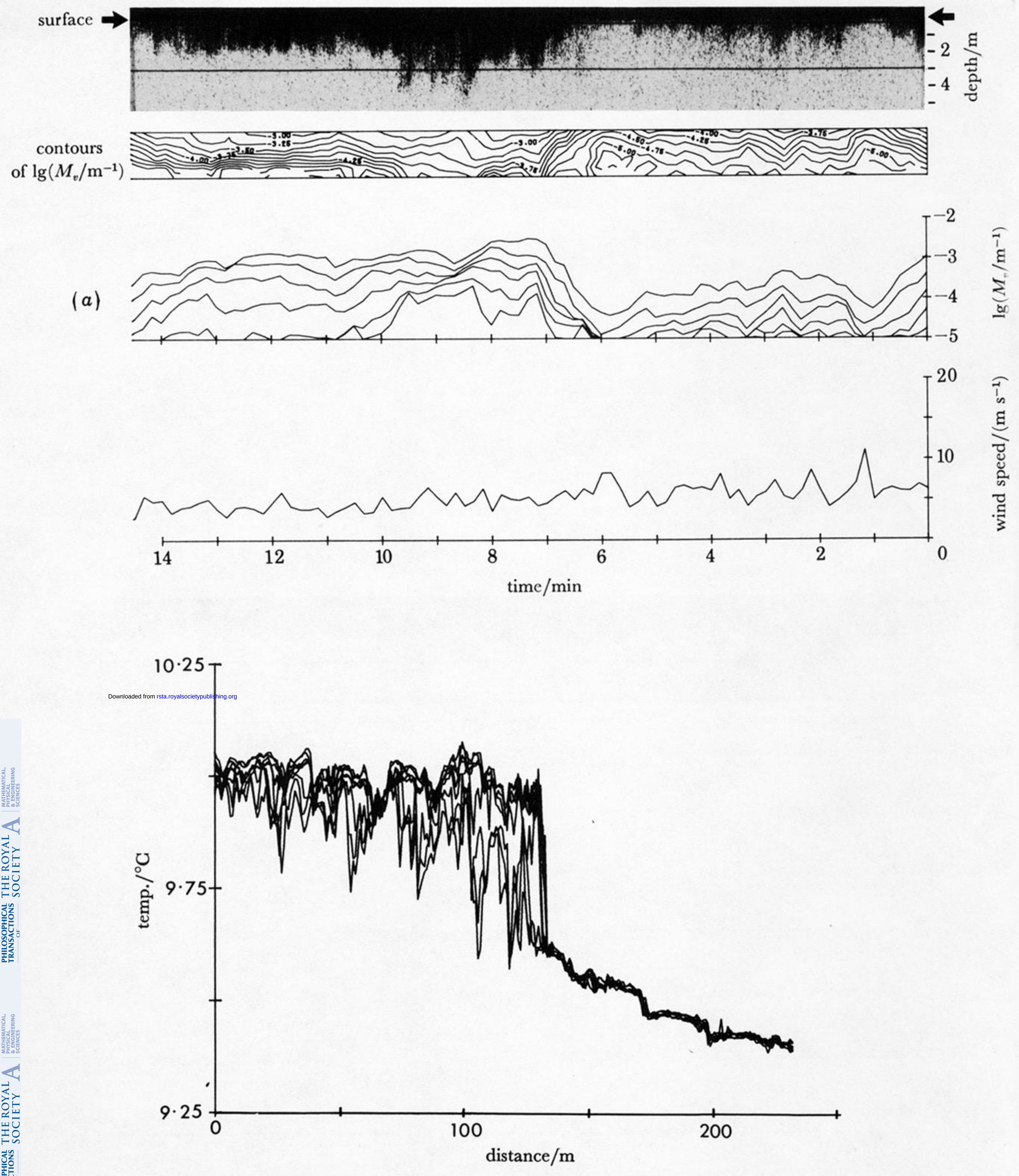

FIGURE 7. (*a*) Sonagraph, M_v, and wind records from Loch Ness during the passing of the temperature front shown in (*b*). (*b*) Eight records from thermistors at between 0.4 and 3.1 m depth in a section northwest–southeast across Loch Ness.

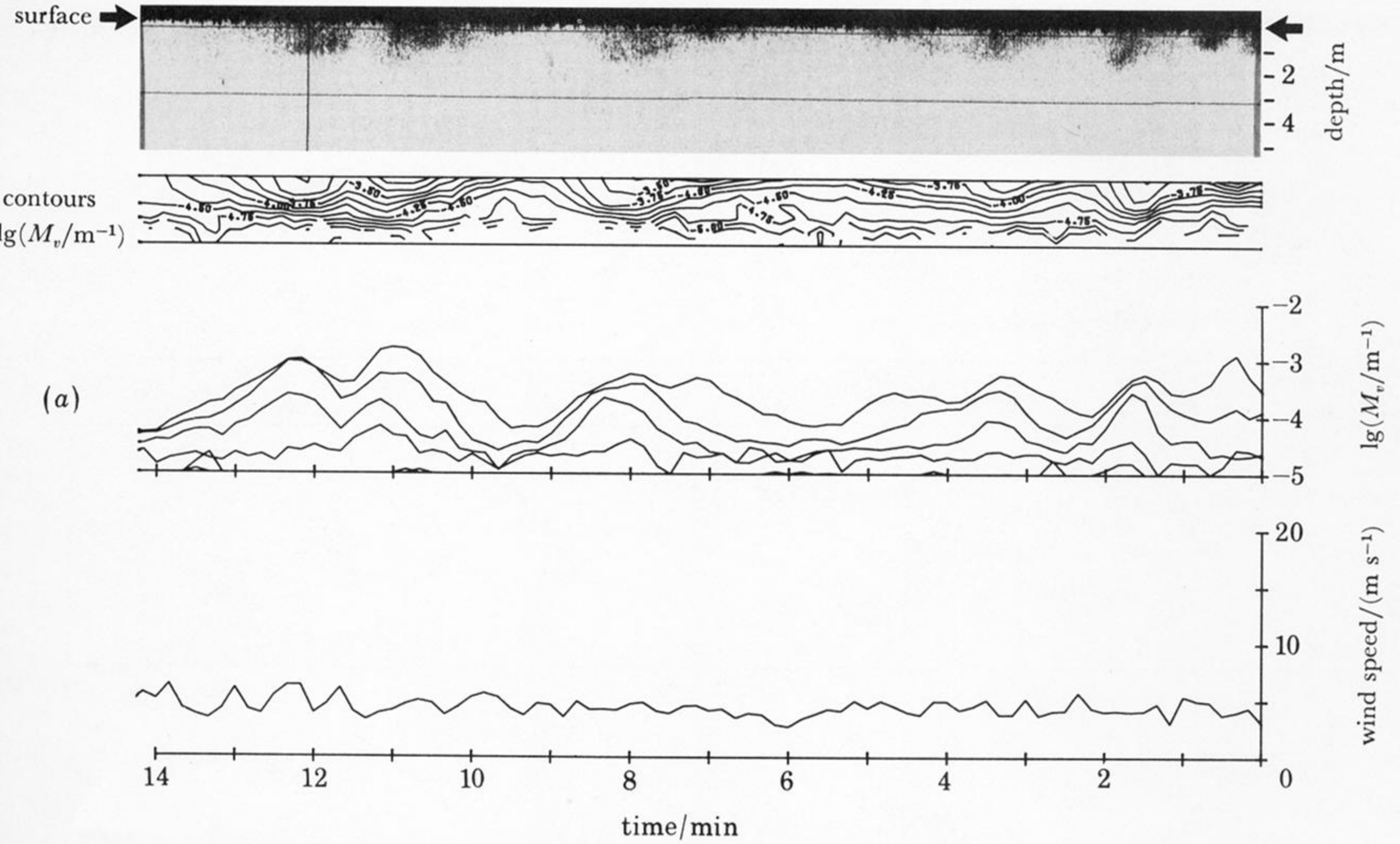

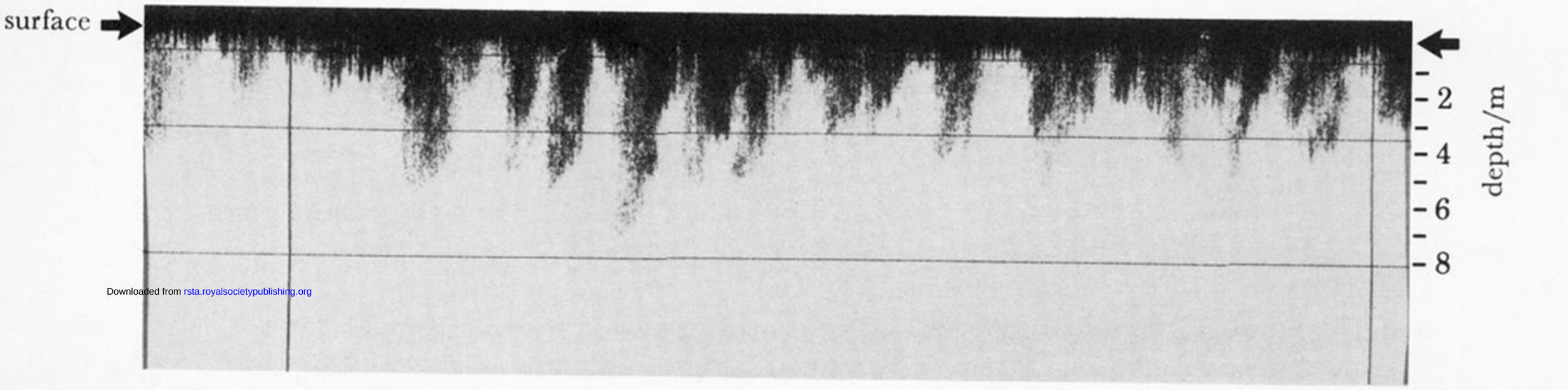

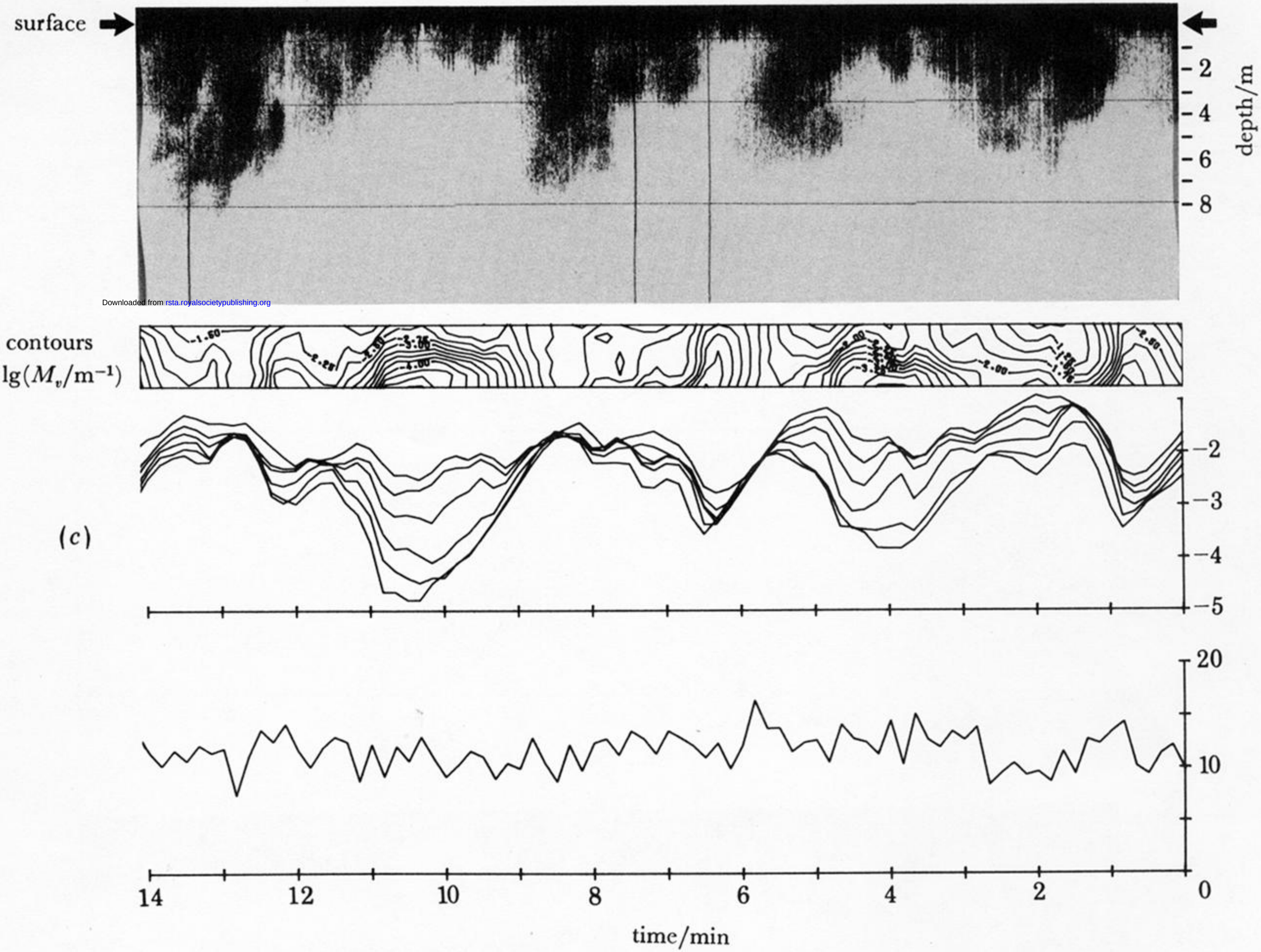

FIGURE 11. Sonagraph, M_v, and wind records from Oban in southwesterly winds: (*a*) $\Delta\theta = -0.4$ K; (*b*) $\Delta\theta = -1.2$ K; (*c*) $\Delta\theta = -1.8$ K.

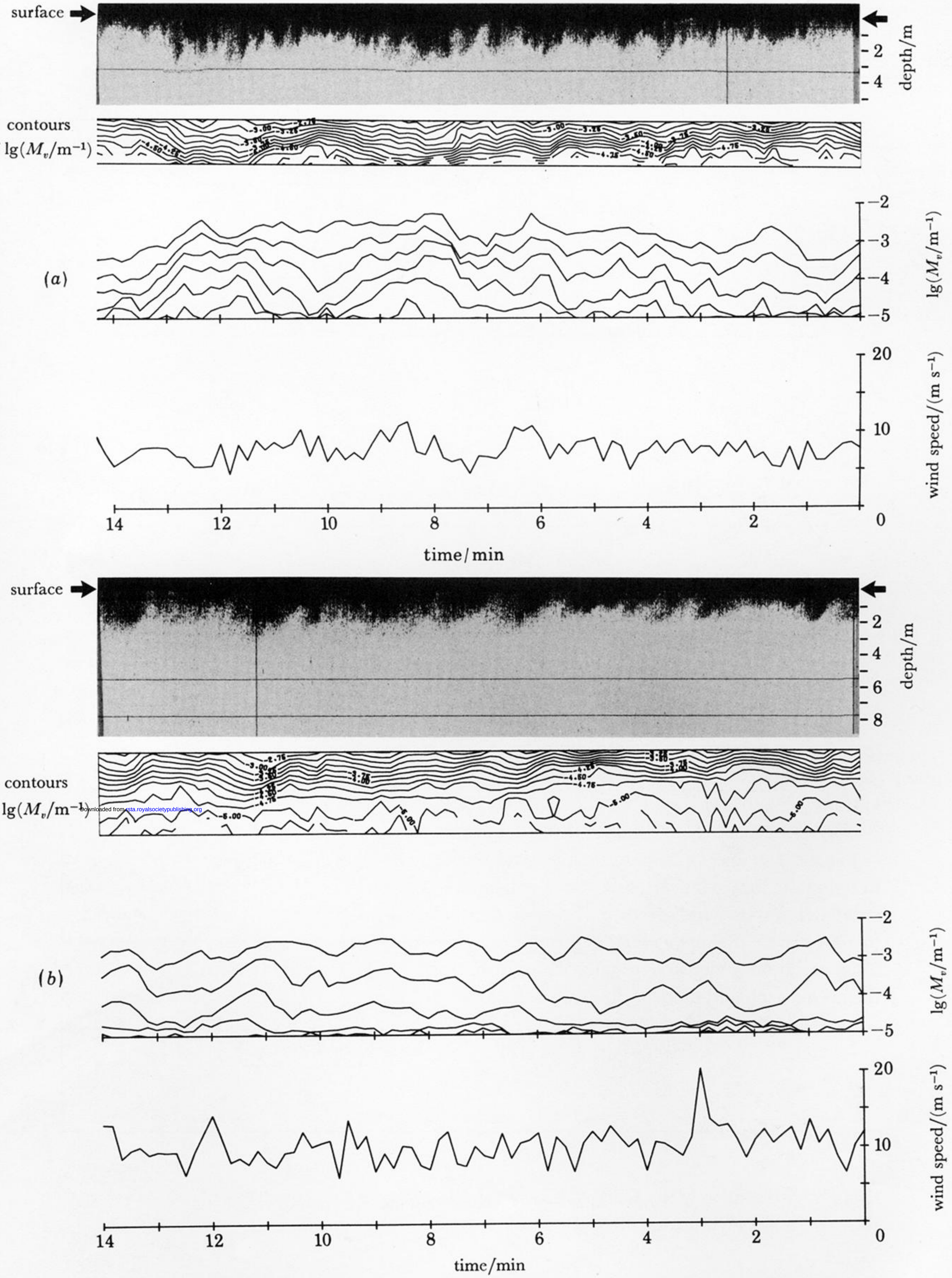

FIGURE 12. Sonagraph, M_v, and wind records from Oban in (*a*) southerly and (*b*) southeasterly winds: (*a*) $\Delta\theta = -2.4$ K (unstable conditions); (*b*) $\Delta\theta = 1.3$ K (stable conditions).

surface

depth/m

contours of $\lg(M_v/\mathrm{m}^{-1})$

(a)

$\lg(M_v/\mathrm{m}^{-1})$

wind speed/(m s^{-1})

time/min

surface

depth/m

contours of $\lg(M_v/\mathrm{m}^{-1})$

(b)

$\lg(M_v/\mathrm{m}^{-1})$

wind speed/(m s^{-1})

time/min

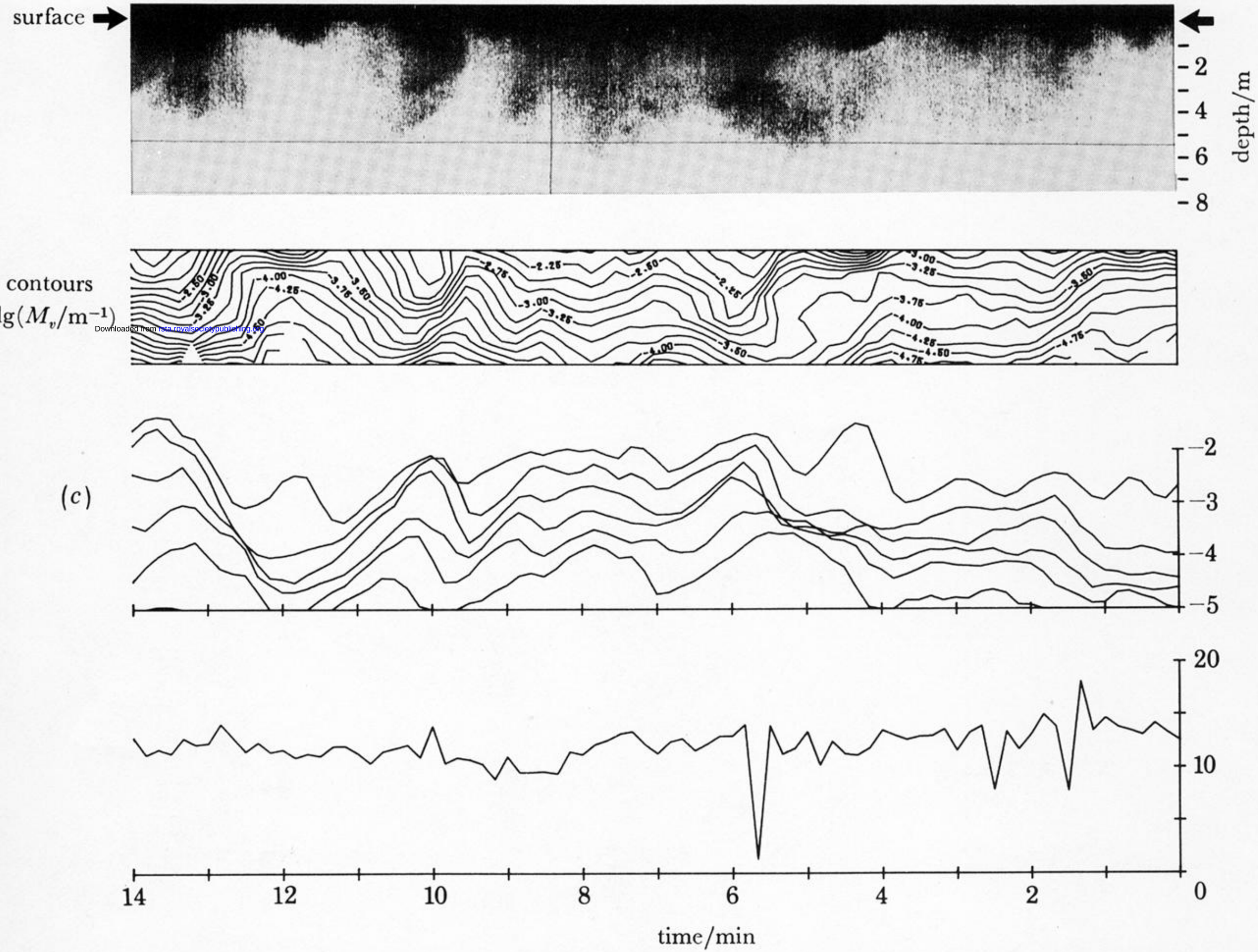

FIGURE 13. Sonagraph, M_v, and wind records from Oban in (*a*), (*c*) northeasterly and (*b*) northwesterly winds: (*a*) $\Delta\theta = -2.0$ K; (*b*) $\Delta\theta = -1.8$ K; (*c*) $\Delta\theta = -3.4$ K. The low value of wind speed at about 5.7 min is due to a fault in the anemometer.